LAMINAR BOUNDARY LAYER RESPONSE TO A STEP INPUT BY AN ARRAY OF PLASMA ACTUATORS

HOSSEIN KHANJARI

A THESIS SUBMITTED TO THE FACULTY OF GRADUATE STUDIES
IN PARTIAL FULFILLMENT OF THE REQUIREMENTS
FOR THE DEGREE OF
MASTER OF APPLIED SCIENCE

GRADUATE PROGRAM IN MECHANICAL ENGINEERING
YORK UNIVERSITY
TORONTO, ONTARIO

FEBRUARY 2021

Abstract

Bypass transition is a subcritical transition pathway that a boundary layer may follow from laminar to turbulent state. The latter is associated with higher drag. Prolonging the laminar boundary can therefore enhance efficiency in applications such as the flow over aircraft. Bypass transition is caused by the growth of streaks of low and high velocity in the laminar boundary. Spanwise arrays of plasma actuators have shown promise in experimental demonstrations of the active cancelation of these streaks in an open-loop and also closed-loop feedback control framework to delay transition in the past. However, when the plasma actuators were given a step input to model a fast response to a detected streak, a non-minimum phase response of the far-field velocity and shear stress was detected. Experiments were limited to only the streamwise velocity component and to regions considered in the far fields given physical sensor limitations.

In this thesis, a spanwise array of plasma actuators in a Blasius boundary layer are simulated numerically. The output of the plasma actuators is modeled as a momentum source to the flow. The spatial distribution and the magnitude of the momentum source were parametrically varied to explore the effects of the parameters on the generated disturbance velocity in the boundary layer. The velocity disturbance is decomposed into the discrete spanwise wavelengths related to the spacing of the actuators to compare the different parameterized cases. The variation in the composition of the disturbance energy is compared to an existing experimental database to determine the combination of parameters required to calibrate the body force model.

The primary focus of this thesis is to examine and explain the flow phenomenon related

to the occurrence of the non-minimum phase behavior when a step input is applied to the actuators. In this regard, the transient vortex evolution in the far-field downstream and also directly over the region where the plasma actuators input a body force is studied. In addition, the transient evolution of the spanwise and streamwise wall shear stress components considered. It is shown that streamwise vorticity generated precedes the formation of the velocity streaks. The onset of secondary vortex structures appears responsible for the observed non-minimum phase behavior.

Acknowledgements

I would like to express my deep gratitude and appreciation for Dr. Ronald Hanson for all of his invaluable guidance, support, and encouragement during this project.

I am also so grateful to my dear parents and my sister and also my friends who were worried about how I was doing far away from home during the completion of my master's degree, and to those who were close encouraging me to keep on working as hard as I could to finish this project.

Table of Contents

List of Tables

List of Figures

Chapter 1

Introduction

The rise of greenhouse gas (GHGs) emissions, such as CO_2, into the atmosphere, can lead to uncontrollable and fast happening consequences like increased sea levels and temperature [1]. According to the Paris Agreement, Canada plans to reduce the GHGs emission below 30% of 2005 by 2030, and in a more advanced plan, aims to achieve zero-net emissions by 2050 [2, 3]. The transportation sector, worldwide shipping, airline industries account for significant fuel consumption and, as a result, a considerable CO_2 emission [4]; for example, in Canada, 1% of the total emissions attributes to the aviation industry, which contributes to the 2.8% of the Canadian Gross Domestic Product (GDP) [5]. A huge part of the required energy and fuel consumption is to overcome the drag force [6]. Therefore, any drag reduction will bring substantial environmental and economic benefits.

Aerodynamic drag force is caused by pressure and shear stress. For commercial passenger flights, nearly half the total drag force is caused by the presence of the boundary layer on the surfaces of the aircraft [7]. The boundary layer is a thin layer of fluid that forms contiguous to the solid walls, and there is a velocity gradient inside it due to the viscous effects [8]. Boundary layer states have a direct impact on the amount of the generated drag force [7]. Therefore, boundary layer control by applying flow control strategists, including active control, passive control, and shape optimization, can help to reduce the skin friction drag by preventing the flow from transition and keep it in the desired state or impact it while

remaining in a particular state [6, 7, 9].

Bypass transition, which occurs by the breakdown of the amplified elongated streaks is a form of sub-critical transition to turbulence [10, 11]. A closed-loop control system is required for controlling the transient growth of streaks in Bypass transition because of their stochastic nature. Closed-loop systems require sensors, actuators, and controllers. For example, Hanson *et al.* [12] designed and employed a closed-loop control system using plasma actuators and wall shear stress sensors. The promising results of that experimental study are the basis of the current numerical research.

This thesis is motivated by the experimental work of Hanson *et al.* [12, 13, 14]. Hanson *et al.* [14] found that downstream of the plasma actuators, a non-minimum phase response of the streamwise flow velocity occurred near the wall when the output of the actuator was first activated and then deactivated. Such a response is known to limit the overall efficiency of the control system. The previous experimental study of the flow behavior is, however, limited to only the streamwise velocity component of the flow. The main objective of this thesis is to determine the cause of this behavior using the full flow domain information available in the simulation. Toward this objective, first a numerical simulation is designed and the simulated body force is tuned to closely match the observed experimental results prior to simulating the step response of the boundary layer for forcing.

The structure of this thesis is as follows. In the next chapter the background topics of particular importance to this research topic are reviewed, such as Bypass transition, flow control, plasma actuators and body force modeling. Chapter 3 includes the experimental setup details that were used by Hanson [14]. Subsequently, the numerical model details. The body force model is explained in detail. Finally, numerical model verification is provided. The steady actuation results for experiments are discussed in chapter 4. A parametric study on the body forces is also conducted, and the simulated model is matched with a particular experimental model. Chapter 5 discusses the dynamic flow response for both models. The transient evolution of the disturbances and vortices are depicted spatially. In chapter 6, the concluding remarks and recommendations of this study are presented.

Chapter 2

Background

2.1 Boundary Layer History & Transition

In the early 20th century, Ludwig Prandtl proposed the concept of the boundary layer [8]. Since then, the boundary layer has remained an active research topic given its importance to a wide-range of engineering applications. Of particular relation to the focus of this thesis is the sub-critical transition of a boundary layer from laminar to turbulent.

The process of boundary layer transition from laminar to turbulent is reviewed by Saric [15]. The location where the laminar boundary layer transitions to turbulence depends on the penetration of disturbances in a process known as Receptivity. The essential characteristic of these disturbances is their amplitude, which defines the path for transition [15]. The flow will become unstable and cause transition if disturbances reach sufficient amplitude. Although the transition can happen at different Reynolds numbers for a boundary layer over a flat plate depending on the route of the transition, the reported critical Reynolds number (Re), above which the flow will become unstable and transition happens, is about 10^6 [8].

2.1.1 Governing Equations

A brief review of the governing equations related to the flow phenomena considered in this thesis is given. Further details can be found in chapters 1 and 3 of Ref [16]. An incompressible

flow of a Newtonian fluid with constant viscosity is considered in this thesis. The equations of motion are given by the Navier-Stokes and continuity equation. For an incompressible shear flow, the continuity and NS equations can be written as:

$$(\frac{\partial}{\partial t} + \mathbf{u} \cdot \nabla)\mathbf{u} = -\frac{1}{\rho}\nabla p + \frac{\mu}{\rho}\nabla^2 \mathbf{u} \tag{2.1}$$

$$\nabla \cdot \mathbf{u} = 0 \tag{2.2}$$

In equation (2.1 & 2.2), $\mathbf{u}$ is the velocity, t is time, p is the pressure. By applying an infinitesimal disturbance to a parallel flow, in which the streamwise velocity only depends on wall-normal direction, following equations can fully define the fluid flow. In these equations $(x, U), (y, V), (z, W)$ are streamwise, wall-normal and spanwise spatial coordinates and corresponding velocity components respectively, where the spanwise and wall-normall velocity components for a parallel shear flow are zero. The coordinate system is the same as the coordinate system in Figure 2.1. In these equations the ν is the wall-normal disturbance velocity component; and (∇) is the divergence operator.

$$[(\frac{\partial}{\partial t}\nabla^2) - U''\frac{\partial}{\partial x} - \frac{1}{Re}\nabla^4]\nu = 0 \tag{2.3}$$

$$[\frac{\partial}{\partial t} + U\frac{\partial}{\partial x} - \frac{1}{Re}\nabla^2]\eta = -U'\frac{\partial \nu}{\partial z} \tag{2.4}$$

prime $(')$ denotes for the $y-$derivative, moreover, (η) is the normal vorticity and is defined as:

$$\eta = \frac{\partial u}{\partial z} - \frac{\partial w}{\partial x} \tag{2.5}$$

Introducing a wavelike disturbance to the equations 2.3 and 2.4 will result equations (2.8) and (2.9). The wavelike disturbances can be defined as:

$$\nu(x, y, z, t) = \tilde{\nu}(y)e^{i(\alpha x + \beta z - \omega t)} \tag{2.6}$$

$$\eta(x, y, z, t) = \tilde{\eta_y}(y)e^{i(\alpha x + \beta z - \omega t)} \tag{2.7}$$

where (α) and (β) are streamwise and spanwise wave numbers respectively and (ω) is the frequency. In addition, (D) is the differentiation operator with respect to y and $k^2 = \alpha^2 + \beta^2$.

$$[(-i\omega + i\alpha U)(D^2 - k^2) - i\alpha U'' - \frac{1}{Re}(D^2 - k^2)]\tilde{\nu} = 0 \qquad (2.8)$$

$$[(-i\omega + i\alpha U) - \frac{1}{Re}(D^2 - k^2)]\tilde{\eta} = -i\beta U' \tilde{\nu} \qquad (2.9)$$

2.2 Bypass Transition

If the boundary layer is exposed to low levels of free-stream disturbance, the exponential growth of two-dimensional Tollimen-Schlichting (TS) waves leads to the classical transition pathway. The growth of the TS waves can be described by equation 2.6, which is known as the Orr-Sommerfeld equation [16, 17]. At higher levels of external disturbance, the classical transition pathway is bypassed [17]. In Bypass Transition the streamwise elongated streaky structures, that are spanwise alternating low and high speed velocity regions are characteristic of the pre-transitional region (as shown in Figure 2.1). These streaky structures were termed Klebanoff modes by Kendall [18], who named them after the work by Klebanoff [19] who first noted the existence of these so-called Breathing-modes that had thickening and thinning effect on the boundary layer.

Bypass transition has three main steps [20]. The first step, as mentioned earlier, is the receptivity of free-stream disturbances to the boundary layer and the formation of the streaks. According to equation 2.7, wall-normal disturbance velocity ($\tilde{\nu}$) acts a forcing term on the wall-normal vorticity (η), which causes the low momentum flow near the wall to be replaced by the high momentum flow in higher regions of boundary layer and leads to a spanwise variation in streamwise disturbance velocity [10], a mechanism which is known as Lift-up [21]. The range of the disturbances' frequencies that can enter the boundary layer is limited to only low frequencies because of the Shear-Sheltering effect as discussed by Hunt *et al.* [22].

In the second step, streaks will experience an algebraic increase in their energy for a short time, Algebraic Growth. If they do not reach sufficient amplitude to trigger the secondary
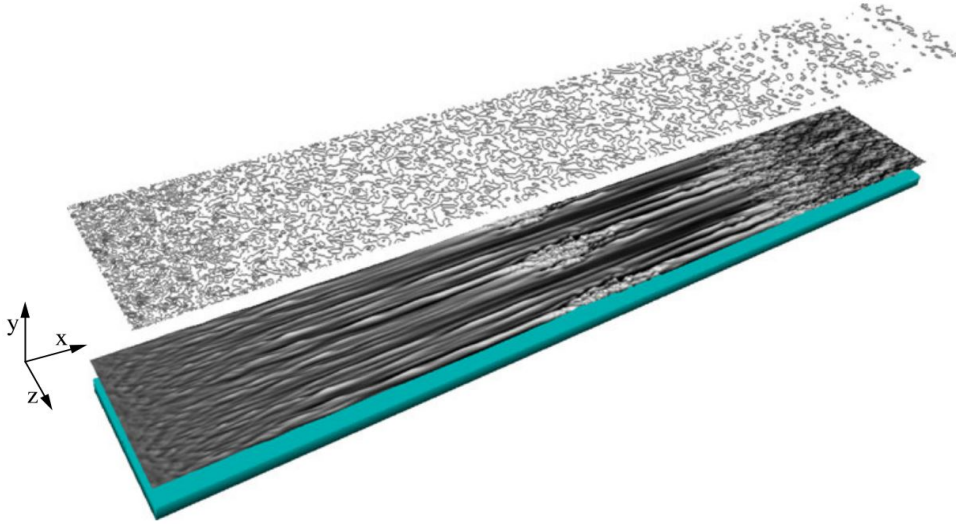
Figure 2.1: Boundary layer transition due to the breakdown of the streamwise elongated streaky structure. Contour plots representing the streamwise velocity perturbations in the range of $-0.15 < u' < 0.15$ inside the boundary layer and also in the free stream. Reprinted from Zaki [20].

instabilities [15], their linear growth is then followed by an exponential decay because of the viscous damping effects. The linear growth and exponential decay together are known as Transient Growth [23, 24]. Despite the fact that there is no model that can predict the transition accurately, studying the energy growth of disturbances can shed more light on Bypass transition. In this regard, Andersson *et al.* [24] studied the maximum disturbance energy growth inside the boundary layer by employing optimal theory. It is found that, the optimal disturbance, meaning the one that experiences the greatest rate of growth, occurs for $\beta = 0.45$, which is the spanwise wavenumber, and $\eta = 2.2$ which is defined as y/δ, where $\delta = (x\nu/U_\infty)^{1/2}$, is the Blasius similarity variable in which ν is the dynamic viscosity. Moreover, it is reported that the optimal disturbance appears as high and low speed velocity regions along the span (Figure 2.2b), is the flow response to the pair of counter rotating vortices which is shown in Figure 2.2a. The data shown in Figure 2.2 is at downstream location of x_f, is the final downstream location where the energy growth is integrated over.

In the third and final step of bypass transition, the amplified streaks will trigger traveling waves that cause the streaks to become unstable, causing the eventual breakdown to turbulence
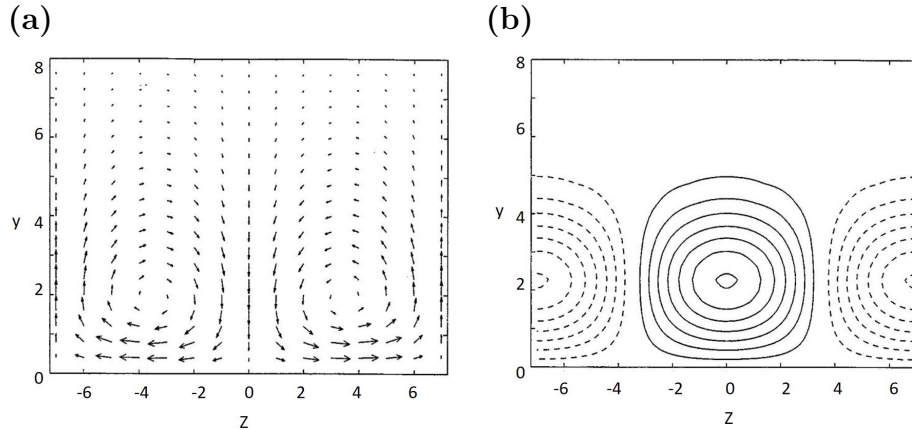
Figure 2.2: (a) Counter rotating vortices and the generated velocity vectors in $y - z$ plane, where y and z are the wall-normal and spanwise directions respectively, (b) corresponding optimal disturbance at downstream location $x_f = 1$, solid line represents the region of high speed flow and dashed lines represent the region of low speed flow. Reprinted from Andersson *et al.* [24].

[25]. In the direct numerical simulation by Vaughan *et al.* [26], two types of secondary instabilities are classified as inner and outer modes. These modes are dependent on the amplitude and frequency of the streaks, and it is pointed that the inner modes, which are also called varicose modes, occur around the local overlap between high and low-speed streaks while the outer modes occur around the low speed streaks Vaughan *et al.* [26]. The critical streaks amplitudes for the inner and outer modes were studied by Andersson *et al.* [11] and were found to be 26% and 37%, respectively.

2.3 Flow Control

Flow control is a term often used to denote the manipulation of a flow field to achieve a desired change for a particular application. For example, flow control can be applied to decrease skin friction drag, delay transition, delay separation, enhance lift, reduce noise, and sometimes a combination of them. Delaying transition will provide advantages that can help achieve different goals simultaneously. For instance, delaying boundary layer transition leads to less noise than a comparable turbulent boundary layer and lower drag, which also causes

less skin friction drag, that latter will reduce emissions and fuel consumption [9].

Various flow control methodologies exist. One methodology is termed opposition control by Choi *et al.* [27]. In opposition control a counter disturbance of roughly opposite sign and similar amplitude is input to reduce or cancel targeted events deemed critical to what the controller wishes to reduce or otherwise effect. Opposition control has been initially applied to the control of near wall events in a turbulent boundary layer (see for example Choi *et al.* [27]).

Active control methods, such as opposition control, require the use of actuators to create the desired counter disturbance. There are different classes of active actuators [28]. One of the most common classes is called Fluidic, which comprises Synthetic jets [29] and Blow & Suction actuators [30]. The fluidic actuators can use the working fluid or also can be a source/sink of mass for the flow. The other class includes the actuators with a moving body that acts inside or at the boundary of the domain. Vibrating ribbons [31], vibrating flaps, and vertical wall motions [32] are some examples of this type. Another class of the actuators is the Plasma actuators that are discussed thoroughly in Section 2.4. In practice, adjusting the parameters of the actuators and the control region not only is not very feasible but also is not the best way to enhance the efficiency because of the energy consumption may increase, that takes the control system away from the optimal point [33]. Moreover there are some drawbacks related different type of actuators that need to considered prior to applying them in the desired condition. For example, Lundell *et al.* [34] have mentioned that synthetic jet actuators yet need to be improved to become durable, flexible, small, and cheap for active flow control applications.

Flow control systems can be categorized as open-loop or closed-loop systems [35]. Open-loop control systems are designed for a specific range of condition, while closed-loop systems can be adjusted for different conditions [35]. In closed-loop controllers, the effectiveness of the control system depends on the capability of the actuators to alter the flow [12]. It also depends on the available data from the flow field to make control decisions. In experiments, available data is limited to what can be measured in real time and more practically, to what

information of the flow that can be obtained at the wall. Numerical simulations do not have this restriction and have therefore had significant contributions to the development of the flow control strategies by providing full flow domain data that helps overcome the issues regarding the experimental works for closed-loop controllers.

For a closed-loop system it is shown that a linear controller would be sufficient for the control of the linear mechanisms lead to the transient growth of streaks in Bypass transition [12]. The choice of applying linear controller considerably reduces the complexities related to the design and implementation of the control system [14]. As reviewed by Kim [4], the streaks in a buffer layer of a turbulent boundary layer (TBL) are formed in the same manner as the streaks in Bypass transition. The generation and regeneration of the vortices in TBLs occur via linear mechanisms [4]. Therefore, linear controller can also be applied for the control of turbulent boundary layers. For example, Sharma *et al.* [36] developed a linear controller system and could successfully relaminarise a nonlinear boundary layer, by controlling the streaks. Despite the similarities between the streaks in laminar and turbulent boundary layers, the streaks of the TBLs are smaller compared to the streaks in Bypass transition, which highlights the challenges regarding the experimental studies on TBL flow control. Moreover, the streaks have higher frequency in TBLs, suggesting the need to fast reacting control systems [37]. The importance of studying Bypass transition beside providing significant advantageous for delaying transition is the potential applications in the control of TBLs.

2.4 Plasma Actuators

Plasma actuators have gained significant attention for flow control over the last two decades. These types of actuators offer advantages of low mass, no mechanical parts, and are easily integrated with an experimental model (for example by adhering to the surface using tape-based parts in construction) [28]. Corona discharge and Dielectric Barrier Discharge (DBD) actuators [38], are the two most common types of plasma actuators for flow control. Discussion is limited to DBD actuators since they were used in the experiments of Hanson *et al.* [14]

and will be modeled in the numerical simulations of this thesis. In the following sub-sections an overview of the physical mechanism of the operation of DBD actuators, their properties, applications to flow control and numerical models to simulate their output is provided.

2.4.1 Structure of a DBD Plasma Actuator

DBDs have no moving parts. Compared to conventional mechanical-based actuators, DBD actuators are, thin, and flexible and can be used on many aerodynamic surfaces, either flat or curved [28]. They have fast time response, which is important to enhance the bandwidth of a control system [39]. In the most simple configuration, DBD actuators are made up of two electrodes that are flush-mounted on both sides of a thin layer of dielectric, as shown in Figure 2.3. The width of the electrodes, the thickness of the dielectric, and the distance between the electrodes effect the actuator performance and have been the focus of several past studies to optimize output or efficiency [40, 41].
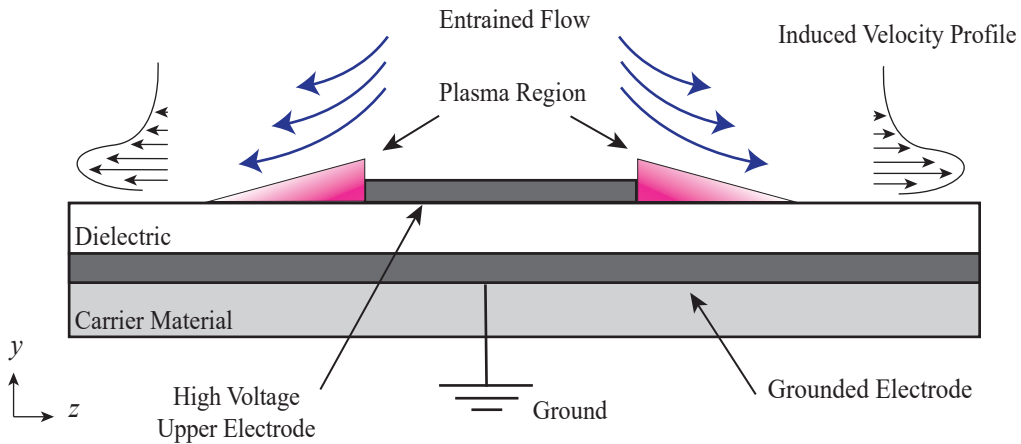
Figure 2.3: Schematic of a common symmetric DBD with its different components. The plasma is depicted over the surface on either side of the high voltage electrode. The entrained flow and induced wall jet are shown.

2.4.2   Physics of Operation

The basic concept of the operation of the DBD actuators is described as follows. Applying high voltage to the electrodes leads to the formation of an electric field between the electrodes that ionizes the air particles in that region. If the electric field reaches sufficient amplitude, it causes a gas discharge and forms a plasma [42], mostly in the range of glow-discharge for DBDs [43], which is visible with blue-violet color over the surface of the dielectric [14]. DBD plasma actuators operate with high AC voltages generally in the range of 1 to 50 kV, while the typical frequencies of the applied voltage considered in the literature tend to be between 0.5 to 25 kHz with sinus, square and triangular wave types [43]. In case of using DC voltage to prevent the self-limiting nature of the plasma formation it is needed to increase the voltage however using AC voltage solves this problem [44].

Inside the plasma (Ionic-Wind), traveling ions in a half-cycle of the AC voltage from the electrodes to the dielectric and their reversion to the electrodes in the other half-cycle, creates electrohydrodynamic (EHD) body force that is because of the transferring momentum to the surrounding neutral air particles [44, 45]. The momentum transfer, is the salient mechanism of the DBDs, and chiefly increases the kinetic energy of the air particles and with less effect on the temperature of the air particles [46]. Once the plasma is established, it creates a spanwise jet flow that creates a velocity profile that depends on different parameters, including electrical and mechanical properties and atmospheric conditions (see, for example [47, 48, 40]). Since the DBDs are not a source of mass [49], the jet flow leads to a wall-ward motion for the flow above the actuator by generating a pressure gradient [41]. The spanwise jet (as schematically shown in see Figure 2.3) leads to the formation of a vortex above the jet profile [49].

While a wide range of studies have considered the steady operation of the plasma actuator, a limited number consider the temporal development of the flow as the actuator is enabled. One key observation is the starting vortex before profile of the jet reach stationary condition. Moreau *et al.* [38] observed the starting vortex by using Schlieren visualizations, a technique based on the gas density gradients. In a later study by Balcon *et al.* [50] the starting vortex

was observed by using particle image velocimetry (PIV) measurement. In that study, a time of 400 ms reported for the jet velocity to reach a steady condition while it grows before that time. The study by Whalley *et al.* [51] provided a clearer picture of the starting vortex formation by using PIV and smoke flow visualization. It is shown that momentum transfer creates a coherent and self-similar starting vortex beside the actuator. As time increases, the vortex becomes bigger and moves away from the wall and edge of the actuator. Due to the
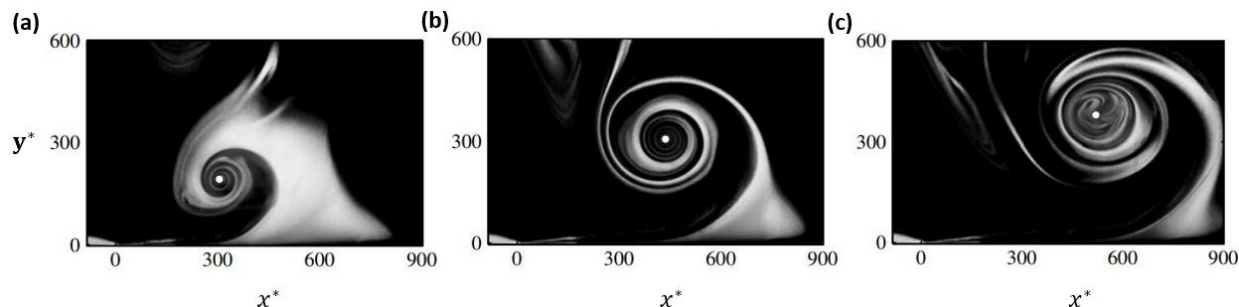
Figure 2.4: Smoke flow visualization of the vortex formation beside a DBD in quiescent air for different times, (a) $t^* = 1620$, (b) $t^* = 2700$, (c) $t^* = 3780$. The plasma initiates from $(x^*, y^*) = 0$ and has x^* extent of 60 to 90. Figure reprinted from Whalley *et al.* [52].

no-slip condition, a secondary vortex will form beside the main vortex. The primary and secondary vortices as a result of viscous dissipation become weaker as they grow. A schematic of this process is shown in Figure 2.5, which is studied by Whalley *et al.* [52] by using smoke visualization. In this figure, $t^* = tU_0^2/\nu$, $y_c^* = y_c U_0/\nu$ and $x_c^* = x_c U_0/\nu$, where ν is the kinematic viscosity, x_c, y_c are the vortex core location with respect to the origin and U_0 is the maximum induced velocity by the actuator. In a more recent study by Zhang *et al.* [53] the temporal development of the flow beside a plasma actuator is found to follow four steps. In the first step a very thin wall jet, sufficient to entrain the flow, is formed. Subsequently, an arched jet will be created beside the edge of the electrode. Then, the starting vortex gradually appears while the arched jet gradually disappears. Ultimately the starting vortex disappears and a stationary wall jet with constant deflection angle forms beside the edge of the upper electrode. The pictured transient induced flow can be found in Zhang *et al.* [53].

Plasma actuators may be arranged such that they generate streamwise vortices that
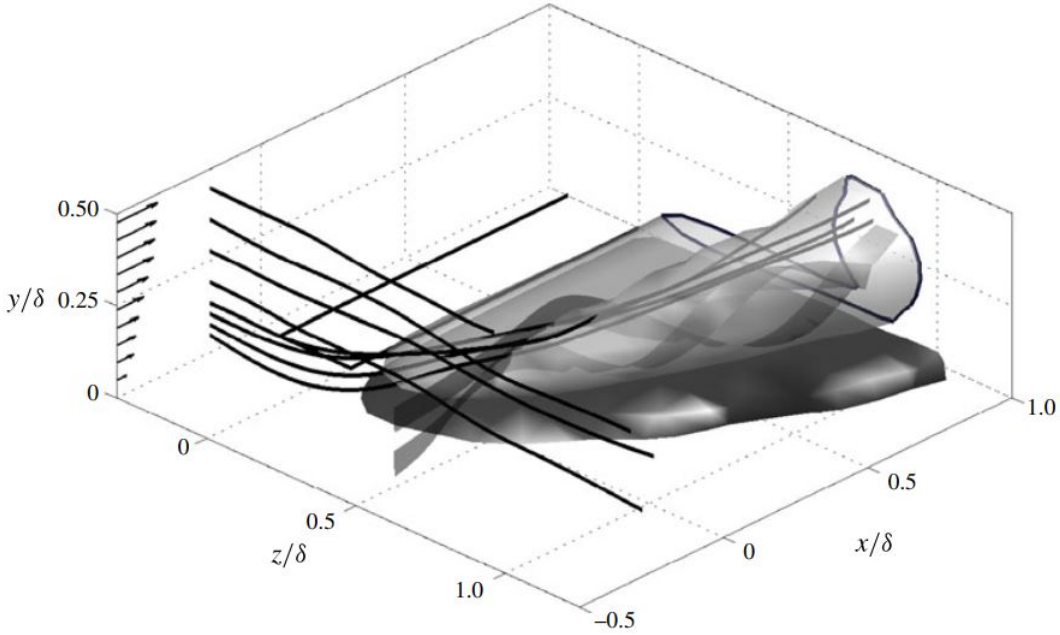
Figure 2.5: Vortex lines with velocity stream-ribbons near the tip of DBD vortex generator. Streamwise vorticity isosurfaces: $\Omega_x \delta / U_\infty = 3.5$ (dark grey); $\Omega_x \delta / U_\infty = -3.5$. Vortex lines are issued from streamwise location of $x/\delta = -0.2$, wall-normal locations of $y/\delta = [0.057, 0.086, 0.114, 0.143, 0.200, 0.286, 0.371, 0.457]$, and spanwise location of $z/\delta = -0.3$. Figure reprinted from Jukes *et al.* [54]

enable generating pairs of impinging wall-jets, causing a spanwise-periodic array of streamwise vortices in a boundary layer [55]. In the streamwise oriented plasma actuators the strength of the vortex increases as it travels along the edge of the actuator. This implies that the DBD adds circulation to the streamwise oriented vortex as it is convected over the length of the streamwise oriented electrode of the plasma actuator. Two key parameters that have notable effects on the streamwise vortex structure are maximum spanwise wall jet velocity W_p and spanwise wall jet's thickness δ_p [49]. Jukes *et al.* [54] studied the streamwise vortex formation for a single plasma actuator placed in a laminar boundary layer, which provides a comprehensive picture of steady vortex formation under constant actuation. A jet, which is very thin compared to the boundary layer height, forms beside the edge of the actuators ($z/\delta = 0$) and results in a vortex beside the actuator. However, it is found that in a streamwise oriented plasma actuator, there are two more sources of vorticity. Once the jet is formed,

it causes a blockage and leads an upward motion for the upcoming boundary layer, shown by the streamwise velocity ribbons. This lifting effect causes the spanwise vorticity of the boundary layer, shown with black lines in Figure 2.5, to move to the regions with higher streamwise velocity. Therefore, they will be reoriented to the streamwise direction. Moreover, after the body force region, $z/\delta > 0.38$, the spanwise jet flow decays gradually and is twisted into the streamwise direction by the upcoming boundary layer. Jukes *et al.* [49] pointed out that these two flow reorientations act as additional vortex sources that do not exist for the DBDs in quiescent air.

2.4.3 Efficiency of DBD Plasma Actuators

Efficiency of plasma actuators is defined as the ratio of the produced mechanical power and power consumed by the actuator [41]. There are a number of factors that effect the electrical efficiency. For example, the material used for the electrodes has not significant effect on the final efficiency [41], however, its geometrical features can improve the output of the plasma actuators. Enole *et al.* [56] showed that decreasing the thickness of the exposed electrode increases the thrust by the plasma actuators. In addition, changing the shape of the edge of the exposed electrode led to increase in the resulted EHD force [57], but it is also pointed that serrated edge can create periodic vorticity near the edge of the actuators [58].

The dielectric layer, usually reaches a few millimeters thick, and is usually made up of either Kapton, glass, or Teflon or Teflon and several other options also are common [39]. Thomas *et al.* [56] compared different dielectric materials with different thickness. They found that increasing the thickness permits applying higher voltages, while for the same thickness, lower dielectric constant leads to higher efficiency. Although the dielectric effects the efficiency and therefore output of the plasma actuator (for example the relative permittivity is related to heating losses) some dielectric materials tend to degrade during operation. The physical degradation and the relationship to power consumption and capacitance of the plasma actuator was studied by Hanson *et al.* [59]. They demonstrated that the operation of the plasma actuator led to a thinning of the polymer-based dielectric (Kapton). As a result,

the capacitance of the actuator increased since the plasma region, which causes a virtual electrode is nearer the grounded electrode after degradation of the dielectric surface. In turn the power consumption of the actuator was found to increase, which is thought to cause a change in force output.

The waveform supplied to the plasma actuator have shown significant effect on the thrust and also power consumption, since this parameter can change the discharge regime that has direct relation on the resulted EHD force [41]. For a constant power consumption a sinusoidal waveform is recommended, for further details see the review [41, 44]. Benard *et al.* [60], studied the frequency of the applied voltage. For a constant amplitude increasing the frequency leads to the higher consumed power by the actuator, however, they have highlighted the importance of the frequency for flow control. Increase in the amplitude of the applied voltage causes the higher thrust for the actuators [61] which also will lead to higher power consumption. However, as pointed by Sato *et al.* [62], the high voltage power supplies are expensive and heavy, which limits their usage. Hence, for the desired application both the geometrical and electrical properties need to be selected properly, and adjusted to have the highest efficiency [41, 63].

2.4.4   Applications of DBD Plasma Actuators in Flow Control

Transferring quasi-steady momentum to the flow enables the DBDs to manipulate the flow and has made them promising means for active flow control [64]. They have shown remarkable effects in real flight applications [65]. Transition control, delaying or hastening, and skin friction drag reduction in turbulent boundary layers are of the two most important areas that DBDs have been applied.

Plasma actuators have been used to suppress TS waves occurring in a laminar boundary layer. For example, Grundmann *et al.* [66] demonstrated the delay the transition over a flat plate by using a closed-loop control scheme and using DBDs as the actuator. TS waves were created by an oscillating surface upstream of the control region. The resulted TS waves were damped by the actuators. It was shown that the amplitude of the TS wave oscillations were

reduced by 20-30 %. As a result, the transition region, in the case of steady forcing, occurred further downstream. In this research the electrodes of the plasma actuator were elongated in the spanwise direction of the boundary layer flow such that the forcing was applied in the direction parallel to the flow (streamwise direction). However, Barckmann *et al.* [67] later used a spanwise array of plasma actuators to generated streamwise oriented streaks to stabilize the TS wave; the idea was demonstrated earlier by Fransson *et al.* [68] to be an effective control method, albeit using mechanical vortex generators.

Entraining the flow above the actuator and replacing the high momentum flow with the near-wall low momentum flow, which is very vulnerable for the separation, has made the DBDs suitable for separation control [69]. For instance, Post *et al.* [70] used plasma actuators at the leading edge of an airfoil to reattach the flow that led to significant drag reduction. Jukes *et al.* [49] studied the application of the plasma actuators for separation control over a ramp. Counter-rotating and co-rotating streamwise vortices were produced using two different spanwise arrays of actuators. It was demonstrated that the counter-rotating arrays were more effective for separation control. A minimum ratio of 7% for induced velocity by plasma actuators over the free stream velocity was reported as the threshold for a possible separation control.

In the related works of Hanson *et al.* [12, 13], DBDs were used for the first time to control streamwise oriented streaks occurring in the Blasius boundary layer. In this example of opposition control, the streaks where initially introduced into the laminar boundary layer by an array of roughness elements, leading to spanwise deviation from the Blasius boundary layer profile, as shown in Figure 2.6(a). Applying DBDs further downstream could attenuate the created streaks not just significantly but, more importantly, linearly, which is a notable simplification compared to the closed-loop system. On the left side of Figure 2.6, the η is the Blasius similarity variable, U' is the streamwise disturbance velocity, Δz is the spacing between the middle of the actuators. On the right side of this figure, the power spectrum of different modes of the disturbance with respect to the spanwise wave-numbers (β) is shown. It is evident that the first mode with the highest energy content has lost its energy extensively
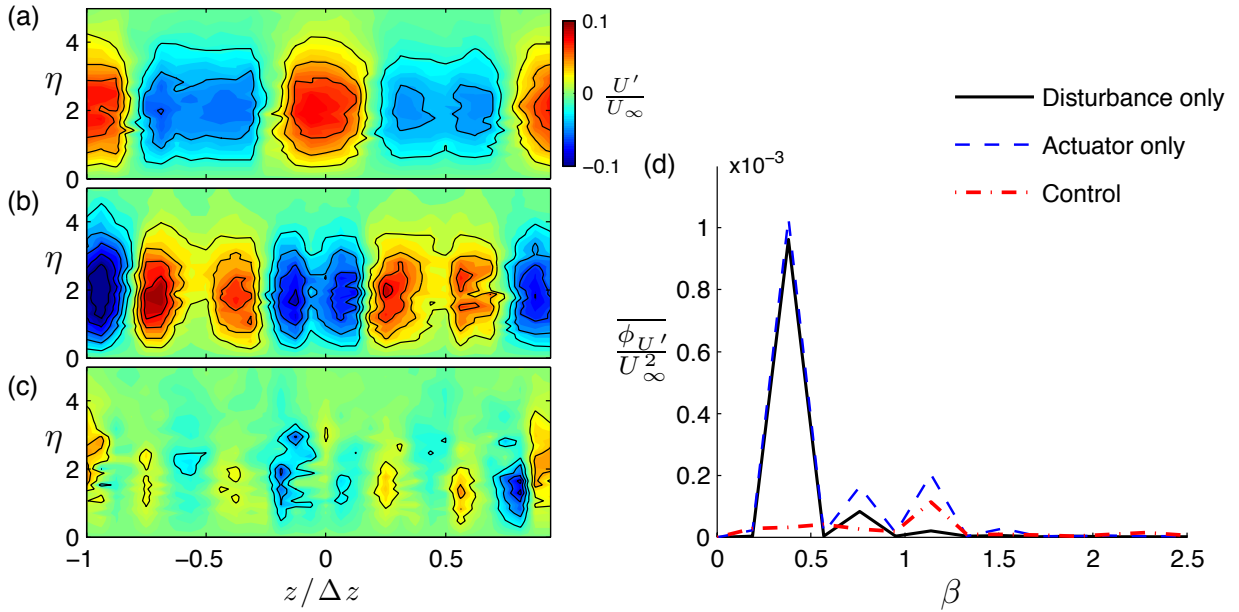
Figure 2.6: Contour plots of U'/U_∞ determined at x = 450 mm for (a) the roughness disturbance only, (b) only disturbance created by the plasma actuators with 8 mm width, and (c) control. (d) The average spanwise wavenumber spectrum for each corresponding case. Reprinted from Hanson [14].

and about 97 %. In the next step of this study, a closed-loop control system was applied. The effectiveness of the control system, which was defined based on the ability of the control system for attenuating the first mode of the energy that can be applied similarly for the total energy of the disturbance, was examined. The energy of the first mode was reduced by 94% and a total reduction in energy of 74% to 86% was reported. This total reduction depended mostly on residual energy that occurred at shorter spanwise lengths and it was assumed negligible since the corresponding spanwise mode was predicted to decay.

Due to the stochastic nature of the Bypass transition [71], a closed-loop control system will bring higher efficiency for controlling the streaks, since it enables to more accurately target the streaks [72]. Bade *et al.* [71], used plasma actuators to control the transient growth of the streaks in a laminar boundary layer. They used a closed-loop system, by providing the boundary layer response to the generated vortices, using wall shear stress sensors. Although the system could effectively attenuate the generated streaks by the roughness element, some

of the challenges in closed-loop system were addressed. For the feed-forward sensors it is necessary to leave a distance between actuators and the sensors, that detect the streamwise shear stress component, due to the lag between the vortcies passing a streamwise located and the corresponding streaks, that was also shown by Naguib *et al.* [10]. In addition, it is highlighted that the convective time of the naturally occurring disturbances and the ones generated by actuators can significantly affect the feedforward control bandwidth. Moreover, they have concluded that moving the feedback senors closer to the actuators can enhance the bandwidth of the system. As previously pointed, the key advantage of the active flow control is the ability of actuators to be turned on when needed. In this regard, Hanson applied an impulse for 0.1 second duration to the DBDs. The flow response was interesting since it showed a non-minimum phase behavior, that was also observed in the study by Jacobson *et al.* [37], in which they were using different type of actuators. This flow response and the reason for this type of flow behavior are more elaborated in Chapter 5.

2.4.5 Numerical Simulation of DBDs

The effect of plasma actuators in numerical simulations are often modeled as a body force. For example, Font *et al.* [73] simulated the plasma actuators numerically. Although the simulated body force had no spatial distribution, results were in a good agreement with the experiment. Futrzynski [74] studied the effect of plasma actuators numerically with applying a momentum source term with exponential distribution in space. There are few models proposed to simulate the plasma actuators more accurately. These models are commonly comparable depending on their complexity and accuracy for simulating the physics of plasma and momentum transfer, and ultimately after calculating the body force, it will be put in the NS equations [75, 76]. One of the models reported by Suzen *et al.* [77] solves two additional equations besides the NS equations one for the electrical field because of the applied voltage and one more for the charge density because of the ionized air particles to calculate the body force. Another more accurate model is known as the plasma-fluid model. This model assumes the plasma as a separate dynamic and then combine it with the base fluid dynamic

by considering the different time-scales, for further details, see Jayaraman *et al.* [78].

Despite the good accuracy of the models mentioned above, their complexity requires powerful computers and are computationally expensive. However, a phenomenological model proposed by Shyy *et al.* [79], which is founded on the electric field distribution, has slightly solved this issue. The electric field variation leads to the distributed body force, which is maximum in the vicinity of electrodes and near the inner edge of them. It decreases as it
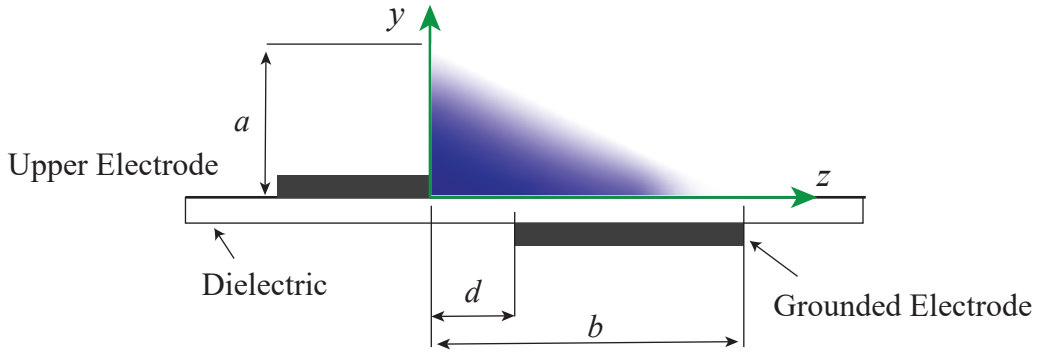
Figure 2.7: Schematic of EHD body force distribution caused by a DBD in Shyy model [79].

moves away from there, as shown in Figure 2.7. The distributed electric field can be written mathematically as follows:

$$|E| = E_0 - K_1 z - K_2 y \tag{2.10}$$

in which E_0 is the maximum electric field that happens between the inner edge of electrodes and is defined as:

$$E_0 = \frac{V}{d} \tag{2.11}$$

where V is the applied voltage and d as it is illustrated in Figure 2.7 is the distance between the electrodes in z direction. K_1 and K_2 are two constants that can be calculated according to electric field breakdown in the plasma fluid boundary and can be calculated by:

$$K_1 = \frac{E_0 - E_a}{b}, \quad K_2 = \frac{E_0 - E_a}{a} \tag{2.12}$$

where E_a is the air dielectric strength. The electric fields in z and y direction are given by:

$$E_z = \frac{EK_2}{\sqrt{K_1{}^2 + K_2{}^2}}, \quad E_y = \frac{EK_1}{\sqrt{K_1{}^2 + K_2{}^2}} \tag{2.13}$$

Given the z and y components of the electric field and the collision efficiency (α), density of charge density (ρ_{nc}) and the electronic charge (e_c) the EHD body force can be calculated by:

$$f_{eff,z} = \alpha E_z \rho_{nc} e_c, \quad f_{eff,y} = \alpha E_y \rho_{nc} e_c \tag{2.14}$$

The high frequency of the applied voltage implies that the body force may be assumed constant as previously discussed, hence the time averaged velocity for the length of the duty cycle (T) and total length of the time period when the plasma is formed is given by:

$$f_{avg,z} = f_{eff,z} \Delta t_p / T, \quad f_{avg,y} = f_{eff,y} \Delta t_p / T \tag{2.15}$$

Consequently:

$$f_{EHD} = (f_{avg,z}, f_{avg,y})^T. \tag{2.16}$$

The calculated body force can be applied in the NS equations as a source of momentum. In this model, as it is evident in Figure 2.7, the spatial distribution of a body force can be defined using the geometric variables a (height), and b (width), as well as the force magnitude. As was shown by Enole *et al.* [80], the plasma extent (or width as used in Figure 2.7) has direct relation with the applied voltage. Furthermore, when the generated body force is nearer to the wall the losses (due to drag caused by shear stress) will become more significant [73]. Moreover, as discussed earlier a higher voltage will lead to more thrust, meaning more EHD force. Since there does not exist a formulation that predicts the spatial distribution and magnitude of the body force for this model, a parametric study is required to tune the coefficients of the modeled force.

Chapter 3

Numerical Model & Experimental Details

The present numerical-based research is motivated by, as previously explained, the previous experimental results of Hanson *et al.* [12, 13, 14]. The full flow domain data obtained from the simulation is used to improve the understanding of the non-minimum phase response of the boundary layer to step forcing. In this section, the experimental configuration and methodology of the steady forcing by Hanson *et al.* [14] is summarized followed by the description of the intentionally matched simulation and studies performed for validation purposes, including the mesh and time step studies.

3.1   Experimental Setup

The experimental setup that was built and ran with Hanson, is briefly reviewed here to first provide a better picture of the actuators placement and the experiment's methodology, secondly, enable the comparison with numerical model. A laminar boundary layer was established on a cast aluminum test plate, 2.1 m long, 1.2 m width, and 12.7 mm thick that was inserted in the closed-loop wind tunnel at the University of Toronto, with 1.2 m × 0.8 m cross-section area and 5 m long test section. The air at room condition with the free-stream

velocity of 5 m/s, and the turbulence intensity less than 0.05 % was entering to the domain. The flow velocity was measured using an array of two hot-wire anemometers. The position of
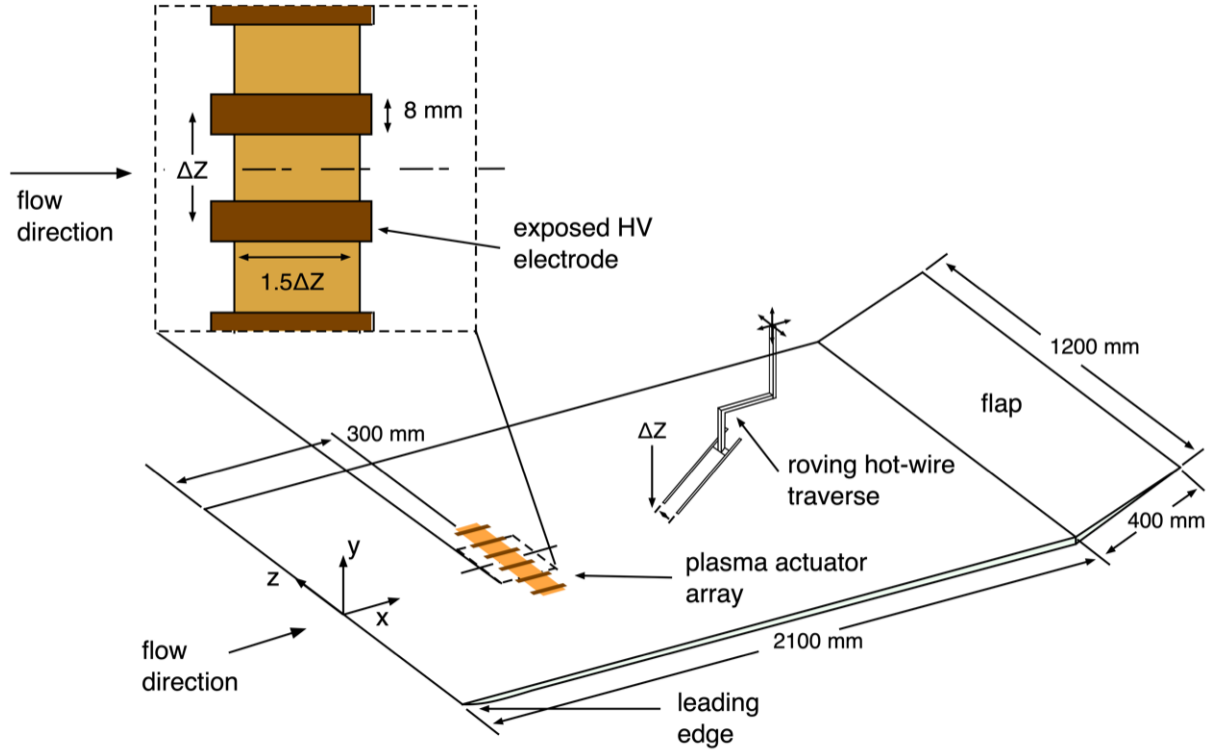
Figure 3.1: Schematic of the experimental setup and the detailed view of the control region. Figure reprinted from Hanson [14].

these sensors were controlled by a traverse system driven by a step motor; that could move in 3 dimensions. These two hot wires were located 20 mm apart and had were placed at the same height from the flat plate. The wall-normal resolution of the velocity measurement consisted of 45 point unevenly spaced for the velocities greater than 0.35% of the free stream velocity. The physical wall location was computed by a extrapolating a linear fit for 8 points between the 20 and 30% of the free stream velocity and the $U = 0$ at the wall. The spanwise measurement resolution was 1.25 mm over 32 spanwise points.

300 mm from the leading edge, a spanwise array of 6 DBDs were implemented that could produced impinging wall-jets. The DBDs' electrodes were made up of copper with 1 μm thickness and 30 mm length and 8 mm width. In order to prevent the fast degradation of

the dielectric layer which happens for Kapton-tape dielectrics, a thin layer of glass with 0.2 μm thickness was chosen. The middle of electrodes were 20 mm apart (Δz). The plasma actuators' operating voltage varied between 3.6 and 5.6 kv with the varying frequencies. However the experimental steady model with the voltage of 4.96 kv and frequency of 5 kHz is used to match the numerical steady model with. Besides, the experimental model was run to study the dynamic actuation. The applied voltage to the plasma actuators during the transient model was 5 kv with the frequency of 1.5 kHz.

3.2 Numerical Domain

3.2.1 Domain & Boundary Conditions

Simulations were performed using the finite volume solver Star-CCM+ version 2019.2.1. A schematic of the 3-dimensional numerical domain is shown in Figure 3.2. As shown, the domain is continuous, however, two distinct areas are apparent. A symmetry plane is included upstream of the no-slip wall (from $x < 0$) to best model the formation of a boundary layer
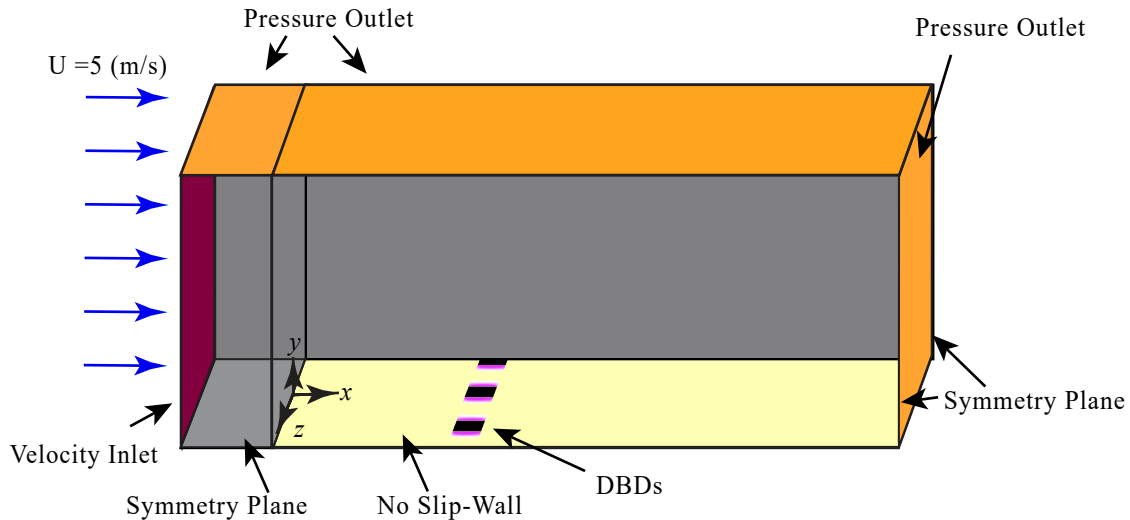
Figure 3.2: Schematic of the numerical domain representing different parts and their corresponding boundary conditions.

from the simulated leading edge at $x = 0$ mm. The section downstream of $x = 0$ on the $z - x$ plane with $y = 0$ and the length of 1000 mm, modeled as a wall with a no-slip boundary condition. The boundary layer develops from $x = 0$ in the direction of the free-stream. The boundary condition of the surface to the far right is a pressure outlet. At the top surface of the flow domain the boundary condition is also a pressure outlet. The pressure outlet at this location supports the zero-pressure gradient condition required for a Blasius boundary layer. At the outlet surfaces, the pressure is set to be zero. The backflow direction is set to extrapolated, which prevented flow into the domain. The inlet surface is specified as a uniform velocity of 5 m/s in the x-direction, which is the same as that used in the related work of Hanson *et al.* [13, 14].

A schematic of the bottom wall of the numerical domain is shown in Figure 3.3. As shown in the figure, the width of the numerical flow domain is 50 mm. The physical location of the high voltage electrodes is schematically shown in Figure 3.3, that the leading edge of electrodes is at $x = 300$ mm. The centers of the electrodes are 20 mm apart in the spanwise direction. The body forces are applied beside the edge of the imaginary upper electrodes
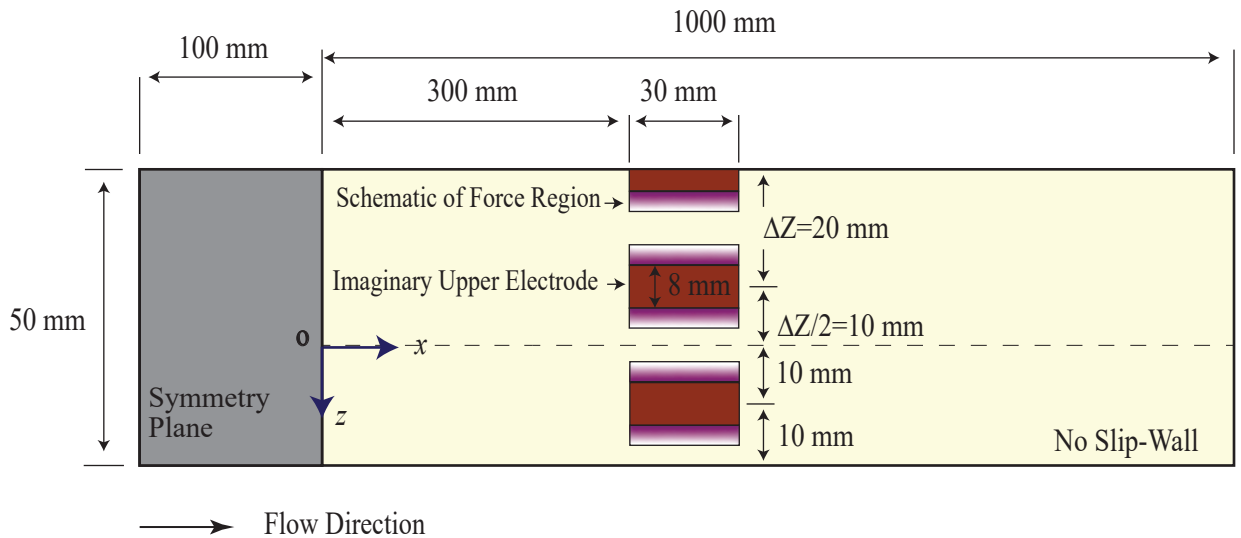
Figure 3.3: View of the bottom wall of the numerical domain and its dimensions (dimensions are not to scale). The upper electrodes and the body force regions are shown schematically.

and are shown in Figure 3.3. The width of force regions is studied parametrically and varies between 1.5 to 3.5 mm. The width of the DBDs (width of the upper electrode) and length are analogous to the experimental work since their physical structure has a direct effect on the energy content of the final disturbance; for example, Hanson studied effect of the width of the upper electrode [14]. The model simplification by reducing the number of actuators that led to a significant decrease in computational time by reducing the total mesh number becomes possible by using symmetry plane boundary condition for the side walls.

3.2.2 Physics Models & Solvers

The coupled implicit incompressible finite-volume solver was used for each simulation. The air density and viscosity were set to 1.2 kg/m^3 and 1.85 Pa·s, respectively. Thus the Reynolds number at $x = 300$ mm, where the front edge of the body force region is placed, and $x = 550$ mm and $x = 700$ mm are 9.73×10^4, 1.78×10^5, and 2.27×10^5, respectively. A second order upwind scheme is used to discretize the convection and diffusion terms of the governing equations. For the unsteady cases, an implicit scheme with second-order accuracy was used to advance the simulations in time. For the implicit unsteady scheme the time steps were fixed. The choice of time step is later discussed in Section 3.6.2. Depending on the focus of the research considered, either the steady or unsteady form of the flow solver were used. The choice of steady vs unsteady was primarily based on particular case being considered. For cases with steady and constant forcing the steady flow solver is used since the pseudo-time-marching approach enabled comparatively large steps with relatively fast convergence rate compared to the unsteady approach.

3.3 Mesh Details

Since the geometry of the flow domain is relatively simple the mesh employed contains some level of structure. A structured mesh supports reduced memory demands and data storage requirements [81], and also permits systematic study of mesh refinement. The maximum size

of the volume mesh is 4 mm in any direction. The mesh is comprised of hexahedron type elements, which are refined smaller in regions of high gradients such as with the boundary
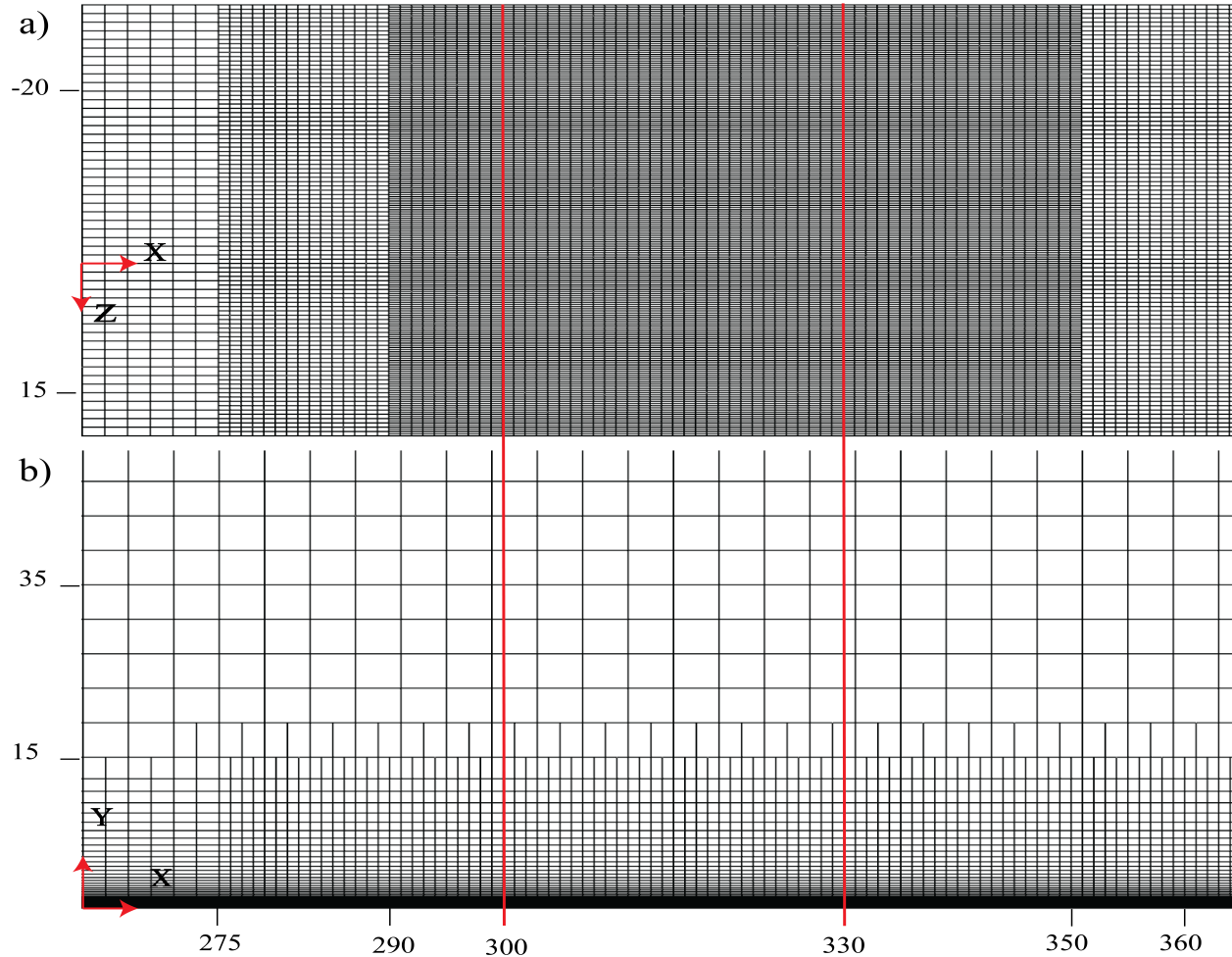
Figure 3.4: Mesh representation near the streamwise location, where the actuator effect is simulated. Red lines show the location of the leading and trailing edge of the location of forcing. (a) Top view, showing the Volumetric controls' effect.(b) Side view, illustrating growth of the prism layer. The units of the coordinate system are in millimeter (mm).

layer (using prism layers), near the simulated actuators, or near the simulated leading edge. The mesh is produced using the built-in mesh generation tools within Star-CCM+.

For the no-slip wall, prism layers are used to resolve the boundary layer. The prism layer is included over the upstream slip-wall all the way to the inlet boundary to maintain structure. A total of 50 prism layers were used, which grew geometrically with a rate of approximately

1.1. An example of the prism layer used is shown in Figure 3.4; the near-wall is not very clear because of the high density of the prisms in that region. Over a fetch of 1000 mm the predicted height of the boundary layer is 8.7 mm for an inlet velocity of 5 m/s. The total thickness of the prism layer region is 15 mm, which exceeds the maximum thickness of the boundary layer in the flow domain (for example the boundary layer is approximately 1/3 of the height of the prism layer at $x = 500$ mm).

Table 3.1: Details of the applied volumetric controls. Streamwise range, wall-noraml range and the cell size in streamwise and spanwise directions.

X Range (mm)	-100-100	-100-75	-13-13	75-250	250-275	275-290	290-350	350-520	520-620	620-770	770-1000
Y Range (mm)	0-140	0-15	0-15	0-15	0-15	0-15	0-15	0-15	0-15	0-15	0-15
Δx(mm)	4	2	1	4	2	1	1	1	2	4	4
Δz (mm)	1	1	1	1	1	0.5	0.25	0.5	0.5	0.5	1

In the streamwise direction, regions of increased mesh density are required near changes in boundary conditions or where forcing is applied. For example, near the leading edge where the bottom wall's boundary condition changes from no-slip wall to slip wall, or in the proximity of the location of the virtual actuators where a body force (momentum source) is applied.A flexible tool in STAR-CCM+ provides the ability to create the desired mesh by applying control volumes and defining the mesh size in different directions. Figure 3.4a, represents the top view of the mesh over the bottom wall near the DBDs region shown by the red lines the increase and decrease in the cell sizes are apparent in this figure. At the location where a body force will be applied to model the effect of the plasma actuator (between x = 300 and 330 mm and across the span) the x and z sizes of the mesh are 1 mm and 0.25 mm respectively. The wall normal mesh spacing is maintained as the prisms layer previously noted. The resulting grid consist of 2.76 million cells, the majority are in the prism layer region. An overview of the control volumes and the assigned streamwise and spanwise sizes are provided in the Table 3.1, all of the control volumes are stretched into the whole span, and that is the reason their spanwise size is not mentioned in this table. This mesh is used

for the simulations and the results are extracted from this gird in this thesis, whereas the effect of the mesh resolution is later described in Section 3.6.1.

3.4 Base Flow
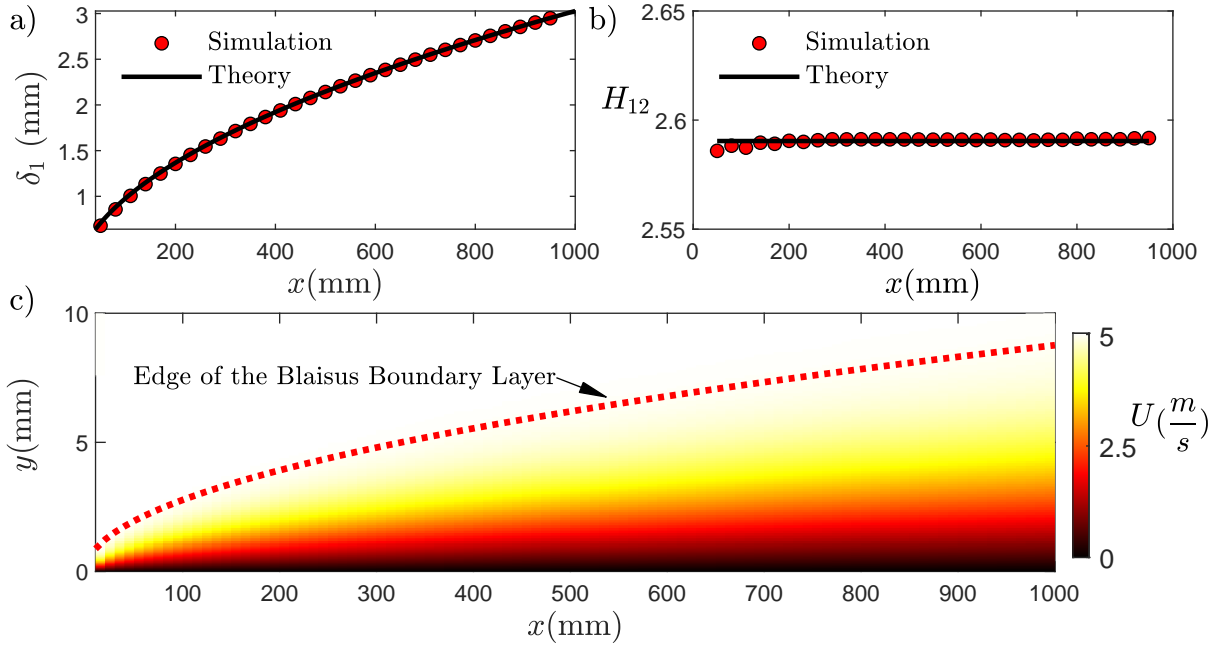
Figure 3.5: (a) Comparison of the displacement thickness for the Blasius solution (labeled as Theory) and simulation. (b) Comparison of the shape factor for the simulation and the value obtained from the Blasius solution. (c) Contour plot of the development of the streamwise velocity at a spanwise normal plane located at z = 0.

A laminar boundary layer was established over the bottom wall with the no-slip boundary condition. A comparison between the simulated laminar boundary layer and the Blasius solution is shown in Figure 3.5a. In this figure the displacement thickness (δ_1) of the Blasius solution (solid line given by $\delta_1 = 1.72(\nu x/U_\infty)^{1/2}$) is shown along with the selected data points from the simulation, which were calculated at a spacing of approximately 25 mm and

by using the following equation:

$$\delta_1 = \int_0^\infty (1 - \frac{u}{U_\infty}).\, dy, \tag{3.1}$$

where the u is the streamwise velocity component at wall-normal distance of y. Figure 3.5b shows the comparison of the shape factor $H_{12} = \delta_1/\delta_2$, in which δ_2 is the momentum thickness and is given by:

$$\delta_2 = \int_0^\infty \frac{u}{U_\infty}(1 - \frac{u}{U_\infty}).\, dy. \tag{3.2}$$

For a Blasius laminar boundary layer, the shape factor is 2.59. It is discussed in ([82], Chap 12) that the variation of the shape factor within 2.59 $\pm$0.05, which was met, is acceptably zero pressure gradient boundary layer. These results imply that the simulated boundary layer flow can be assumed to be consistent with the Blasius condition (flat wall and of zero pressure gradient). A further example of the development of the streamwise velocities over a $x - y$ plane located at $z = 0$ mm, is shown in Figure 3.5c with a dashed line demarking the edge of the boundary layer from the Blasius solution.

3.5   Simulating the Effect of the Plasma Actuator

The numerical simulations require a model to account for the effect of the plasma actuators. In this study the effect of the actuators is simulated by applying a momentum source which is defined by the a User Defined Field Function (UDF) in STAR-CCM+. A similar approach was used recently by Futrzynski [74] to simulate actuator effects on a cylinder in crossflow using STAR-CCM+. Body force modeling of plasma actuators in numerical simulations is commonly used to simulate the actuator effect, see for example [77, 83]. For the present results, a simplified method to model the body force is used. This is justified since the body force will be effectively tuned to best represent the experimental results.

A simple body force distribution which decreases linearly in spanwise and wall-normal directions similar to the Shyy model [79], is applied. The smoothness of the body force
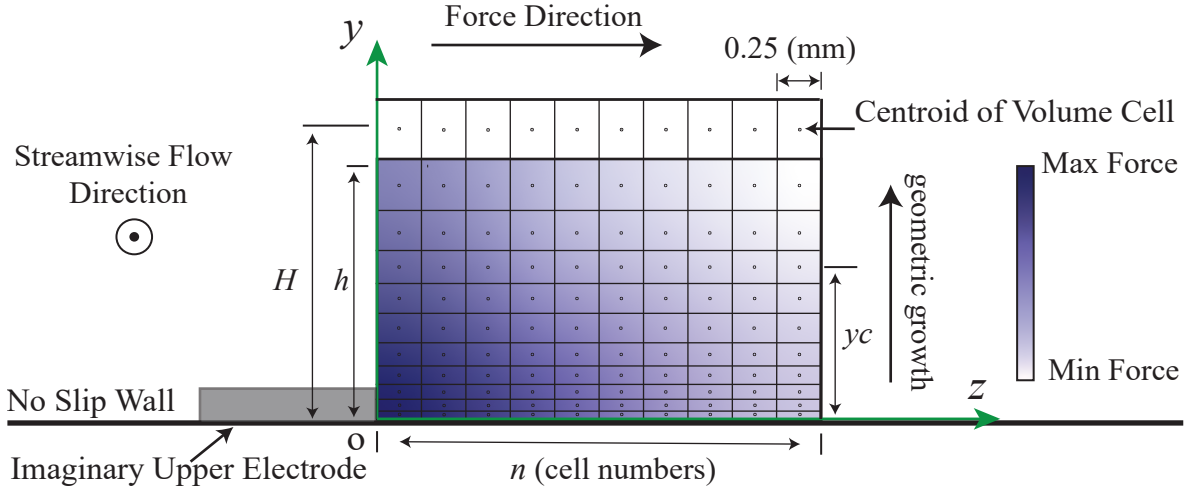
Figure 3.6: Schematic of the body force region. Mesh cells are illustrated and dots represent the cell centroids.

distribution is strongly dependent on the mesh since the value of the momentum source can only be defined for the cell volume at the centroid of the cell. Unlike the continuous plasma region in the experiment, in the simulation the effect of the actuator is from the discretized momentum sources, as it is shown in Figure 3.6, where h is the exact height of the plasma region, H is the height of the centroid of the first cell right above the force region, and n is the number of cell arrays in the span. Furthermore, unlike the triangular force region in Shyy model, as shown in Figure 2.7, the resulting force region in the current body force model is over a rectangular region. In Figure 3.6, which is a schematic of the front view of the volume cells extended into the span and wall-normal directions, the body force maximum magnitude happens near the origin. The magnitude of the force is the least for the cell at the upper right corner. The body force is only being applied in the spanwise direction.

As depicted in Figure 3.7, in which the volumetric cells are shown schematically, and named according to their streamwise and spanwise location based on the front and side edges of the imaginary upper electrode. A{k,i} represents the ith cell from the front cell edge of the plasma actuators, $x = 300$ mm, and kth cell from the side edge of the actuators. Cells
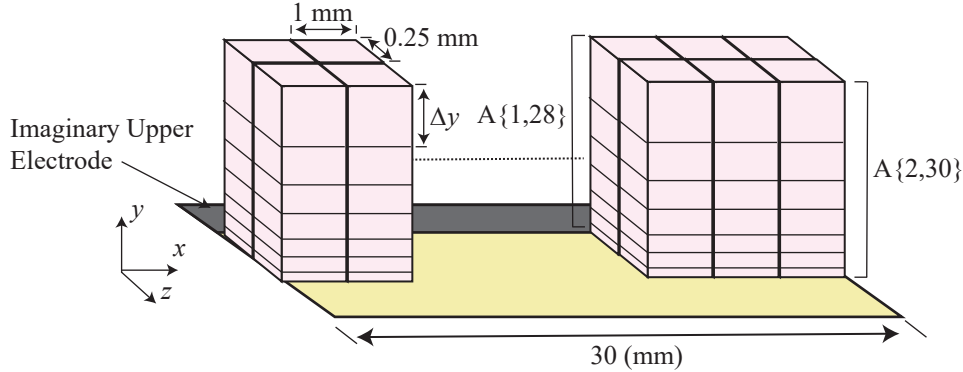
Figure 3.7: Schematic of the cell arrays near the edge of imaginary upper electrode of DBD when the spanwise width of body force is 0.5 mm ($n = 2$). Representing the first two and the last three arrays of the total 30 arrays over the whole streamwise extent of the plasma region. Two cell arrays are labeled as A{1,28} and A{2,30}.

with similar {k,i} make one cell array. For example, two cell arrays are shown in Figure 3.7 and labeled as A{1,28} and A{2,30}. Cell arrays with same distance from the side edge of the imaginary upper electrode have equal total force. For deriving the body force equation, the body force is firstly assumed to be applied in a region with the spanwise width of 0.25 mm ($n = 1$). Afterward, the body force is widened to the span. Since the height of the cells vary by the growth of the prism layers, the volume of cells are not constant. Hence, to have a linear decrease in the wall-normal direction, a body force equation is written in a way that the total force at a cell array, which results from the integration of the applied body force to the centroid over the volume of the corresponding cell, decreases linearly with respect to the wall-normal location of the cell centers.

Initially, it is assumed that the maximum applied force occurs at $y = 0$, and will become zero at $y = H$, which is shown in Figure 3.6 and is the wall-normal location of the center of the first cell after the force region. A simple linear equation based on the wall-normal location y is written and given by:

$$f_{linear}(\frac{N}{m^3}) = 0.025 \times (2 - \frac{200}{H} \cdot y_c) \tag{3.3}$$

where, y_c is the wall-normal location of the centroids for different cells in a cell array, and is shown for a cell in Figure 3.6. The first H is set to be 0.5 mm. In the second step, the body force equation is divided by the absolute of the height of the volumetric cells in a cell array and is written as:

$$f_{non-linear}(\frac{N}{m^3}) = \frac{f_{linear}}{| \Delta y |},$$ (3.4)

The applied body force to centroids, become non-linear based on the new force distribution, as shown in Figure 3.8a, which is for the case with $H = 0.5$ mm and width of 0.25 mm. In this figure it is evident, the body force magnitude is of the order of 10^3 (N/m^3) for the first cell near the wall while the magnitude of the least force is of the order of 10. When
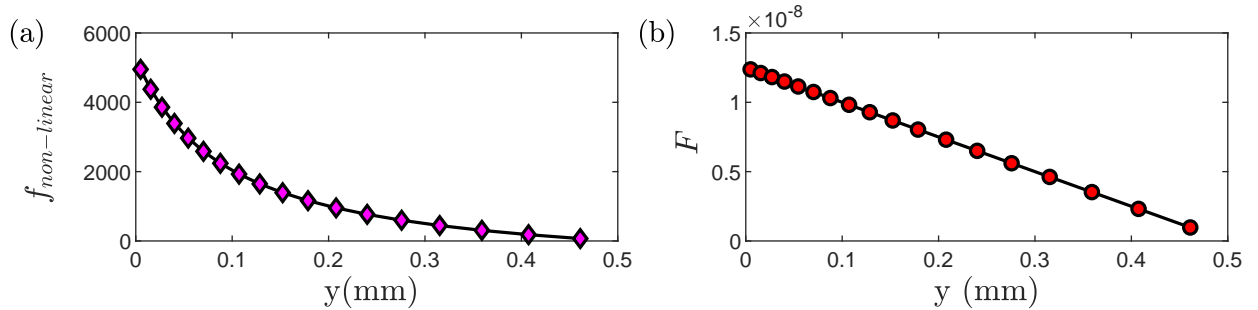
Figure 3.8: Body force distribution for one cell array near the edge of DBD for $H = 0.5$ mm and $n = 1$ or 0.25 mm. (a) Force per volume for each cell at the cell array (b) Force magnitude for each cell at the cell array.

the magnitude of the centroids are integrated over the volume of the cells, equation 3.5, the resulted body force follow a linear decrease according to the wall-normal location of the centroids. In Equation 3.5, the $dx, dy,$ and dz correspond to the streamwise, wall-normal, and spanwise size of the volumetric cells that the body force is applied to their centroids. The linear decrease of the body force in the wall-normal direction is shown in Figure 3.8b. The total applied body force at each force region will be equal to 30 times of the total force in a cell array, before expansion in span, since the streamwise length of the force regions are 30 mm which comprises 30 force arrays.

$$F(\text{N}) = \iiint f_{non-linear} dx dy dz \tag{3.5}$$

As previously mentioned in Chapter 2, the body force spanwise extent has a linear relation with the applied voltage and reaches a few millimeters. Consequently, the body force equation should be advanced to enable the spanwise distribution and parametric study on the effect of the width of the force region. The body force also has linear decrease in this direction as well. Thereupon, depending on the number of cell arrays in the span the Equation 3.4 is multiplied to a width correction factor C_w which is defined as follows:

$$C_w = \frac{n}{\sum_{i=1}^{n} i} \tag{3.6}$$

Multiplying this correction factor is not sufficient for a linear spanwise distribution, since all the arrays in span will have same total force. While the desired model has the maximum body force near the edge of the imaginary upper electrode and the lowest magnitude at the furthest cell array from the side edge. Therefore, arrays depending on their spanwise {k} number are multiplied by $(n - (k - 1))/n$, where $k = 1, 2, ..., n$, and is 1 for the first array near the edge of electrode. Figure 3.9 shows only the variation of the force in the spanwise direction for 1 vs 4 cell arrays in the span. This figure is schematically comparing two different cases. Figure 3.9a, the case when the total applied body force is ($F_T = F$) and applied to a cell array that just occupies a region with 0.25 mm width ($n = 1$). Figure 3.9b, the case when the same amount of body force body force is applied to four cell arrays in the span that has 1 mm width or ($n = 4$). For the situation with 4 arrays the $C_w = 2.5$, also the array closer to the edge of the imaginary electrode has more body force, schematically shown darker blue color.

Finally to consider the variation of the height of the force region another correction factor C_H, is introduced. To find the height correction factor, the total body force for the model with $H = 0.5$ and width of 0.25 mm ($n = 1$) is calculated as the base model. Subsequently, the total force with the new H is calculated and divided by the base model. The resulting

(a)

A{1,1} , $F_T = F$

Imaginary Upper
Electrode

y

x

z

(b)

A{1,1}, $F_T = (\frac{4}{4}).(\frac{F}{2.5})$

A{2,1}, $F_T = (\frac{3}{4}).(\frac{F}{2.5})$

A{3,1}, $F_T = (\frac{2}{4}).(\frac{F}{2.5})$

A{4,1}, $F_T = (\frac{1}{4}).(\frac{F}{2.5})$

y

x

z
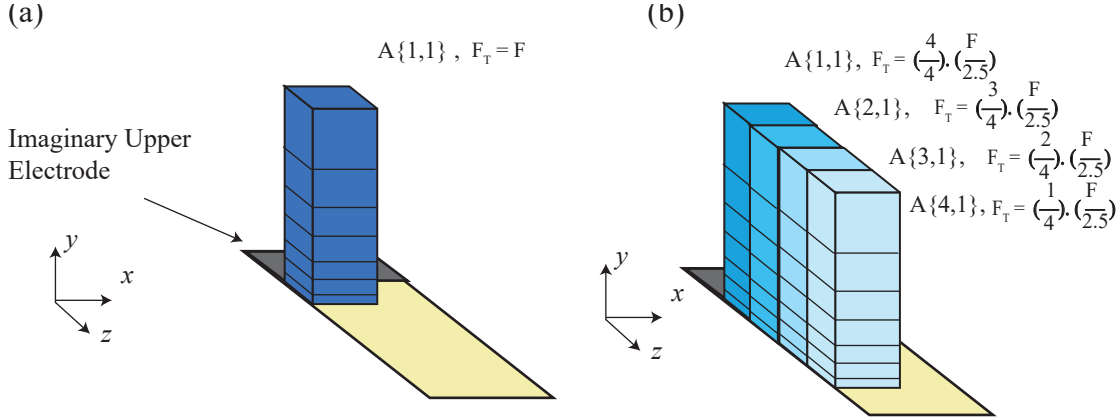
Figure 3.9: Schematic of the spanwise body force distribution for (a) one cell array, (b) four cell array. F_T is the total body force in one cell array and for the case with the with of 0.25 mm ($n = 1$) is assumed to equal to F. $C_w = 1/2.5$ for the case with four cell arrays. This figure does not show the body force distribution in wall-normal direction.

number is put in the equation as the height correction factor C_H:

$$C_H = \frac{\Sigma F_H(\text{N})}{\Sigma F_{0.5}(\text{N})}. \tag{3.7}$$

Ultimately, the UDF code for the body force that will be integrated over the cell volumes by the solver for cells in the *kth* cell array according to their centroids is given by:

$$f(\frac{N}{m^3}) = f_{non-linear}.C_w.C_H.\frac{n-(k-1)}{n}. \tag{3.8}$$

Results of the parametric study on different widths and heights are discussed in Chapter 4.

3.6 Methodology

3.6.1 Mesh Study

The objective of the mesh study is to determine the resolution of the mesh such that the flow solution is sufficiently accurate [84], The domain is divided to two types of mesh, hexahedral

cells of constant dimensions with the volumetric refinements and prisms layers (hexahedral cells that expand with distance from the wall).

Two studies were considered to determine the dependency of the results with respect to the grid or mesh employed. First, the prism layer region's discretization was considered in terms of the number of layers (cells) and the near-wall thickness. The total thickness was not varied as the value chosen was twice the maximum boundary layer thickness and therefore sufficient to fix. Secondly, to compare the existing mesh with a finer model the base size is halved. Different parameters including momentum and continuity residuals, streamwise shear stress, and generated disturbances were monitored to compare results obtained using the different meshes.

Three different number of prism layers, 32, 45, and 50, are considered, while the near-wall layer had 0.05 mm height for all of the cases, therefore changing the number of layers changes the stretch factor for the growth of the layer. For the case of 32 layers, the spanwise momentum component never converged, however increasing the number of prism layers to 45 and 50 led to the convergence of the residuals. The boundary layer as it is shown in Figure 3.10a, which shows the shape factor comparison, is near near the Blasius value 2.59 in each case. Figure 3.10b show the streamwise shear stress component along the no-slip wall for both models and the theoretical shear stress. As shown, both numerical models are in a good agreement with the theory. The Blasius shear stress (theoretical) is given by:

$$\tau_x = \sqrt{\frac{\rho.\mu.U_\infty^{\,3}}{x}}, \tag{3.9}$$

where, ρ is the flow density, ρ is the fluid density, μ is the fluid viscosity, U_∞ free stream velocity, and x is the streamwise location. The case with 45 layers appeared sufficient and similar to the case with 50 layers. However the case with 50 layers was used since it maintained a more similar growth rate of the prism layer for the smaller near-wall thickness of the first cell considered next.

Three different near-wall thicknesses, 0.05, 0.025, and 0.01 mm, are considered. Monitoring
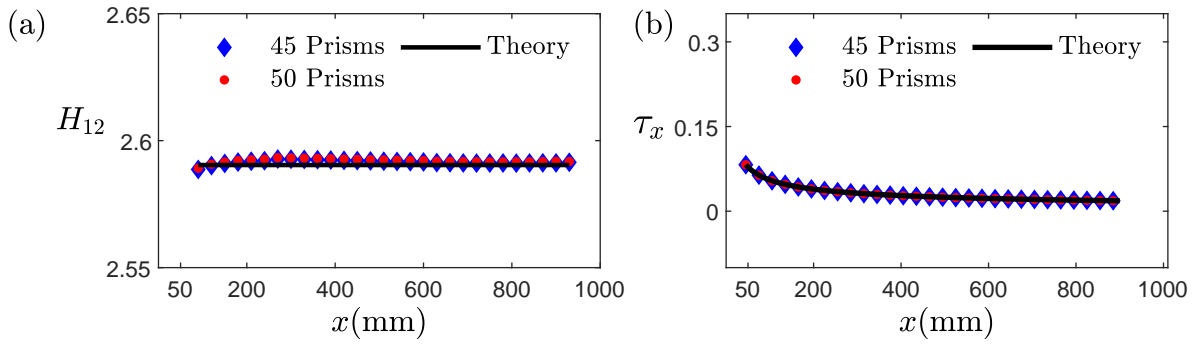
Figure 3.10: The comparison of (a) shape factor (b) streamwise shear stress for numerical models with 45 and 50 prism layers and the theoretical Blasius solution.

the momentum and continuity residuals showed faster convergence when the near-wall thickness reduced to 0.025 from 0.05. The streamwise, spanwise and wall-normal components of the momentum residuals for these two models are of the order of $10^{-5}, 10^{-2}$, and, 10^{-3} respectively. Decreasing the near-wall thickness to 0.01 mm improves the streamwise residual to the order of 10^{-6}. Considering the similarity between the established boundary layers which is evident from Figure 3.11 that shows the comparison of the shape factor and the streamwise shear stress component for all these three models, the model with higher level of convergence is selected to be used for next steps.
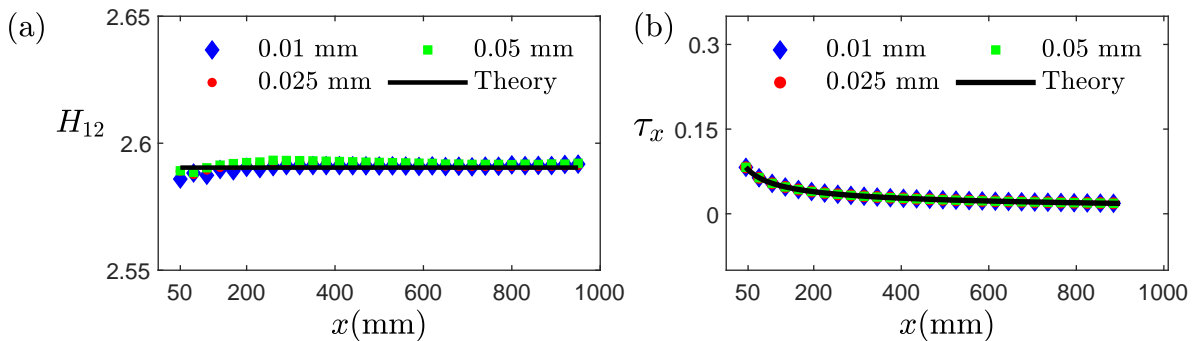
Figure 3.11: The comparison of (a) shape factor (b) streamwise shear stress for numerical models with 50 prism layers and the naer wall thickness of 0.01, 0.025 and 0.05 mm with the theoretical Blasius solution.

As previously mentioned, the body forces are applied to volume cells very close to the

wall with a very fine wall-normal size because of the prism layers. However, their length and width are 1 and 0.25 mm, respectively. To check the quality of the mesh for the applied body force, the base size is reduced to 2 mm, half of the base model, to generate a finer mesh. The volumetric controls that are used for mesh refinement, where they are required for example at the location of the body forces, are defined based on the size of the base mesh. Hence, the cell sizes inside the volumetric controls will change according to the changes of the base size. The fine grid consists of 11.64 million cells, which is nearly 4 times more than the base mesh. The disturbance due to the applied momentum source, with the magnitude of $4.399 \times 10^{-6}(\text{N})$, the $h = 0.489$ mm and width of 2.5 mm or $n = 10$ cells in the span for the base mesh and 20 cells in the fine mesh, for each plasma region, is considered for comparing the two different grids.
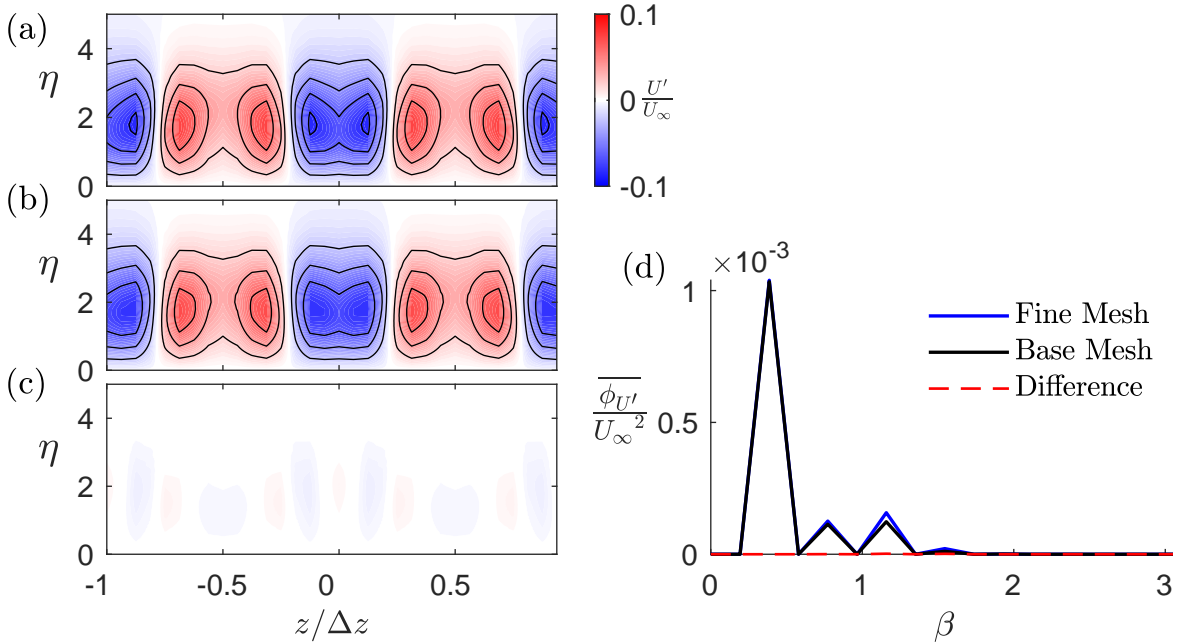
Figure 3.12: Contour plots of U'/U_∞ determined at $x = 490$ mm for (a) Fine mesh, (b) Base mesh, and (c) Fine mesh minus Base mesh. (d) The averaged spanwise wavenumber for each corresponding contour plot.

The resulting disturbances at $x = 490$ mm for the fine mesh, as are shown in Figure 3.12a, have a similar structure to the base mesh at the same streamwise location, Figure 3.12b.

The center of low-speed disturbance is at $z/\Delta z = 0$, while the high-speed disturbances are centered at $z/\Delta z = \pm 0.5$. The comparison between these two results is shown in Figure 3.12c, which represents the difference (i.e. data in Figure 3.12a with that of Figure 3.12b subtracted). In addition, the spanwise averaged power spectrum (see Equation 4.3), is shown in Figure 3.12d. The total difference in flow energy between these two models is 4.6%. The first fundamental mode's energy difference is 0.5%, while the difference for the second and third modes is 9.5% and 21.7% respectively. The difference in third fundamental mode is clearly apparent in Figure 3.12d. The models are also compared at two other streamwise locations. The total flow energy difference at $x = 450$ mm is 5.4%, and at $x = 550$ mm is 4.2%. While there may be some possible improvement in accuracy of the results of the order of 5%, the computational costs and time increase with the difference in the number of cell (nearly 4 times), is not necessary.

3.6.2   Validation of the Time Step

In this thesis the flow response to forcing is considered as the actuator is activated, held on for a period of time and then deactivated. Therefore a transient flow solver is used. The transient flow solver used is a second order implicit scheme. Although this solver is essentially unconditionally stable [84], and relatively large time steps, compared to those required by an explicit approach, may be used without loss of stability, the time steps must be sufficient small to accurately resolve the transient flow response, while large enough such that the cost of the simulation (total run time) is minimal. The first choice for the time step is calculated based upon the Courant number definition, in a way that this parameter is equal to one. Courant number (C) is defined as:

$$C = \frac{U\Delta t}{\Delta x} \tag{3.10}$$

where U is the flow velocity, Δt is the time step, and Δx is the grid spacing. The presence of the boundary layer causes the flow velocity to vary from the free-stream to the no-slip condition at the wall. As a first estimate a velocity of U pertaining the free-stream value (5

m/s) for calculation of the courant number is used such that that the flow only passes one cell length (when $C = 1$) in the streamwise direction at each time step. For this to be maintained, the value of Δx corresponds to the smallest cell size in the direction of the free-stream in the domain, 1 mm. Hence the time step with $C = 1$, is 2×10^{-4}(s). Three other time steps are considered for this study, half, twice and four times the case with 2×10^{-4}(s). The four time steps considered in this study are referred to as Δt_1, Δt_2, Δt_3 and Δt_4, which corresponds 1×10^{-4}(s), 2×10^{-4}(s), 8×10^{-4}(s), and 8×10^{-4}(s), respectively.
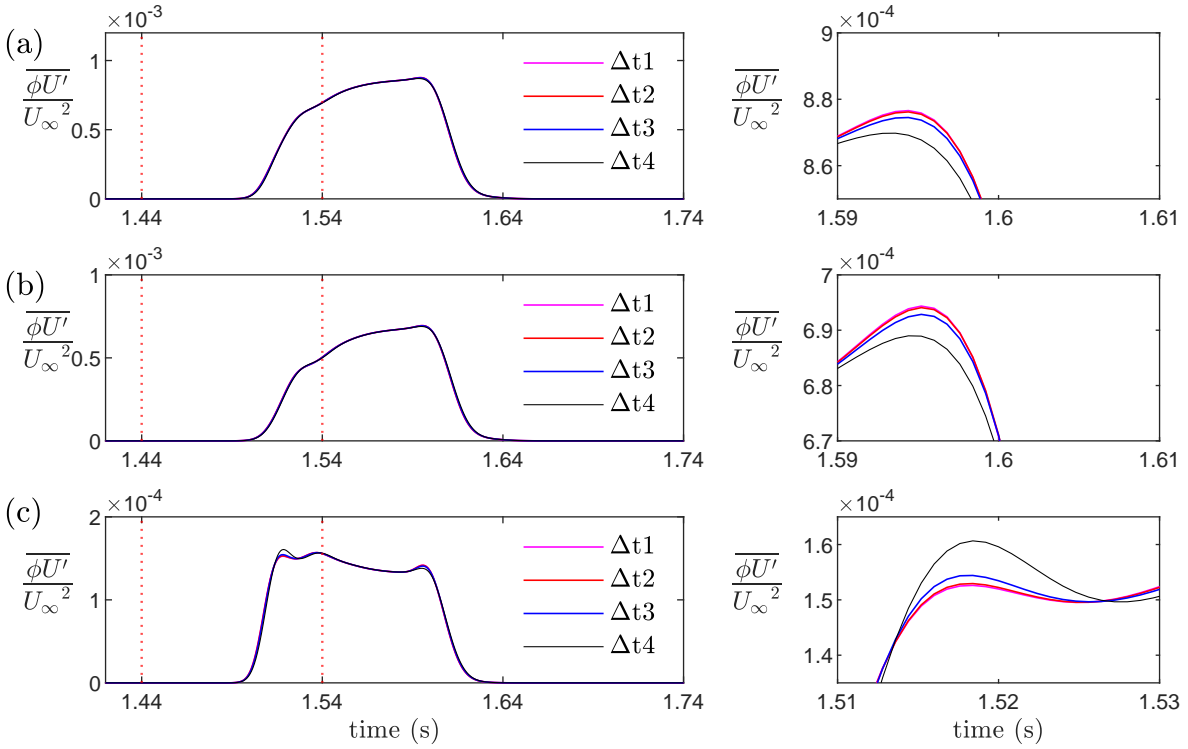
Figure 3.13: Development of the disturbance energy as a function of time for the (a) total or unfiltered energy (b) first fundamental mode (c) second fundamental mode. Red dashed lines representing the range when plasma is on. $\Delta t_1 = 1\times10^{-4}$, $\Delta t_2 = 2\times10^{-4}$, $\Delta t_3 = 4\times10^{-4}$, $\Delta t_4 = 8\times10^{-4}$.

Although the transient behavior of the different modes is discussed in Chapter 5, their peak values for different models with different time steps are compared in here to find an acceptable time step without significant accuracy penalty. Each of the simulations were

considered converged (low residual values and constant total shear stress reached) when the baseline Blasius boundary layer was established, typically after 1.44 seconds of total simulated time. Next the body force source term with magnitude of 4.308×10^{-6}N, width of 3.5 mm or 14 number of cells in span, see Figure 3.7, and the exact height of 0.382 mm is enabled for the duration of 0.1s and then disabled. The simulations are permitted to run for an additional 0.2 seconds to permit the disturbance to convect downstream. The development of the average spanwise wavenumber power spectrum is calculated by Equation 4.3. A plane at the 490 mm from the leading edge, is considered to extract the transient data for time steps comparison.

The overall development of the flow energy and the first two fundamental modes in time for each of the time steps appears similar as shown in the left column of Figure 3.13(a, b, and c). The zoomed plots on the right side of the Figure 3.13 better show the differences for each time steps. The maximum total energy for the Δt_2 (base time) happens at t = 1.5944s or 0.0544s after the time when plasma is turned off. This is the same for Δt_1, and Δt_3 however, for Δt_4 is different and happens at t = 1.5936s. Δt_1, is 0.046% greater compare to Δt_2. While the differences for the Δt_3 and Δt_4, are 0.192, and 0.731 % less, compared to the selected base time (Δt_2). For the second fundamental mode, the difference between the maximum value for the Δt_4 and Δt_2 time steps becomes more evident. Δt_4 has 2.40 % more energy while Δt_3 has 0.05 % compared to Δt_2. Also, the maximum magnitude for Δt_4 happens 0.0184 seconds earlier. Ultimately, the time step of $\Delta t_3 = 4 \times 10^{-4}$s is considered a reasonable balance between accuracy and computational costs.

Chapter 4

Simulation of Steady Streaks

4.1 Overview

In this Chapter, the related steady state experimental results of the boundary layer response to steady forcing by a spanwise array of plasma actuators of Hanson *et al.* [12], are simulated numerically using a momentum source term. The overarching research objective considered in this chapter is achieve comparable streaks in the numerical stimulation of the laminar boundary layer. Comparisons between the simulation and the experiments are made with respect to both amplitude and spatial distribution of the streaky disturbance at a downstream location where the corresponding experimental measurements were acquired. The model of the force distribution was previously described in Section 3.5. In this chapter the three key parameters considered using the modified version of a Shyy model [79] (rectangular forcing domain with linear force variation) are the body force (a) magnitude, (b) width, (c) height. The last two parameters are the geometrical variables depicted in Figure 3.6. Six force magnitudes, three different heights, and five widths are considered. To isolate the influence of a single variable, the two other variables are kept constant. From the parametric study, a suitable combination of these parameters is chosen to represent the momentum source magnitude and spatial distribution to model the plasma actuators in the transient flow simulation of the boundary layer step response to forcing.

4.2 Overview of the Experimental Results

In the related experiments of Hanson *et al.* [14, 12, 13], the magnitude of the forcing was varied by the voltage and frequency of the sinusoidal waveform applied to the exposed electrode of the plasma actuators. In this chapter a single characteristic steady actuation case of 4.96V and 5 kHz is considered since this case is most similar to that later applied in the case of the dynamic actuation, which is the main focus of the present research. For the latter case of the step response to forcing discussed in Chapter 5, the voltage was only marginally more ($\sim$5% higher), which resulted in a higher disturbance magnitude. The parametric optimization of the simulated disturbance is best suited for the steady actuation case given the lower computational costs (run time on the order of nearly 1/6th of the transient simulation). However, the latter transient simulations are the main research focus.

For the comparable experiments, the measurement plane in the spanwise (z) and wall-normal (y) direction is located at a $x = 490$ mm from the leading edge. A schematic of the experimental setup was shown previously in Figure 3.1. The generated disturbances are small (i.e. typically less than a 10% deviation from the Blasius profile) and therefore the spanwise average of the is a boundary layer is approximately the Blasius solution. The disturbance velocity U' is calculated by subtracting the spanwise averaged velocity U_{tz} from the time-averaged velocity U_t and can be defined as:

$$U' = U_t - U_{tz}. \tag{4.1}$$

It was shown earlier by Hanson *et al.* [13] the streaks of alternating low and high velocity in the boundary layer tend to be primarily comprised on a spatial spanwise wavelength of length Δz, which is the spacing between the exposed electrodes of the spanwise array of plasma actuators. However, additional energy content at shorter wavelengths of $\Delta z/i$, where i is an integer number, was present. The ratio of energy at these wavelengths shorter than Δz decayed downstream, such that the ratio of energy at the wavelength Δz increased

downstream, meaning that the flow profile appears to be of a single wavelength far downstream. That said, the energy of the total disturbance at a measurement plane can be expressed as a sum of the contributions of the energy at each spanwise wavelength, viz.

$$\Sigma\phi_{U'}(\beta) = \sigma(U')^2, \tag{4.2}$$

where β is the dimensionless spanwise wavenumber and is equal to $2\pi\delta/\lambda$ in which δ is the Blasius similarity length scale, and λ is the spanwise wavelength. The fundamental wavelength is defined by Δz, which is the spacing between the simulated or real electrodes of the plasma actuators. In the experiments, velocity profiles were measured at a spacing of $\Delta z/16$ over a spanwise distance of $2\Delta z$. The resulting one-sided spectrum has a resolution of $\Delta z/8$ owing to the 16 boundary layer profiles per Δz. The average energy content of the disturbance velocity over the height of the boundary layer is given as a function of β by:

$$\overline{\phi_{U'}}(\beta) = \frac{\int_0^{5\delta} \phi_{U'}(\beta)d\delta}{5\delta}. \tag{4.3}$$

As shown in Figure 4.1a, the disturbance includes low speed streaks that are centered at $z/\Delta z = -1, 0, 1$ and high speed streaks that are centered at $z/\Delta z = \pm 0.5$. The streaks appear double-peaked, in particular for the high-speed regions. This observed spatial distribution can be explained as a result of the summation of different spanwise wevelength disturbances having integer values of $\lambda_i = \Delta z/i$, where i = 1, 2 and 3, which corresponds to $\beta = 0.38, 0.76$, and 1.13 respectively. As shown in Figure 4.1b, these three modes are the most energetic, and contain 69%, 12.7%, and 11.4% of the total energy. These three modes also contain approximately 93% of the total energy.

The spatial distribution of U'/U_∞ is shown in Figure 4.1c, d and e for the band pass filtered disturbance at at modes 1, 2 and 3 or having a spanwise wavelength of Δz, $\Delta z/2$, and $\Delta z/3$, respectively, while the colorbar levels is different for each of these figures. The energy level decreases in descending order of the wavenumbers. The first mode (Figure 4.1c), and the second mode (Figure 4.1d), are in the same phase at $z/\Delta z = 0$ while the third
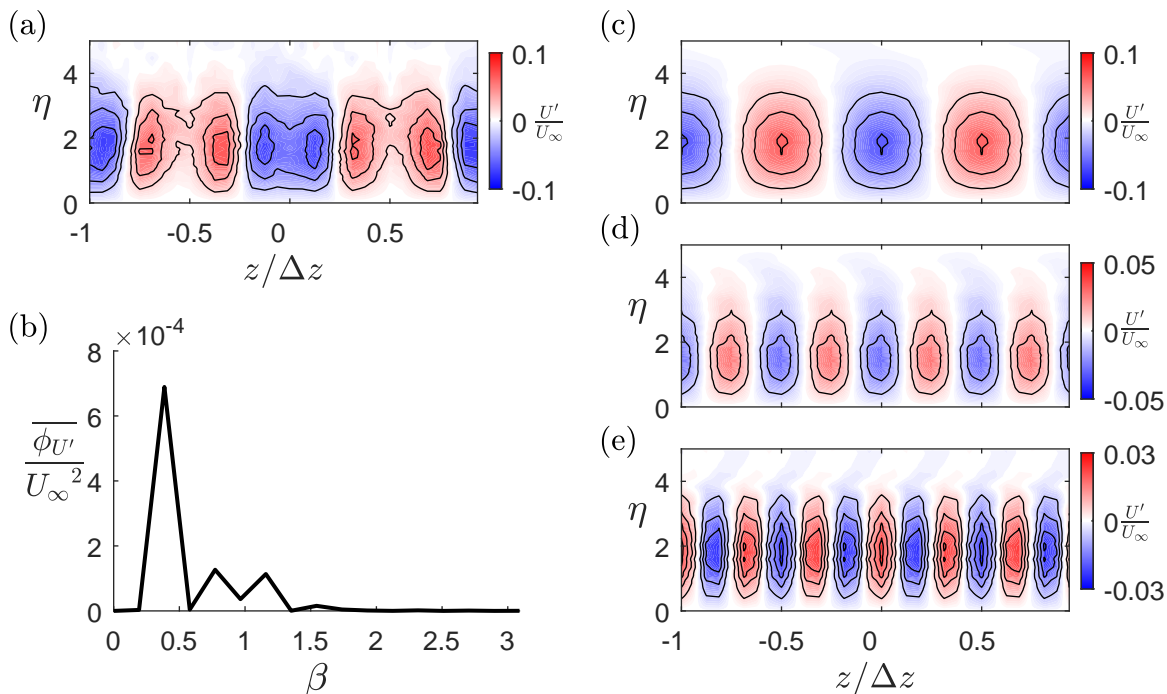
Figure 4.1: Example experimental result from the dataset of Hanson [14]. Velocity contours of the streamwise disturbance U'/U_∞ for (a) unfiltered disturbance, (c) first mode, (d) second mode (e) third mode. (b) average spanwise wavenumber power spectrum of the disturbance velocity measured at $x = 490$ mm.

mode (Figure 4.1e) has opposite phase at that location. On the other hand, at $z/\Delta z = \pm 0.5$, the second and third modes have the same phase, opposite to the first mode. As a result, high-speed streaks are more double-peaked than the low-speed ones.

4.2.1 Parametric Study of the Body Force

A parametric study on the effect of the simulated body force was conducted. The three variables considered in this study are the force magnitude (Subsection 4.2.2), width (Subsection 4.2.3) and height (Subsection 4.2.4) of the forcing region. In total 5 different forcing widths, three different heights and 6 different force magnitudes are included in the following sections. The plasma region is continuous, however, in all of the simulated models the geometrical parameters, as discussed in Chapter 3, are dependent on the mesh resolution. An initial

44

exploratory study was conducted to identify the range of the three variables (height, width and magnitude) that are considered in this parametric study, and this study is not discussed for brevity.

4.2.2 Effect of the Magnitude of the Forcing Region

The process that was used to predetermine the values of the momentum source term applied at each cell within the modeled plasma region was previously explained in Section 3.5. As discussed in that section, and schematically shown in Figure 3.6, the simulated momentum source (or body force) will vary linearly for the model being applied. The peak value occurs within the cell having an edge where the physical exposed electrode would be in the experiment (i.e. see Figure 3.6). For different heights and different widths, a linear variation of the body force is studied. However, only the results for $H = 0.5$ mm and width of 3.5 mm ($n = 14$) will be presented. The body force varies between 0.6F and 1.1F in every side of the plasma actuators in the case when $F = 4.399 \times 10^{-6}(N)$, this force magnitude referred to in following discussion as the base force, and is denoted by F_b. The ratio of other magnitudes are expressed by F/F_b. Figure 4.2 shows the disturbance velocities and the corresponding first three fundamental modes for various force magnitudes. The increase in the velocities for the unfiltered, the first and second fundamental wavenumbers are evident. However, the third wavenumber appears less sensitive compared to other wavenumbers. Furthermore, it is indicated that the first mode has the same sign with the second mode at $z/\Delta z = 0$. In contrast, the third mode has opposite sign at that location. Moreover, at $z/\Delta z = \pm 0.5$ first mode is in the opposite sign of the second and third mode. Consequently, the variation of the body force magnitude does not lead to phase shift for the first three fundamental wavenumbers.

Figure 4.3a shows the average spanwise wavenumber power spectrum for different body force ratios. As shown, the first three modes contain most of the flow energy. The total energy contained in the first three modes for each case was at least 99%. Increasing the body force ratio, in a region with constant height and width, leads to the increase in the energy of
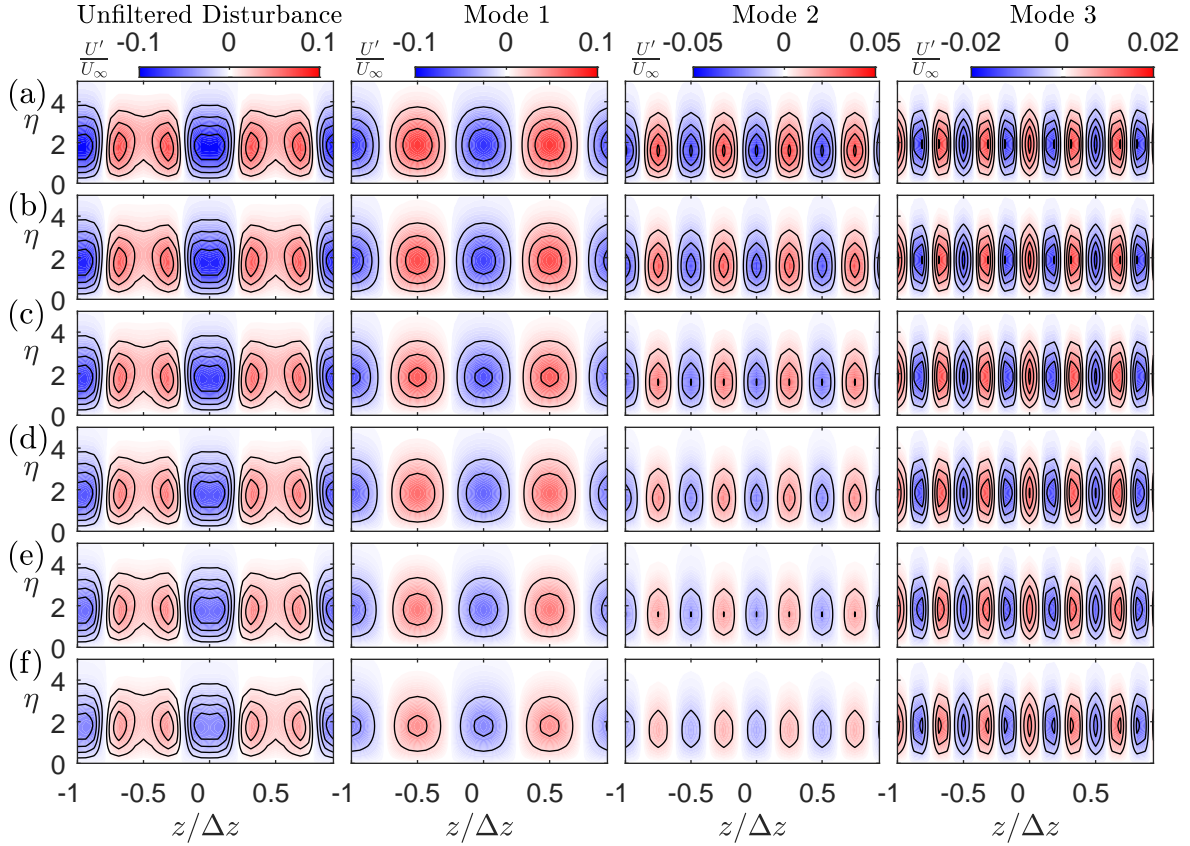
Figure 4.2: Contour plots of the unfiltered disturbance velocity and the first three fundamental wavenumbers at $x = 490$ mm when $H = 0.5$ mm and width of 3.5 mm ($n = 14$), and (a) $F/F_b = 1.1$, (b) $F/F_b = 1$, (c) $F/F_b = 0.9$, (d) $F/F_b = 0.8$,(e) $F/F_b = 0.7$, (f)$F/F_b = 0.6$.

mostly the first and second mode of the energy, while, the third mode shows less changes. Table 4.1 includes the energy ratio of the first three modes and their overall fraction of the total energy. The energy ratios of the first and third modes, unlike their absolute values, decrease by increasing the body force. The energy ratio of the second mode had increased by increasing the force. The sum of the energy ratio of the first three modes decreases by increasing the body force, implying that higher harmonics are intensified. Figure 4.3b shows the profiles of spanwise root-mean-square (rms) of the disturbance velocity, calculated over the height of the boundary layer. As shown the wall-normal location of the maximum disturbance velocity appears nearly constant at a value of approximately $\eta = 1.8$ for the range
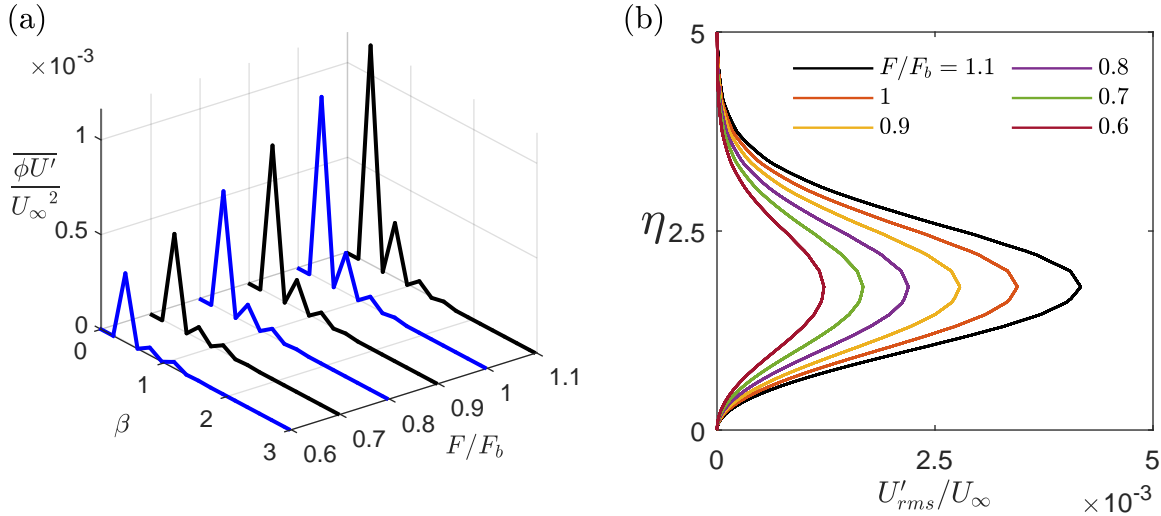
Figure 4.3: Waterfall plot of the average spanwise wavenumber power spectrum for different force magnitudes, $H = 0.5$ mm and width of 3.5 mm ($n = 14$), measured at $x = 490$ mm. (b) wall-normal profile (U'_{rms}) for the unfiltered disturbance for different force magnitudes.

of force magnitudes considered. While the wall-normal location of the maximum disturbance velocity for an optimal disturbance with the spanwise wavenumber of $\beta = 0.45$ occurs at $\eta = 2.2$ [11].

Table 4.1: Energy ratio of the first fundamental wavenumbers for $H = 0.5$ mm and width of 3.5 mm ($n = 14$) and varying force magnitude for the disturbance measured at $x = 490$ mm.

F/F_b	0.6	0.7	0.8	0.9	1	1.1
$E_1/E_t(\%)$	82.79	81.55	80.26	78.94	77.62	76.30
$E_2/E_t(\%)$	9.18	11.16	13.19	15.23	17.24	19.21
$E_3/E_t(\%)$	7.44	6.61	5.78	4.98	4.23	3.52
Sum(%)	99.43	99.33	99.24	99.16	99.09	99.04

4.2.3 Effect of the Width of the Forcing Region

It was previously discussed in Section 2.4.5 that the plasma extent, or region where the body force is generated, varies with the applied voltage. Therefore, the extent or width of

the plasma region as defined in Figure 3.6 is considered. Furthermore, with respect to the spatial distribution of the body force region, it was also shown by Hanson *et al.* [14] that the location of the forcing strongly affects the energy distribution of modes 1, 2 and 3. The width of the force region can only be varied incrementally based on the dimensions of the cells in that region. In the forcing region, the cell widths were 0.25 mm, and in this study,
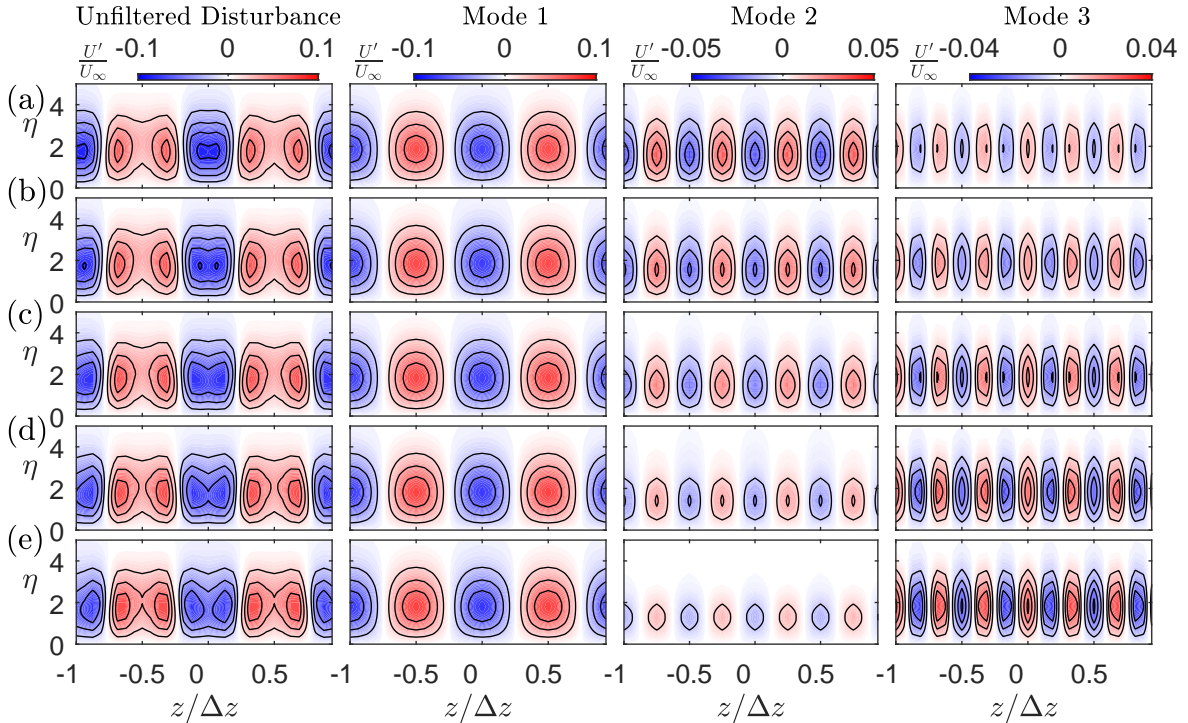
Figure 4.4: Contour plots of the unfiltered disturbance velocity and the first three fundamental wavenumbers at $x = 490$ mm when $H = 0.5$ mm and $F = F_b$, and widths (a) 3.5 mm ($n = 14$), (b) 3 mm ($n = 12$), (c) 2.5 mm ($n = 10$), (d) ,(e) 2 mm ($n = 8$), (f) 1.5 mm ($n = 6$).

widths varying linearly in increments of 0.5 mm were considered from 1.5 mm to 3.5 mm or 6 to 14 cells. Figure 4.4 shows the contour plots of the unfiltered and bandpass filtered mode 1, 2 and 3 of the disturbance velocity for each width at the constant body force of F_b and height of $H = 0.5$ mm. As shown from the unfiltered disturbance for a width of 3.5 mm the positive disturbance velocity region centered about $z/\Delta z = \pm 0.5$ is more double-peaked compared to the region at $z/\Delta z = 0$. For the narrower body forces, for example, the width of 1.5 mm Figure 4.4e, at $z/\Delta z = 0$, the unfiltered disturbance looks doubled-peak. Looking at

the band-pass filtering results for the U'/U_∞ shows that by increasing the width of the body force, although the first fundamental wavenumber (Δz) is the dominant mode, the second mode is amplified. On the other hand, the third mode attenuated. Due to these changes in the modes, the overall structure of the disturbance changes by the width of the body force. Figure 4.4 also demonstrates that the phase of the different modes is not affected by the variations of the width of the body force.

The spanwise averaged power spectrum of the disturbance velocities for different widths (Figure 4.5a) also indicates that the flow is almost missing the second mode when the body force width $= 1.5$ mm ($n = 6$), and as mentioned in the Table 4.2, the energy ratio of this mode is 1.99%, while for the third mode is 15.15%. Moreover, for all models, the first three wavenumbers contain more than 99% of the flow energy. This implies that widening the force region does not amplify the higher harmonics. The total flow energy, caused by the same amount of force, for the $n = 14$ is 4.96, 3.62, 2.52, and 1.40 % less than the $n = 6$, $n = 8$, $n = 10$, and $n = 12$ respectively. Hence the wider the force region, the lower the added energy to the flow. The lower energy stems from the increase in the drag penalty caused by the increase in the surface area where the body force is imparted [73].

Figure 4.5b, shows that distributing a constant force magnitude in the spanwise direction, does not change the wall-normal location of the maximum unfiltered disturbance velocity; and it happens at $\eta = 1.8$. However, as shown, peaks of the wall-normal disturbance velocity profiles are in descending order of the flow energy, and the model with the model with the width of 3.5 mm ($n = 14$) has the lowest peak.

Table 4.2: Energy ratio of the first three fundamental wavenumbers for $H = 0.5$ mm constant force magnitude F_b with a varying width.

width (mm)	1.5	2	2.5	2.5	3.5
$E_1/E_t(\%)$	82.40	81.70	80.58	79.18	77.62
$E_2/E_t(\%)$	1.99	4.97	8.87	13.11	17.24
$E_3/E_t(\%)$	15.15	12.61	9.63	6.70	4.23
Sum(%)	99.54	99.29	99.08	99.00	99.09

(a)

(b)
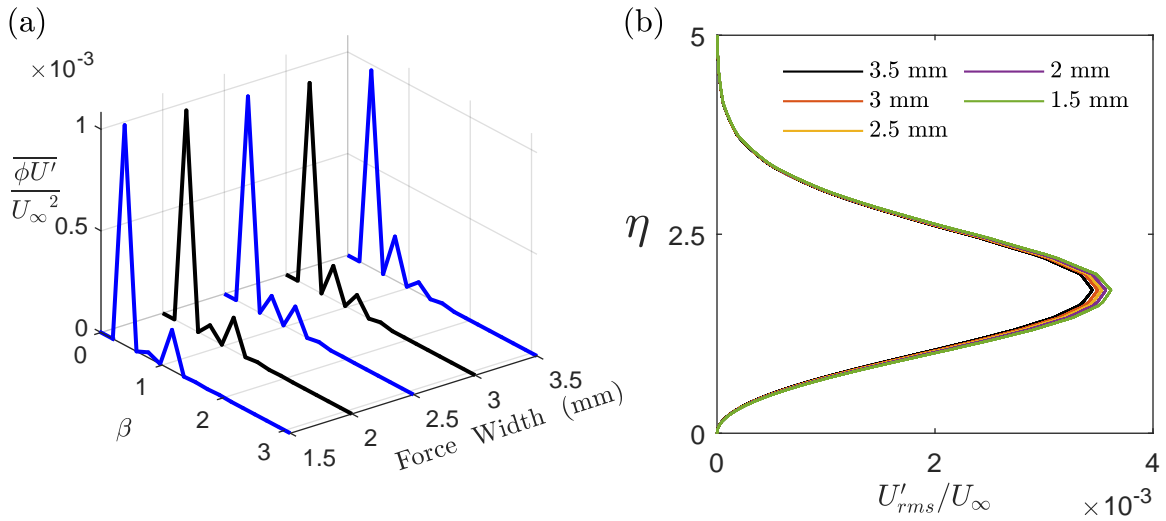
Figure 4.5: (a) Waterfall plot of the average spanwise wavenumber power spectrum for different force widths and height of $H = 0.5$ mm and magnitude of F_b, measured at $x = 490$ mm. (b) Wall-normal profile for the unfiltered disturbance for different force width.

4.2.4 Effect of the Height of the Forcing Region

The last parameter considered for the force volume is the height of the force region (given by H, as is shown in Figure 3.6). Three different heights of $H = 0.4$, 0.5, and 0.73 mm are considered. Where H corresponds to the wall-normal location of the centroid of the first cell after the edge of the last cell in the force region. Therefore, the edges of the corresponding force regions that are denoted by h in Figure 3.6 will be located at 0.382, 0.489, and 0.635 mm respectively. The C_H, which is the height constant in Equation 3.8, is 1.135, 1, and 0.821 for each of these heights, respectively. Here, the results of the constant body force of F_b and the constant width of 3.5 mm ($n = 14$) for three heights are compared. Figure 4.6 represents the disturbance structure and the modal decomposition of the first three fundamental wavenumbers. The attenuation of the disturbance velocity by decreasing the height of the body force region, while the total body force remained constant, is evident in the contour plots shown in Figure 4.6a, b, and c. As shown by Font *et al.* [73] when for the same body force produced by the plasma actuator, if applied nearer the wall, the wall
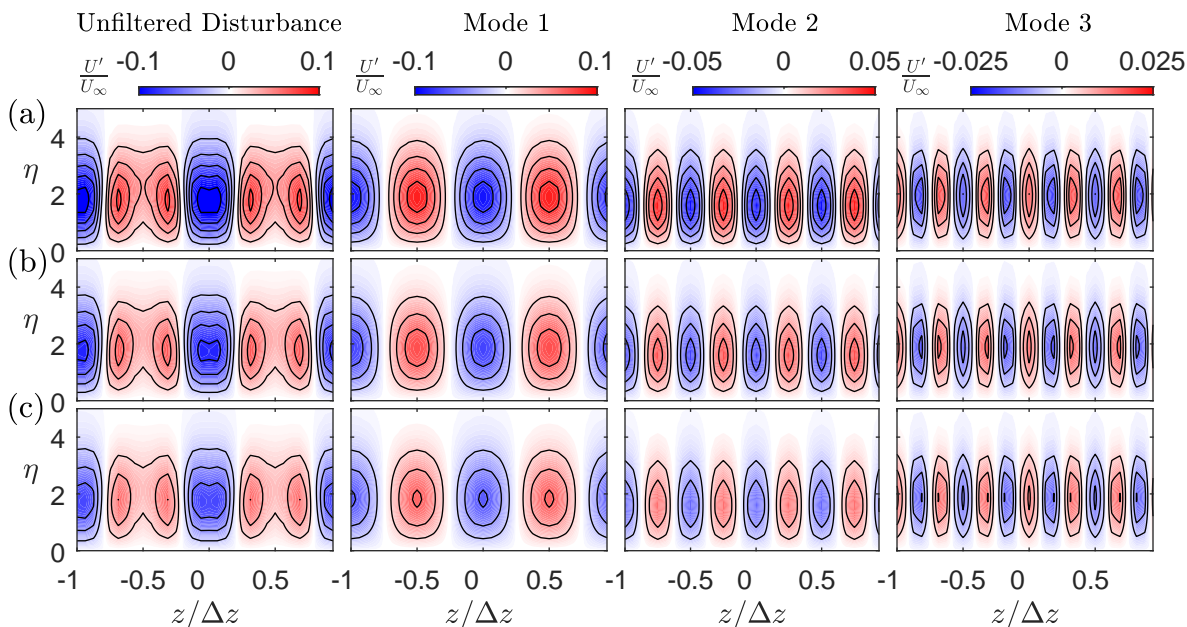
Figure 4.6: Contour plots of the unfiltered disturbance velocity and the first three fundamental wavenumbers at $x = 490$ mm when the force region's width is 3.5 mm ($n = 14$), with the magnitude of $F = F_b$, and (a) $H = 0.73$ mm, (b) $H = 0.5$ mm , (c) $H = 0.4$ mm.

drag will be greater and the less net body force will be applied to the surrounding air. This rational appears consistent with results shown in this study where the magnitude of the velocity disturbance decreased with the educed height. The height variation also shows no effect on the phase of the resulted disturbance at $x = 490$ mm from the leading edge.

The change in the total energy with respect to the disturbance velocity can be quantified using the spanwise power spectra that was averaged over the boundary layer thickness as shown in Figure 4.7a. From this figure the significant increase in the first and second modes by increase in the height of the force region is observable. In addition, the total energy has increased. For instance, the total energy calculated over the first 8 wavenumbers shown in Figure 4.7a, for $H = 0.5$ mm is 37% less than the case with $H = 0.73$ mm while this difference for the case with $H = 0.5$ mm is 54%.

However, the first three modes are still having more than 99% of the total energy. The contribution of the first mode to the total disturbance energy decreases by increasing the height of the force region, as pointed in Table 4.3. Similarly, the third mode has decreased,
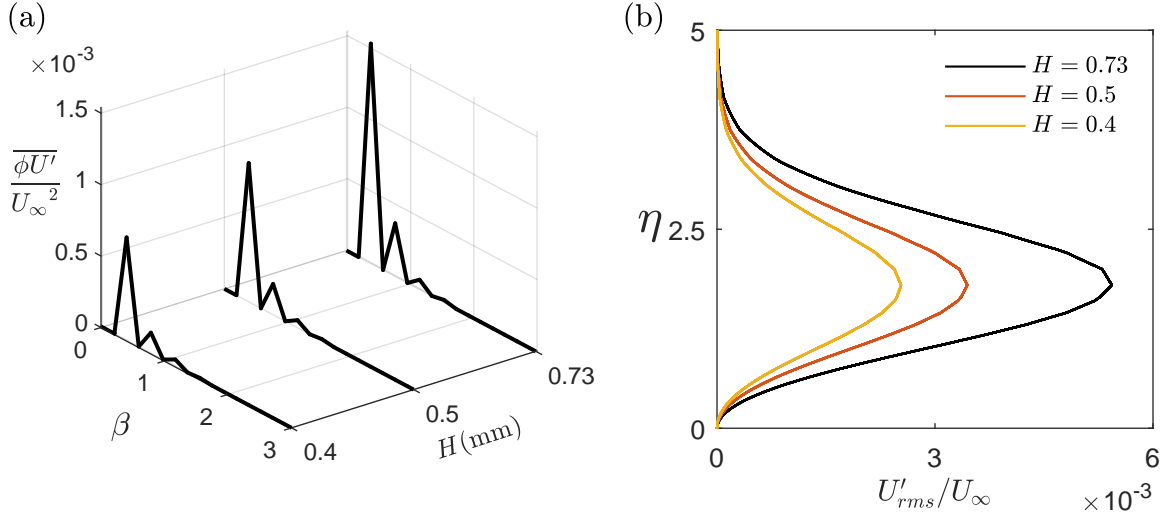
Figure 4.7: (a) waterfall plots of the average spanwise wavenumber power spectrum for varying force region height and constant width and force magnitude, measured at $x = 490$ mm. (b) wall-normal profile (U'_{rms}) for the unfiltered disturbance for different force heights.

while the second mode has shown increase in its energy ratio. The same behavior was previously observed for the variation of the force magnitude. Figure 4.7b indicates that despite the differences in the wall-normal velocity profiles for the different heights, the maximum is still happening at nearly $\eta = 1.8$ for all heights.

Table 4.3: Energy ratio of the first three fundamental wavenumbers for $n = 14$ constant force magnitude F_b and varying height.

H(mm)	0.4	0.5	0.73
$E_1/E_t(\%)$	78.54	77.62	77.05
$E_2/E_t(\%)$	15.87	17.24	18.64
$E_3/E_t(\%)$	5.00	4.23	3.42
Sum(%)	99.12	99.09	99.11

4.3   Matching of Simulation and Experiment

In the related experiments the first mode (with spanwise wavelength Δz) contained the majority of the disturbance energy ($\sim 69\%$) and the first three modes contained up to 93% of

the total energy. In the numerical simulations nearly 99% of the total energy was contained in the first three modes. Although minor, the discrepancies may be attributed to differences between the simulation, the modeled body force and the physical experiment. The objective of this section is to determine the approximate combination of variable considered which minimizes the difference between the simulated boundary layer disturbance of streaks and those of the experiment.

The variation of the first mode for constant height $H = 0.4$ mm, varying widths and force magnitudes is plotted in Figure 4.8. In this figure, the dotted blue line corresponds to value of the energy contained in the first fundamental mode as given by equation 4.3 for the spanwise wavelength of Δz, in the experimental model. Second-order polynomial lines are fitted over the first energy modes. Subsequently, F/F_b, calculated where the horizontal line corresponding to the averaged energy in the experiment intersects the lines fitted to the points considered in the simulations. For instance, in Figure 4.8, the range of the intersection points are all in the range of 0.9 to 1. The same approach is also applied to two other heights.
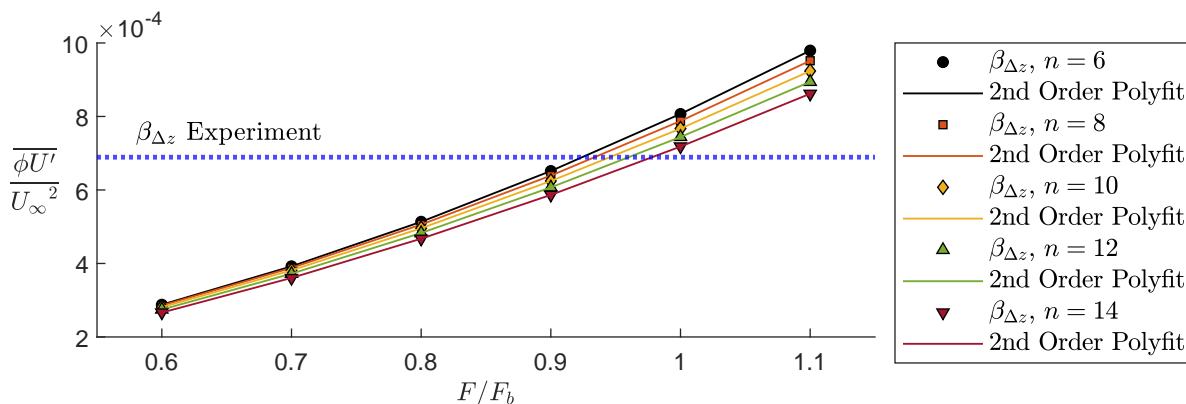
Figure 4.8: First fundamental mode's energy growth for constant $H = 0.4$ mm and varying force and width, and the corresponding mode for the experiment at $x = 490$ mm.

The interpolated values for F/F_b, based on heights and widths, are provided in Table 4.4. According to the results of Section 4.2.4, higher force magnitudes are required when the force region has a lower height. The expected required forces are then simulated to the result in an approximate match of the mode 1 disturbance. The resulted disturbances are measured

at the same streamwise location, $x = 490$ mm. Spanwise averaged power spectrum is again calculated for the models with using equation 4.3 over the height of the boundary layer ($\eta = 5$). The resulted energy corresponding to the first three wavenumbers is plotted in Figure 4.9. In this figure the black, blue, and red dashed lines represent the first, second, and third mode of the experiment, respectively.

Table 4.4: Force ratios F/F_b, for the intersection points shown in Figure 4.8 for the numerical models that their first mode's energy is matched with the first mode of the experiment.

H(mm)	Width(mm)	1.5	2	2.5	3	3.5
0.4	F/F_b	0.9249	0.9350	0.9470	0.9614	0.9791
0.5	F/F_b	0.7949	0.8029	0.8108	0.8215	0.8353
0.73	F/F_b	0.6318	0.6318	0.6347	0.6407	0.6496

As illustrated in Figure 4.9, the energy contained in the first mode for the purposely matched mode 1 disturbances are within a fraction of a percentage difference of the experiment ($\sim 0.1\%$ difference). Therefore the points appear overlapped and difficult to distinguish on the figure. However, a discrepancy remains in the energy contained in the second and third modes comparing to the experimental results. Consider the case having a width of 1.5 mm. For this case the simulated disturbance is comprised of nearly only a first and third mode ($\beta_{\Delta z}$ and $\beta_{\Delta z/3}$). A key observation from Figure 4.9 is that as the width is further increased the contributions of the modes 2 and 3 behave in an opposite sense. The relative energy of mode 2 increases while that of mode 3 decreases. Moreover, the height of the body force region as previously shown, mostly affects the required force for constant energy modes.

The second mode in the experiment has nearly 11% higher energy compared to the third mode and it is evident from Figure 4.9, in which the dashed blue line is placed above the dashed red line. For the cases with force region spanwise width of 3 and 3.5 mm the second mode is more than the third mode the same as the experiment. Hence, the body forces with widths more than 3 mm all appear to be possible choices for later studies. However, in here it is tried to choose a model that has a better match in the second mode with the experiment. Thus, the numerical model would have two modes matched with the experiment. The models with width of 3.5 mm ($n = 14$), have closer second mode energy to the experiment model.
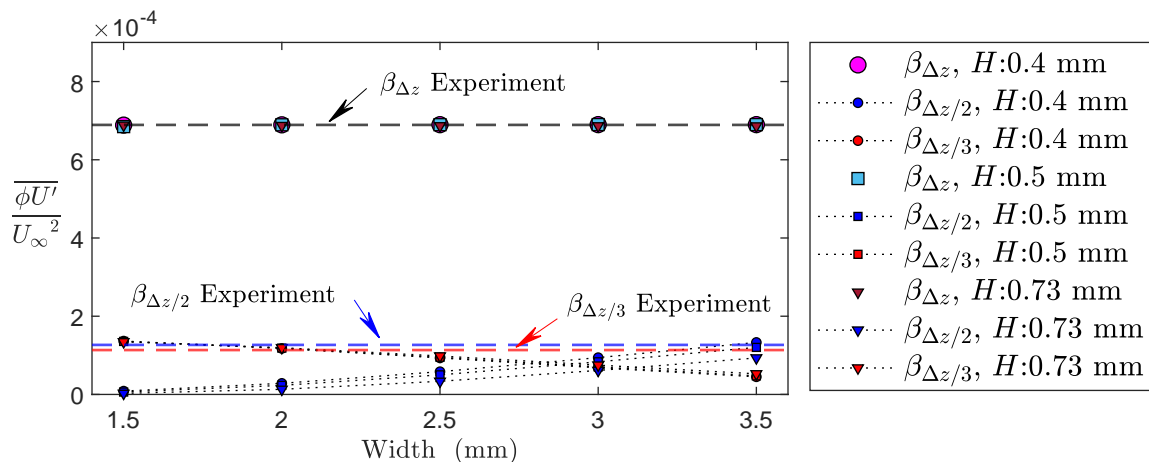
Figure 4.9: First three fundamental modes' energy for numerical models and experiment. The first modes are matched with the experiment and thus the points overlap for the various values of width and height for mode 1 (denoted by $\beta_{\Delta z}$).

The difference of the second mode for the case with $H = 0.4$ mm is $+5\%$, implying that the numerical model has more energy for $\beta_{\Delta z/2}$ wavenumber than the experiment. However, for the $H = 0.5$ mm is -5%; hence, it has less energy content. The difference between the second modes of the model with the $H = 0.73$ mm and the second mode of the experiment, is 26%.

Among all of the available options the model with $H = 0.4$ mm and width of 3.5 mm ($n = 14$) is selected. Figure 4.10a represents the disturbance velocity contour plots of the experiment and its first three fundamental modes, Figure 4.10b, for the final selected model's disturbance. As shown, the high-speed streaks are centered at $z/\Delta z = \pm 0.5$, and low-speed streaks are at $z/\Delta z = \pm 1$ and 0 in the numerical model, which is the same as the experiment. The high-speed streaks are doubled-peak in the simulation due to the same reason that explained for the experiment. Looking at the modal decomposition results of the disturbance for the first three wavenumbers, $\Delta z, \Delta z/2$, and $\Delta z/3$ demonstrates that the numerical model, in all of these modes, as that of the corresponding experiment.

The subtraction of the disturbance velocity calculated using the simulation (Figure 4.10b) from the corresponding experimental result (Figure 4.10a) is shown in Figure 4.10c. The mode 1 of the difference is nearly zero, which is a result of the near match that was purposely made
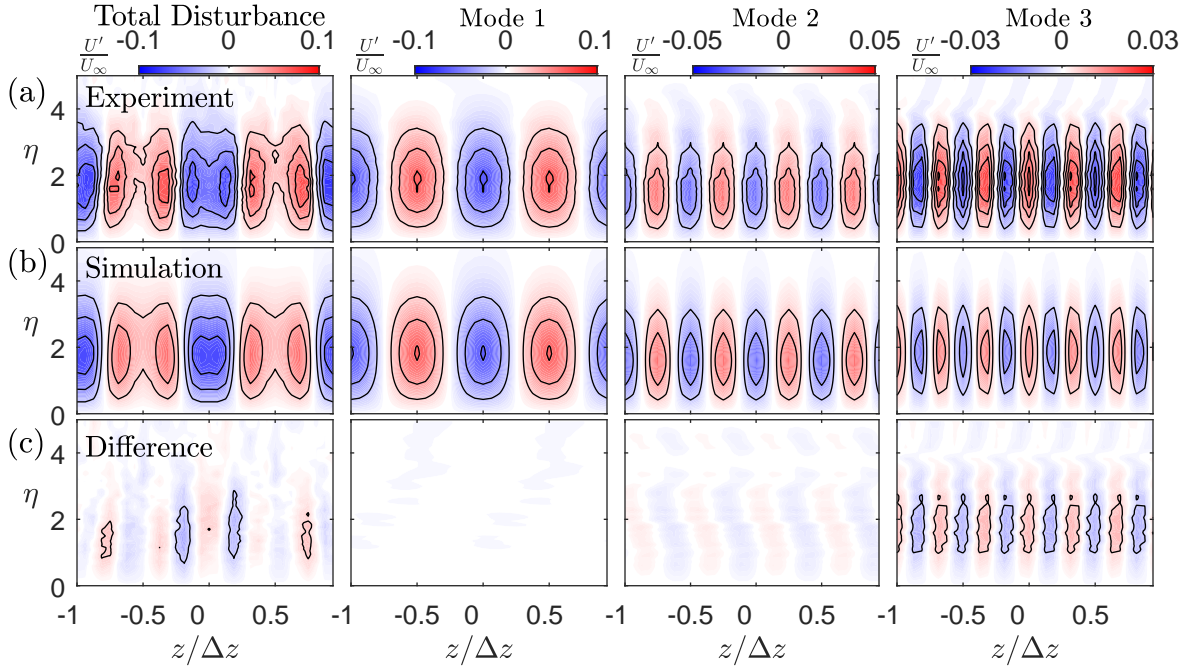
Figure 4.10: Contour plots of the disturbance velocity and the corresponding first three wavenumbers for (a) experiment (b) final selected numerical model with $H = 0.4$ mm, width of 3.5 mm ($n = 14$) and body force magnitude of $0.9791F_b$ (c) disturbance velocity of the experimental result with the corresponding simulation data subtracted.

as previously discussed in this Section. some minor difference owing to a slight mismatch in the energy at the mode 2, as was also described earlier in this section, to be within 5%. The difference between the third more is greater as anticipated from the comparison of the spectra from Figure 4.11. Despite all of these these differences the total energy difference between the simulate and experiment is within 8%.

4.4 Concluding Remarks

A parametric study on the magnitude of the simulated spanwise body force and spatial distribution including the width and height of the simplified body force model was performed. The most influential parameter on the ratio of the second and third harmonics of the disturbance velocity is the width of the body force region. Increasing the width causes an
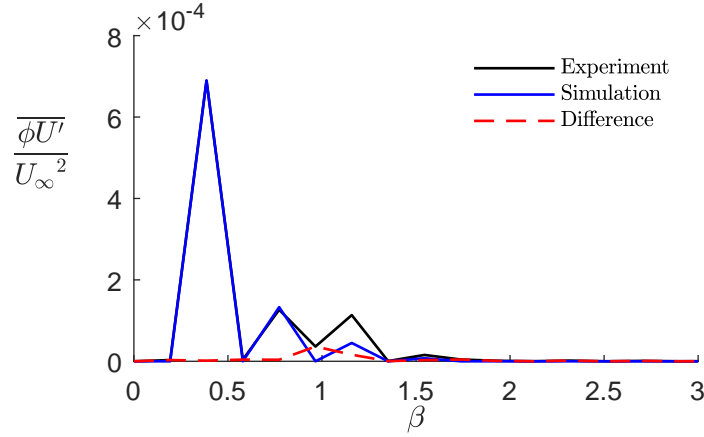
Figure 4.11: Spanwise averaged power spectrum of the disturbances. Black line is for the experiment and the blue line is for the simulation. Dashed red line representing the difference of power spectrum of the disturbance velocity of the experimental result with the corresponding simulation data subtracted.

increase in the second mode and decrease in the third mode, while it has a very small effect on the first mode. Increasing the body force magnitude creates more energetic disturbances. However, the ratio of the first and third modes decreases and the second mode increases strongly.

Increasing the thickness or height of the region of the simulated body force led to an increase in the total disturbance energy (see Figure 4.7), which was consistent with the results of the study by Font *et al.* [73] in which it was found that the net body force applied to the surrounding air will be reduced by reducing the height of the body force region. The parameters for the body force distribution and magnitude are selected based on the difference between the simulations and corresponding experiment (explained in Section 4.3). Although there was few options with the body force width of 3 and 3.5 mm it was decided to pursue the study with the case that has a width of 3.5 mm ($n = 14$) in the span, height of $H = 0.4$ mm, and force ratio $F/F_b = 0.9791$. For this case the resulting total disturbance energy over the height of the boundary layer at $x = 490$ mm was within 8 % of that of the experiment. The energy of mode 1 and 2 were nearly matched (within 0.1% and 5%, respectively), while a greater difference in mode 3 was observed.

Chapter 5

Blasius Boundary Layer Dynamic Response

5.1 Overview

In this chapter the temporal response of the laminar boundary layer to the modeled plasma actuator undergoing a step output from on to off is examined. The in depth understanding of the flow physics occurring is anticipated to support design improvements for closed-loop flow control systems targeting Bypass transition or sublayer streaks in the turbulent boundary layer. In this regard, the flow response to dynamic forcing is considered both in the near field of the actuators and in a region far downstream of the actuators. The far field (of the actuators) is defined as the region with $x > 400$ mm, where as the near-field (of the actuators) results are considered to be for the streamwise range of $290 < x < 350$ mm and only for the simulated flow. The far-field results are used to capture the non-minimum phase behavior of the flow observed experimentally by Hanson [14] and also by Jacobson *et al.* [37] with a different type of actuators. The major advantage of the use of this simulation is the access to the three components of flow velocity not available in the experimental dataset and also the corresponding shear stress. It is shown that the spanwise and wall-normal velocity are useful for describing the cause of the non-minimum phase behavior.

5.2   Far-Field Flow

5.2.1   Experiment

The streamwise velocity components were measured over seven planes in downstream of the actuators in the experiment (Figure 3.1). They were located from 400 mm to 700 mm evenly with the spacing of 50 mm. The third plane was just located at 490 mm to prevent blockage for the shear stress sensors at 500 mm. The operating voltage and frequency during the unsteady actuation were 5 kv and 1.5 kHz, respectively. This voltage is very close to the model that the simulation is matched with and was 4.96 kv. However, it will be shown that despite the slight difference in the voltages for the experimental models, the resulting disturbance in the transient simulation will have less amplitude than the transient experimental disturbance. Available transient experimental streamwise velocity component dataset is phase averaged over 25 complete cycles. Each cycle has 0.1 seconds of actuation and 0.9 seconds resting with the temporal resolution of 0.0005 seconds. This actuation parameter choice is sufficient to reach an approximately steady-state at the downstream planes considered before the deactivation of the actuators.

It was found that in the phase locked data at $x = 490$ mm that there existed a period of fluctuation with the actuator output that could be detected in the disturbance velocity output. While minor, the latter downstream plate at $x = 550$ mm (220 mm from the trailing edge of the actuators) was ultimately chosen for detailed consideration. The unfiltered disturbance velocity and the first three fundamental wavenumbers' transient evolution at the $\eta = 0.85$, and spanwise location of $z/\Delta z = 0$ are shown in Figure 5.1. In this figure, five instances are selected and labeled as (a) to (e). All the points are located on the blue line that represents the first mode's evolution in time. As illustrated in this figure, the initial response at $x = 550$ mm, occurs nearly after a time lag of 0.075 seconds. The reason stems from the distance between the region of the DBDs and the measurement plane. Consequently, the closer the plane, the faster the disturbances reach there. Another parameter that can affect the time
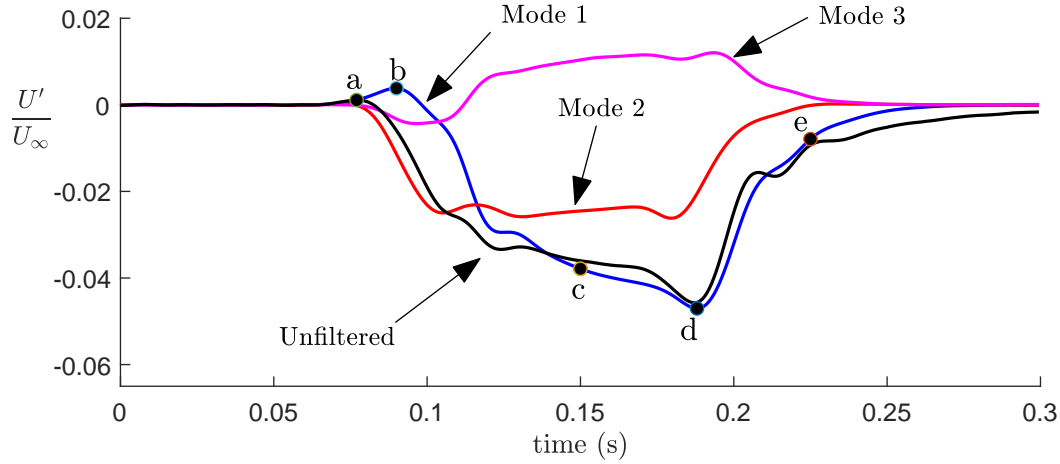
Figure 5.1: Experimental disturbance velocity variation and the first three fundamental modes at $x = 550$ mm, $\eta = 0.85$ and $z/\Delta z = 0$ for a 0.1 seconds of the DBD actuation that starts from t $= 0$ (s).

lag for the first downstream responses is the free-stream velocity. Higher free-stream velocity leads the created vortices over the actuators to travel faster.

At instant (a), which is at t $= 0.0775$ s, unfiltered disturbance and the first two harmonics show the presence of high-speed streaks ($U'/U_\infty > 0$). Also third mode at this moment is a low-speed streak. While as discussed in Chapter 4, during the steady actuation, a low-speed streak happens at this location, and the first and second modes are in the same phase with the unfiltered disturbance. In addition, the third mode has the opposite phase and is a high-speed streak. By a further increase in time; and moving to instant (b), t $= 0.905$ s, when the first mode has amplified and reached to its peak, third mode has also amplified. The second mode initially shows phase change and becomes in phase with its steady condition's phase, afterward starts amplifying. Before reaching instant (c), which is at t $= 0.15$ s, the third mode at t $= 0.097$ s, starts decreasing and finally at t $= 0.1125$ s, becomes in phase with its steady condition. The first mode, however, grows after point (b). The first mode continues the growth to reach the point (d) when it reaches its maximum magnitude. The two other modes have more gradual variation before their peaks and the final decay. At instant (e), t $= 0.225$ s, the disturbance is convected to downstream of the measurement

plane, hence all modes are vanishing and becoming zero.

Figure 5.2 depicts the spatial picture of the disturbance velocity and the fundamental wavenumbers corresponding to the five instances, shown in Figure 5.1. As it is evident in Figure 5.2a, at the first time instant, the disturbance is not yet developed to create double-peaked regions of disturbances; and only a weak disturbance appears in the measurement window. The entered disturbance looks stronger at the upper part of the boundary layer ($\eta > 2$). At the later time, instant (b), the disturbance shows that it has moved toward the
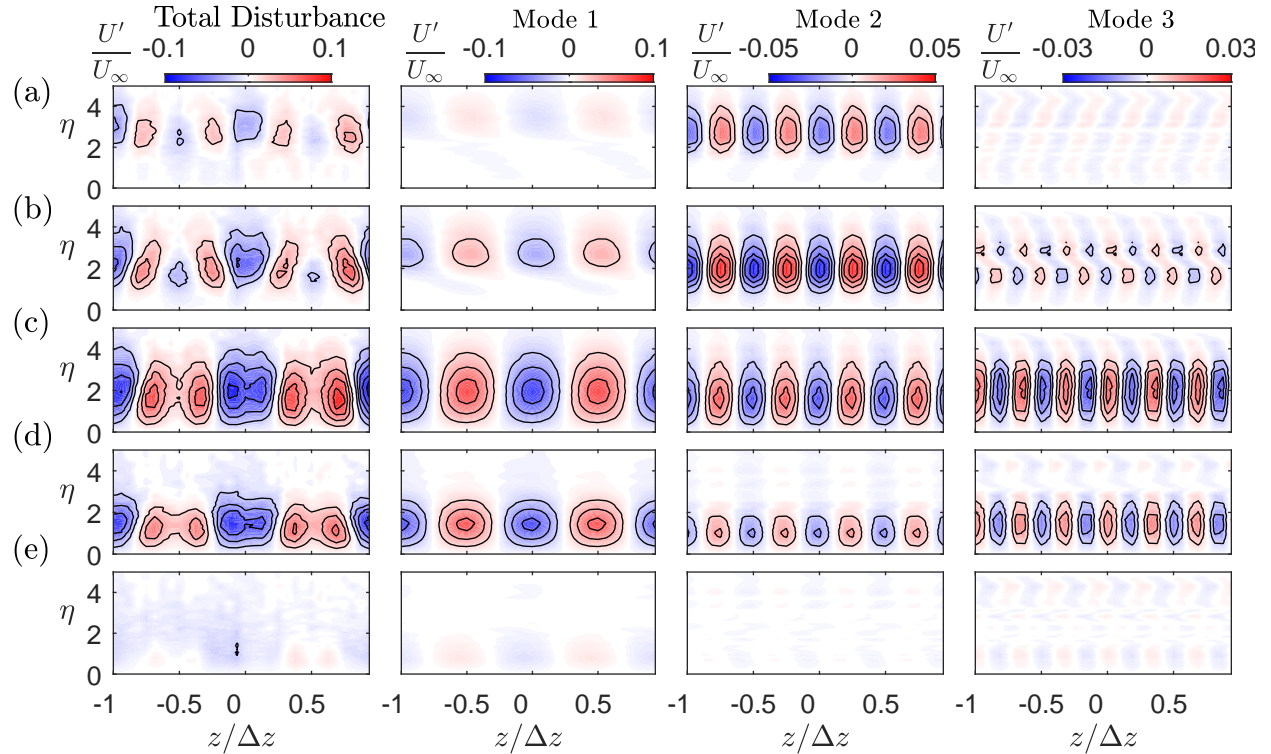
Figure 5.2: Contour plots of the disturbance transient evolution corresponding to the characteristic instances (a) to (e) shown in Figure 5.1. a) t = 0.0775 s, b) t = 0.905 s, c) t = 0.15 s, d) t = 0.188 s, e) t = 0.225 s.

wall compared to the previous time instant. At this moment, the third mode shows a better picture of the opposite phase this mode compared to the steady conditions. For instance, by moving from the wall $\eta = 0$ to the edge of the boundary layer $\eta = 5$, at $z/\Delta z = 0$, near the wall $\eta < 2$ this mode shows a low-speed streak while at $\eta > 2$ an opposite phase disturbance

is apparent. Moreover, at this instant, the second mode is the dominant mode, according to the contour levels and the contour lines that are set to be 5 lines from 0 to the maximum of the contour maps. The total disturbance structure also shows a spanwise distribution of high and low-speed streaks like the second mode.

In Figure 5.2c, which is at instant (c), disturbance has become double-peaked, similar to the steady actuation. At this moment, the first mode is the dominant wavenumber, also third mode shows a significant amplification compared to the previous instant. Figure 5.2d demonstrates that as time increases, the strong region of the disturbance velocity has moved closer to the wall; simultaneously, it has became less significant. The decay in the disturbance is mainly because vortices are convected to the downstream. Ultimately, at instant (e), Figure 5.2e, the disturbance is almost dissolved, and only a negligible disturbance is visible over the height of the boundary layer at the measurement plane.

5.2.2   Simulation

The tuned body force model, that is matched with a steady experimental model, is turned on for a duration of 0.1 s, the same as the transient experimental model. The results of the simulated flow are compared with the experiment at a similar downstream location x = 550 mm. Figure 5.3 shows the variation of the non-dimensionalized disturbance velocity (U'/U_∞) for the simulated flow at $x = 550$ mm, $\eta = 0.85$ and $z/\Delta z = 0$. The overall behavior of the unfiltered disturbance velocity and the first three fundamental wavenumbers at the same spatial location with the experiment, looks similar to the transient evolution of the disturbance velocity in the experimental model, discussed in Section 5.2.1. However, by comparing both transient models, figures 5.3 and 5.1, a clear lower amplitude for the simulation is evident. The reason essentially stems from the differences, although very minute, between the operating conditions in the steady experiment model that the body force is matched with and the experiment model used for the transient actuation.

The transient simulated model has a very weak third mode at all instances as shown in Figure 5.3. The low amplitude third mode was predictable from the steady results (see
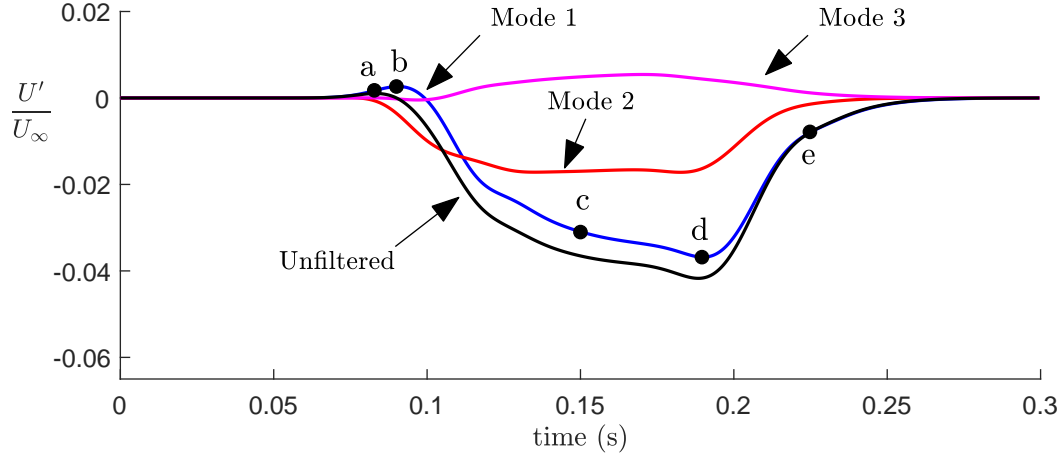
Figure 5.3: Simulation disturbance velocity variation and the first three fundamental modes at $x = 550$ mm, $\eta = 0.85$ and $z/\Delta z = 0$ for a 0.1 seconds of the DBD actuation that starts from t = 0 (s).

Figure 4.11. Instances (a) and (b) are at t = 0.0836 and 0.0908 s, respectively, and represent the moments when the unfiltered and the first mode reach their peaks with the opposite phase of the steady condition. Instant (c) is at t = 0.15 s, and instant (d) is at t = 0.1904 s. Instances (a), (b) and (d) that are characteristic moments when the unfiltered and first mode reach their extremum amplitude, have a subtle difference for the experiment and the simulation. This implies that the vortices have identical convective velocity in both flows. Hence, as mentioned earlier, the free-stream velocity and the distance of the measurement plane from the trailing edge of actuators are two critical parameters for the far-field response to the generated vortices.

The transient spatial evolution of the disturbance within the boundary layer corresponding to each characteristic instant shown in Figure 5.3 is demonstrated in Figure 5.4. Similar to the experiment at the instant (a) disturbance is emerged from the higher region of the boundary layer while it is very weak. In Figure 5.4a, in the unfiltered spatial disturbance velocity, the low-speed streaks centered at $z/\Delta z = \pm 0.5$ and in between the high-speed regions is clearly pictured. At the first shown instant, the disturbance velocity has not yet completely developed and the double-peaked regions are not yet formed.
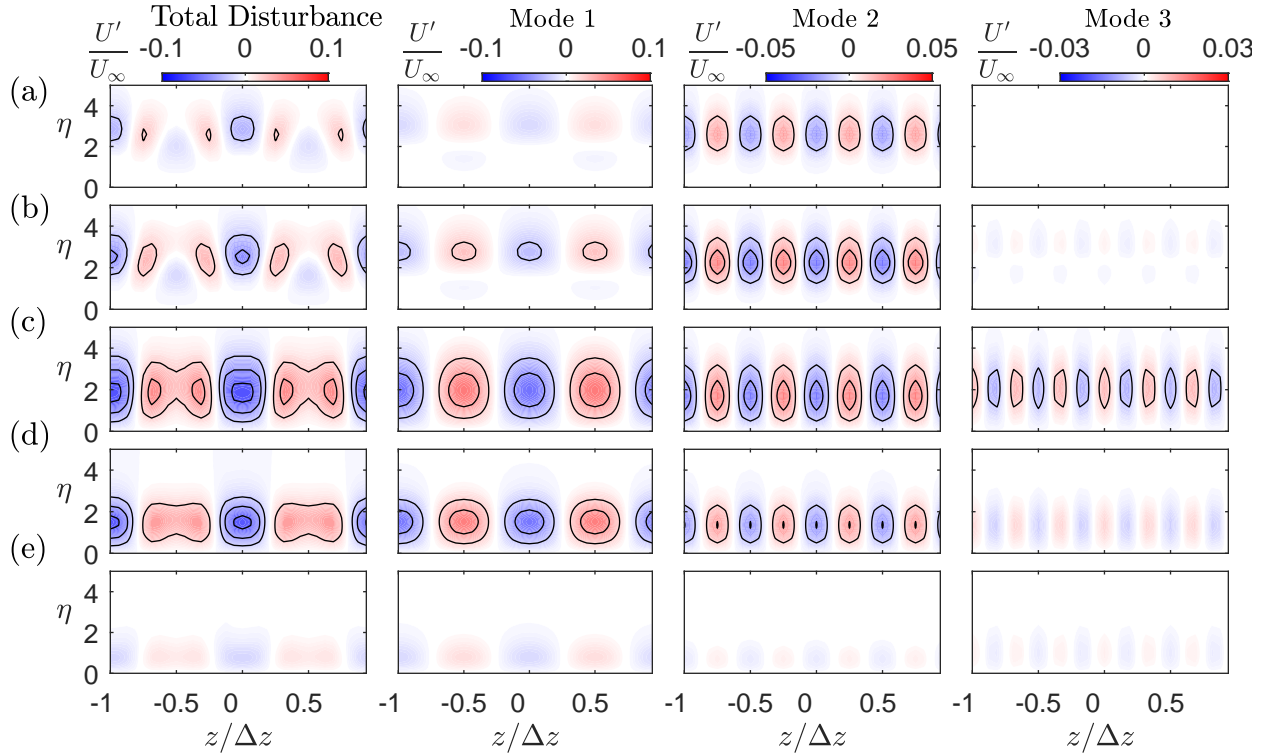
Figure 5.4: Contour plots of the transient disturbance evolution at $x = 550$ mm corresponding to the characteristic instances (a) to (e) shown in Figure 5.3. a) t = 0.0836 s, b) t = 0.908 s, c) t = 0.15 s, d) t = 0.1904 s, e) t = 0.225 s.

Following the development of the high-speed disturbance velocities, shows how they have grown and coalesced from the top to create the doubled-peak regions, as demonstrated in Figure 5.4b, and Figure 5.4c. Simultaneously, the stronger part of the disturbance has moved down to fill the near-wall regions, and the opposite phase disturbance starts to disappear. At instant (c), the disturbance is comparable with the steady situation (see Figure 4.10b). At point (d), The center of the unfiltered disturbance and decomposed modes get very close to the wall. Ultimately, at point (e), the disturbance is almost convected to the downstream, and the disturbance velocities are mostly disappeared from the measurement window.

As discussed in Section 2.2 the generated vortices form the spanwise low and high speed velocity regions via *lift-up* mechanism. Therefore, to find out the transient disturbance evolution, the transient vorticity maps are studied and compared with the steady model. The

steady vorticity map at the same downstream location in the transient model $x = 550$ mm is depicted in Figure 5.5. The streamwise vorticity can be expressed as Equation 5.1 in which where the V and W are the wall-normal and spanwise velocity components, respectively:

$$\Omega_x = \frac{\partial W}{\partial y} - \frac{\partial V}{\partial z}, \tag{5.1}$$

In Figure 5.5 at $z/\Delta z = \pm 0.5$, the center of the body forces (imaginary upper electrodes), a wall-ward flow motion is visible according to the velocity vectors. The velocity vectors also show how the fluid motion has formed the vortices shown by colormaps. As illustrated in this figure, at the spanwise range of $z/\Delta z$ = -0.5 to 0, a counter-clockwise rotation shown by velocity vectors has caused negative vorticity. Moreover, another response with opposite rotational direction is generated beneath the primary vorticity at the same spanwise range and is shown by red contour maps. In this thesis, if any rotational direction referred to as either CCW or CW, it has the same direction as the ones shown and discussed in Figure 5.5.
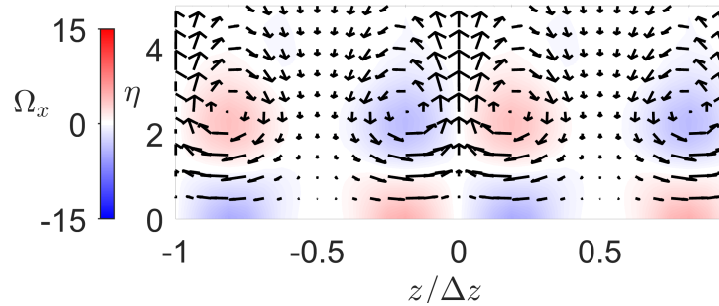
Figure 5.5: Contour plot of the vorticity at $x = 550$ mm, during the steady actuation.

The three dimensional streamwise vortex generated by DBDs in the steady model, is shown in Figure 5.6. The streamwise range pictured in this figure is from $x = 290$ mm to 700 mm. In this figure the side view ($y - x$ plane) is presented in the left plot and the right plot is the top view ($z - x$ plane). At the beginning of the streamwise domain, vortex is stronger which is evident from the higher iso-surface level in the core, and also since the shown iso-surface levels have filled a wider spanwise range. As the vortex has moved to the
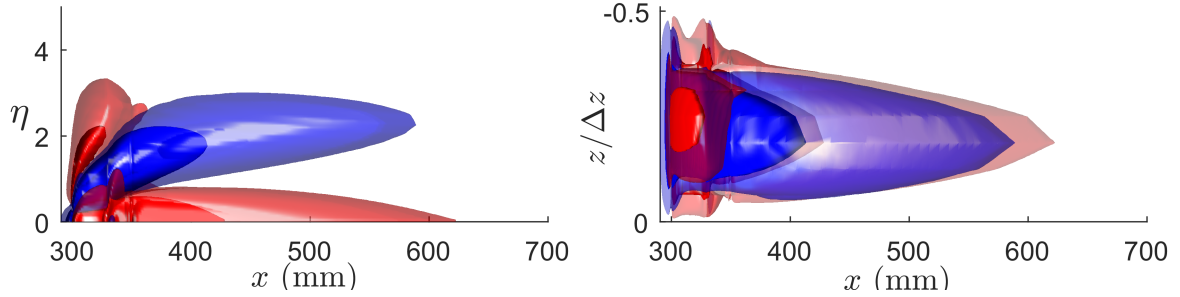
Figure 5.6: Streamwise vortex structure during steady actuation. Iso-surfaces levels correspond to $\Omega_x = \pm 15$ and ± 3 (1/s). The shown iso-surfaces are at the spanwise range of $-0.5 < z/\Delta z < 0$.

downstream its decayed, which observable from the disappeared higher level iso-surface and the shrank spatial size of the lower level iso-surface. Apparently, this vorticity structure leads to the steady disturbance at the downstream planes, an example at $x = 490$ mm is discussed thoroughly in the previous chapter. Hence, in the transient model, the appearance of the streaks with opposite signs of the ones expected from the steady actuation suggests the existence of secondary vortices. Thus, the vortices at the measurement plane are reproduced and presented in Figure 5.7. In this figure, the spatial development of the streamwise vortices at $x = 550$ mm is presented. Similar to the disturbance velocity, the decomposed modes of the streamwise vortcity have also been studied and shown in Figure 5.7. The blue regions represent the counterclockwise rotation (CCW), while the red regions have an opposite rotational direction (CW).

Figure 5.7, shows the transient evolution vorticity that has a complex pathway. To better explain, the vortex development in the spanwise range of $-0.5 < z/\Delta z < 0$ is chosen and discussed. The side regions, from $-1 < z/\Delta z < -0.5$ and $0 < z/\Delta z < 0.5$, have similar rotational characteristics only with opposite phase of the selected region for discussion. At instant (a), by moving from $\eta = 0$ to the edge of the boundary layer a blue contour map which represents a CCW rotation exist. On top of that region, a red contour map is shown, which implies a CW rotation. Ultimately, above both of these two vorticity maps another CW region is evident. As shown in Figure 5.5, at the selected spanwise range, near the wall a CW vorticity and above that to the edge of the boundary layer there is only a CCW
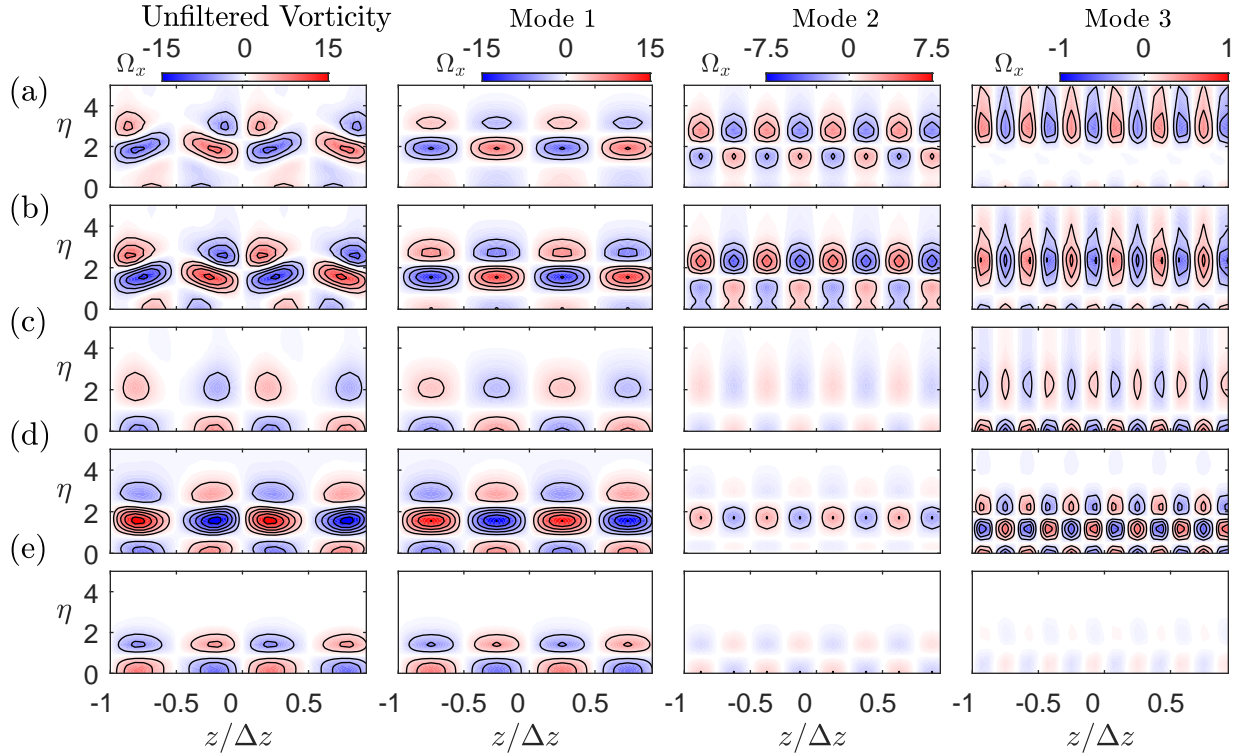
Figure 5.7: Contour plots of the vorticity transient evolution corresponding to the characteristic instances (a) to (e) shown in Figure 5.3. a) t = 0.0836 s, b) t = 0.908 s, c) t = 0.15 s, d) t = 0.1904 s, e) t = 0.225 s.

rotation. Therefore, at the first transient instant the arrangement of the vortices along the wall-normal direction does not follow the steady arrangement. With further increase in time at instant (b), all the vortices along the height of the boundary layer are amplified that can be seen by more intense colormaps at this instant. Moreover, comparing instant (b) with the previous instant suggests that the vortices have also had a wall-ward motion. The size of the near-wall vortex is reduced, while the highest vortex shows an increase in its size. At instant (c), an evident vortex phase change near the wall is visible. At this moment, along the boundary layer height, there are only two vortices. These vortices have led to the disturbance structure, Figure 5.4c, similar to its signature in the steady actuation with the doubled-peak regions of high and low-speed streaks. Moreover, the existing vortices in the study window show a significant decay comparing to the previous time instant. At instant

(d), the vortices are amplified, while at the higher regions of the boundary layer, a new CW vorticity has emerged. Ultimately, at instant (e), another vorticity phase change is evident. At this moment, the near-wall vorticity, that in the previous instant was CW, is replaced by a CCW vortex. Furthermore, at this instant, the vortices are again decayed compared to the previous instant.

To further explain and link the vorticity and resulted disturbance velocities, which clarifies the non-minimum phase behavior (e.g. Figure 5.3), the first modes in Figures 5.7, and 5.4 are considered. In this regard, the spanwise range of $-0.75 < z/\Delta z < -0.25$ is discussed. The disturbances at this range are centered at $z/\Delta z = -0.5$, while vortices are centered at $z/\Delta z$ =-0.75 and -0.25. Before reaching the steady type disturbance, instant (c), at the selected spanwise range the low-speed streak near the wall is caused by the presence of the secondary vorticity. At instant (a) when the vortices are weaker compared to the later instant the resulted disturbance velocity is also weaker. At instant (b), when the vortices are amplified the low-speed streaks at the selected range will be stronger. At instant (d), which is the other non-minimum phase point, the vortices as explained are amplified and also have moved toward the wall. Therefore, the near-wall disturbance, although has no phase change, is amplified before decaying.

Although the two-dimensional vorticity contour plots help clarify the non-minimum phase disturbance behavior, some physics remains vague. For instance, the wall-ward motion of the vorticity inside the boundary layer, the change in the rotation direction, and the appearance of the extra vorticities inside the boundary layer. More importantly, the reason for the amplifications of the vortices, obsereved at the downstream. The transient 3-dimensional vortex structure is reproduced to follow its development into the streamwise direction to find out the possible answer for all of these unclear phenomenons. In this regard, to extract the data from the numerical domain a few planes are defined in the far-field domain, and the streamwise vorticity component at each time step is saved over each plane. 85 planes are defined from x = 350.5 mm to 518.5 mm and 521 to 621 mm with 2 mm spacing. Also, 19 planes from 696 mm were defined with a spacing of 4 mm. To prevent any possible

interpolation error, all the planes are located so that they be at the streamwise location of the cell centers (see table 3.1).

The streamwise vortex structures, corresponding to the characteristic time instants (a) to (e), are shown from two different angles in Figure 5.8. To have a better insight to the travel of the vortex to the down stream two additional times are also represented in this figure and named as a_0 and b_2 that correspond to 0.05 and 0.125 s, respectively. The left side figures are the vortices from side view ($y - x$ plane), and the right side figures show the top view ($z - x$ plane). Since the vortex is symmetrical for each side of the actuator, only the vortex at the right side of the actuator, which is centered at $z/\Delta z = -0.5$, is represented. The vortex iso-surfaces in this figures have four levels ± 15 and ± 3 (1/s). The Blasius similarity length scale δ, is calculated separately at the streamwise location each plane.

As illustrated in the side view at instant a_0 in Figure 5.8a, the front of the plotted iso-surfaces which shows the vortex, which has a certain level of vorticity, is inclined with respect to the streamwise direction. In this view, it is apparent that the primary vortex at the studied spanwise range is the CCW one with blue color. Since this vortex is moved up, the shear layer response is also moved away from the wall. Hence, beneath the shear layer response, a secondary vortex is generated due to the presence of the wall, that is in phase with the primary vortex. The higher level of iso-surfaces shown by darker colors suggest that the vortex have not had had a significant decay. At the later moment, instant (a), the travel of the vortex to the downstream is evident, compared to the previous instant. Moreover, the stronger vortex closer to the actuators can be seen by the higher level of iso-surface. As the vortices have traveled to downstream ($x > 400$ mm) are decayed which stems from the viscous damping effect [54]. Inside the front inclined part, where at this moment shows less angle to the streamwise direction and can be found at $500 < x < 600$ mm , was stronger once created, because although it is decayed, there is still a small region of higher iso-surface level inside that.

Further increase in time, at instant (b), the secondary generated vortex shows a clear size reduction, comparing to the two previous instances. However, only considering the x
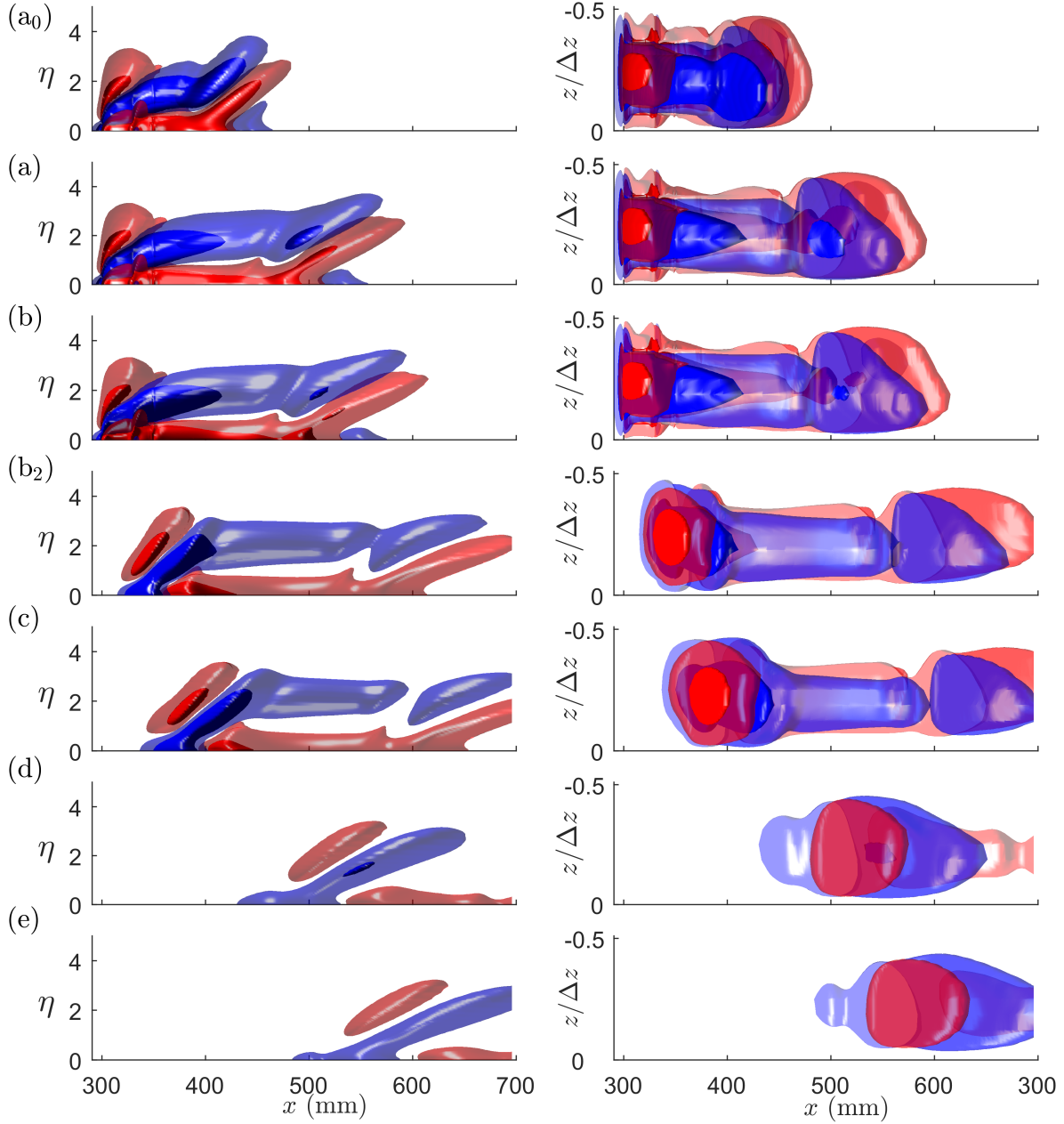
Figure 5.8: Side and top views of the four levels of streamwise vortex iso-surfaces, $\Omega_x = \pm 15$ and ± 3 (1/s), at each characteristic time instant shown in Figure 5.3. a_0) t = 0.05 s, a) t = 0.0836 s, b) t = 0.908 s, b2) t = 0.125 s, c) t = 0.15 s, d) t = 0.1904 s, e) t = 0.225 s.

= 550 mm, at instant (b) the secondary vortex near the wall, Figure 5.7 b side view, has taller region for the iso-surface compared to instant (a). Moreover, comparing the top views at $x = 550$ mm for instances (a) and (b) suggest that due to the wider region filled by a certain iso-surface level at instant (b) the vortex is stronger at that location at instant (b), which is the reason why the 2-dimensional contours in Figure 5.7b, also showed amplification compared to Figure 5.7a.

At instant (a) in the range of $x = 290$ to near 420 mm and at instant (b) to near $x=$ 470 mm the side view vortex structure looks identical to the steady actuation (see Figure 5.6). However, the top view at both instances, suggest that the vortex has not yet reached to its steady condition due to the differences between the steady model (Figure 5.6) and the transient ones (Figure 5.8a, b). At the later time, instant b_2, after the body forces are turned off, the selected iso-surfece levels are passed from the end of the streamiwse range, and also at $x = 550$ mm there is no more secondary vortex. Additionally, the top view at this moment shows how the downstream part of the vortices (e.g. $x > 450$ mm) are decayed, evident from the thinned iso-surfaces compared to the previous instances. At this time also, at the streamwise range of $x < 400$ mm, it can be observed that, similar to the initial inclined front part of the vortices, again the vortices are inclined with respecte to the streamwise direction. The top view at the mentioned streamwise range also suggests that the vortices are also amplified, since at this moment the filled spanwise range is widened too.

At instant (c), the picture of another secondary CW vortex over the primary vortex CCW, $300 < x < 450$ mm, is depicted. More importantly, at the start of the domain, $x < 400$ mm, the near-wall vortex is replaced with the primary CCW vortex. As time goes, the vortex moves more downstream it can be seen at instant (d), the new inclined part has reached $x = 550$ mm, while vortices are disappeared at $x < 400$ mm. Hence, as shown in Figure 5.7d, three vortices are at that downstream location. It is also evident at the CCW vortex core a higher level of isosurface, implying a stronger vortex. This clarifies the reason for the amplification of the vorticity contour plot at this moment illustrated in Figure 5.7d that also led to the second non-minimum phase behavior at this moment (see Figure 5.3). Ultimately,

at instant (e), the vortex is more damped, and only two vortices are visible $x = 550$mm. The vortex continues its travel to the end of the domain after this instant to completely get disappeared. An important conclusion from the comparison between the steady generated vortices in Figure 5.6, and vortices at different instances in Figure 5.8 is that, the transient model for in the case of 0.1 s actuation, never completely becomes the same as the steady model.

Vortices and the corresponding flow responses that appear as streaks will leave their signature on the wall shear stresses. Hence, spanwise and streamwise wall shear stresses are measured at the no-slip wall (see Figure 3.3). Figure 5.9a, shows the spanwise variation of the first mode of the both shear stress components at $x = 550$ mm and t = 0.13 s. In this figure, τ_z is multiplied by 5 to ease the comparison with τ_x by providing a better visualization. As
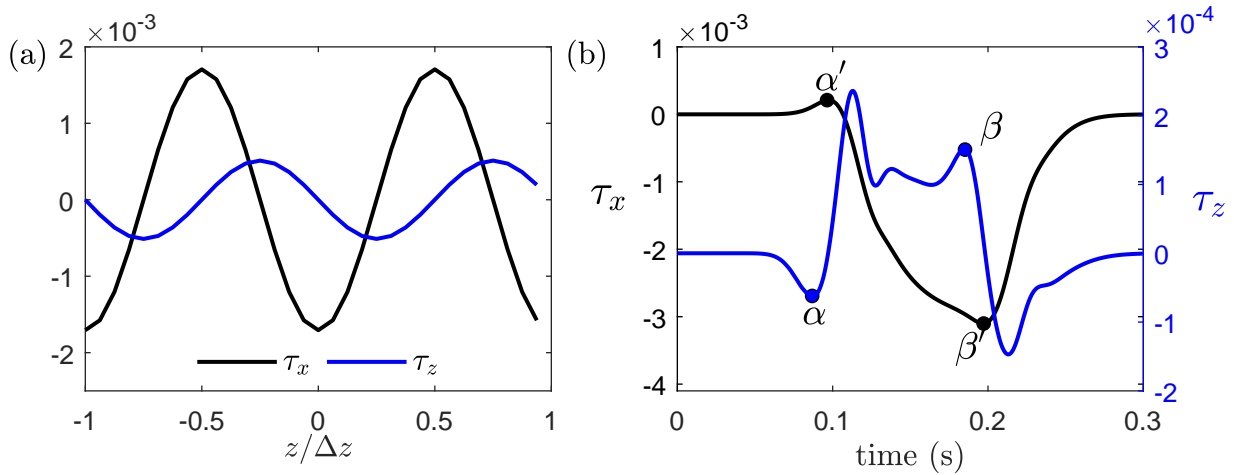
Figure 5.9: (a) Spanwise variation of the streamwise and spanwise shear stress components at $x = 550$ mm, and t = 0.13 s. τ_z is scaled by 5. (b) Transient variation of the streamwise shear stress component (τ_x) at $x = 550$ mm, $z/\Delta z$ = -0.5, and spanwise shear stress component (τ_z) at $x = 550$ mm, $z/\Delta z$ = -0.25.

depicted in this figure, the first mode of the spanwise shear stress τ_z peaks at ±0.75, and ±0.25 where is exactly under the center of the first mode of vortex as it is illustrated in the second column of Figure 5.7. On the other side, the first mode of τ_x peaks at ±0.5 and 0, where it is placed beneath the center of the high-speed and low-speed streaks respectively (see Figure 5.4, Mode 1). The spanwise variation of the first fundamental mode of τ_x and τ_z,

agree with the idealized model schematically shown by Naguib *et al.* [10].

Figure 5.9b, shows the transient variation of the τ_x at $z/\Delta z$ = -0.5, and τ_z at $z/\Delta z$ = -0.25. Following the variation of streamwise shear stress τ_x suggests, it is the streaks footprint on the wall, since it is comparable with the transient evolution of the disturbance velocity in Figure 5.3. On the other hand, the transient evolution of the spanwiswe shear stress τ_z is the immediate disturbance signature on the wall [10].
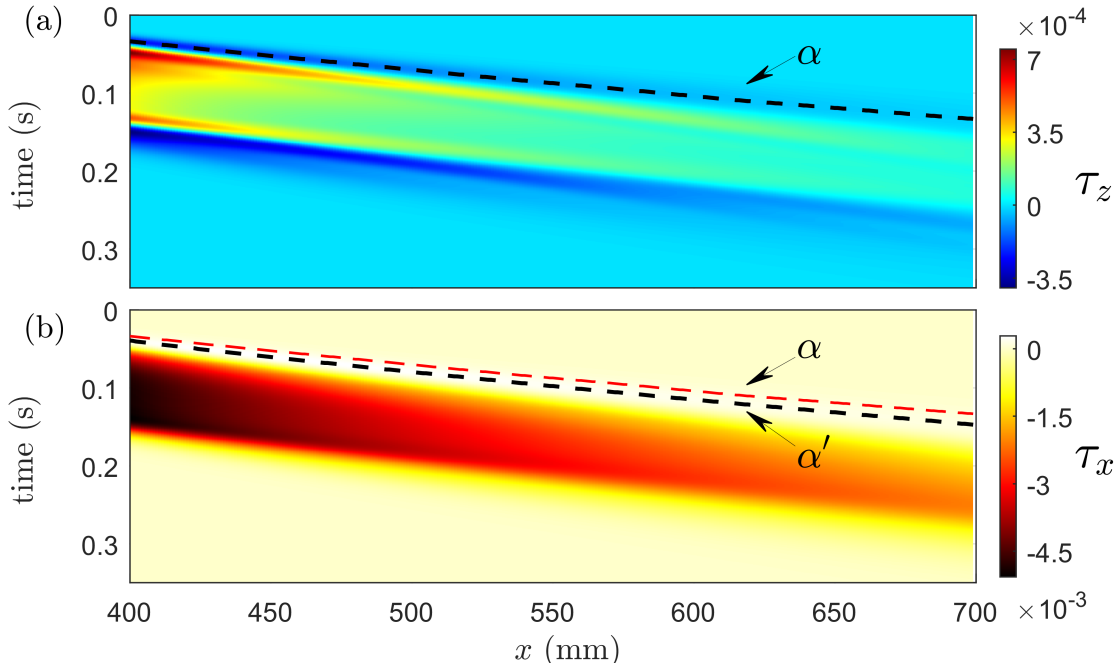
Figure 5.10: Transient variation of the first fundamental mode of the (a) spanwise shear stress component (τ_z) at $z/\Delta z$ = -0.25, (b) streamwise shear stress component (τ_x) at $z/\Delta z$ = -0.5 along the streamiwse range of $400 < x < 700$ mm.

Naguib *et al.* [10] showed that τ_x lags behind the disturbance while τ_z instantly responds to the changes of the disturbance and remain in phase with the disturbance. This also evident in Figure 5.9b. For a better explanation four characteristic instances are labeled as α, α', β, β', that are at t = 0.0872, 0.0976, 0.1856, and 0.1972 seconds respectively. At instant α, the spanwise shear stress component is an extremum point. This implies that the vortex that has led to this magnitude of τ_z has also an extremum strength at that time. Hence, an extermum U' which will cause a extremum τ_x is expected. However, the maximum

of the τ_x happens at a later time at α'. Similarly, a time lag is evident for β and β'. In Figure 5.9b, τ_z initially becomes negative and after instant α starts amplifying, moreover, after instant β it start decaying, however before becoming completely zero it becomes negative and peaks at t = 0.2136 s, later on start to become zero. Therefore, the phase inversion in the vortex observed in Figure 5.8, has left its affect on the spanwise wall shear stress, meaning that this shear stress component remains in phase with the disturbance. It can be concluded that for the purpose of flow control, spanwise shear stress component provides more advanced details of the disturbances with no time lag as also mentioned by Naguib *et al.* [10].

Figure 5.10 shows the transient evolution of the first fundamental wavenumber of τ_z at $z/\Delta z$ = -0.25, and τ_x at $z/\Delta z$ = -0.5 at multiple downstream locations. It can be seen that both τ_z and τ_x occur faster for the upstream locations, while they are also stronger. Two times phase change in the spanwise shear stress can be observed along the shown streamwise range. In Figure 5.10a, the dashed black line corresponds to point α for different downstream locations. This line is later shown with dashed red line in Figure 5.10b, to be compared with α' for $400 < x < 700$ mm. In Figure 5.10b, α line, shows faster response at all downstream locations while the corresponding streamwise shear stress, α', has always lagged behind.
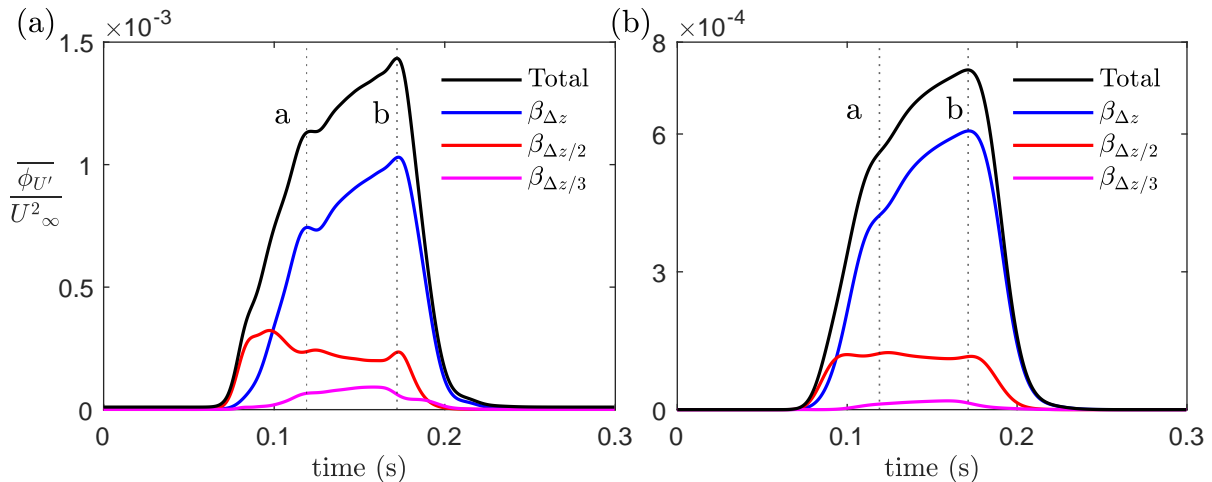
Figure 5.11: Transient total flow energy variation and the first three fundamental wavenumbers at $x = 550$ mm for (a) experiment, (b) simulation

The transient variation of the flow energy for both the experiment and the simulation

at $x = 550$ mm is presented in Figure 5.11a and Figure 5.11b, respectively. The simulation has less amplitude, which stems from the differences between the experimental model that body forces are matched with, and the experimental model used for the dynamic actuation. However, the transient flow energy growth shows similar trend for both models. The total energy for the experimental flow in Figure 5.11a, calculated over the first 8 fundamental wavenumbers (equation 4.3), has peaked twice at a = 0.119 s, and b = 0.172. The simulation at the same time of a = 0.119 s, shows less significant difference with the moments before and after. However, the obvious maximum peak that is illustrated by dashed lines at b = 0.171 s, is in a very noticeable agreement with the experiment's in terms of the moment it is happened. For both models the first mode contains most of the energy in most of the times. Unlike the first mode, the second wavenumber shows less variation and shows a gradual decay between nearly 0.1 < t < 0.2 s. The third mode, has very low amplitude for both models compared to the first two wavenumbers.

5.3   Near-Field Flow

The bulges, the inclined parts of vortices, are originated from the dynamic vortex formation above the actuators. Hence, the region close to the actuators that starts from 290.5 mm to 349.5 mm from the leading edge called Near-Field, is studied. Considering this region provides a more clear picture of the dynamic vortex formation by the DBD actuators when they are oriented into the streamwise direction and in a laminar boundary layer. Velocity and streamwise vorticity components are measured at each time step on 60 planes along the mentioned streamwise range with the spacing of 1 mm, that are all located at the center of the cells (see table 3.1).

Before the current study, most of the researches have focused on the vortex formation once the flow has become steady [49, 54]. Vortex formation in the steady case in quiescent air and zero pressure gradient boundary layers are discussed in Chapter 2. As discussed the wall-ward motion is caused by the entertainment of the fluid to satisfy the continuity of mass

and leads to a spanwise jet velocity. The spanwise jet velocity creates the primary vortex beside the actuator. The reorientation of the jet velocity as it decays in the span; and the reorientation of the replaced boundary layer spanwise vorticity will act as two other sources of vorticity on the main vorticity to create a streamwise vortex structure [54](see Figure 2.4).

The flow over the spanwise range of $-0.5 < z/\Delta z < 0$ will only be discussed. The vortex formation and its temporal evolution are demonstrated by using the streamwise vortex iso-surfaces and the streamlines. The dynamic vortex formation has two stages, the first one is when the body forces are turned on, and it is called ON-Cycle; the other one is when they are deactivated and is called as OFF-Cycle.

Considering that the bulges are initiated from the DBDs location, they may also leave their footprint on the total circulation. Hence, this parameter is calculated over the near-field region and is given by, $\Gamma = \int \Omega_x.dA$, where dA is calculated from $-0.5 < z/\Delta z < 0$, and from the $\eta = 0$ up to the edge of the Blasius boundary layer $\eta = 5$, that is calculated at streamwise location of the measurement planes separately. The boundary layer height at the tip of the actuators is 5 mm. As Figure 5.12 shows, the circulation is zero before time $= 0$ s. When the actuators are turned on, an abrupt increase in the circulation exactly above the actuators happens. Then the circulation increases up to the peak for each plane at different moments, which occurs later for further downstream locations. Before the flow becomes steady, overshoots in the circulation are visible along the near-field domain. Afterward, the circulation decreases and reaches a steady condition and will remain at this situation until the body forces are turned off. At this moment, the circulation decays suddenly. Circulation will not become zero sharply after deactivation, however, it happens faster for the upstream planes. As pointed by Jukes *et al.* [54], the increase after actuation implies that the circulation is mainly caused by the jet velocity and because of the actuators. Moreover, the decrease after the trailing edge of the plasma actuators (body force region) is due to the viscous stresses near the wall [54].

It can be seen in Figure 5.12 by moving from $x = 300$ mm to $x = 330$ mm the magnitude of circulation increases, which suggests the body force accumulation effect on the generated
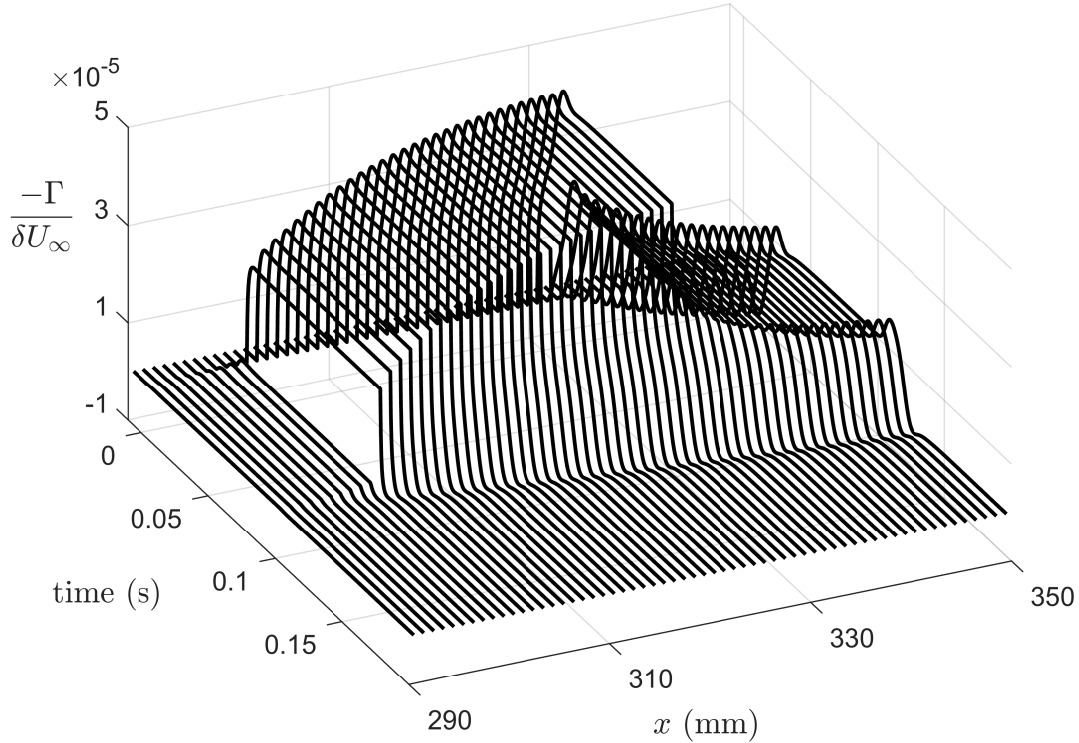
Figure 5.12: Transient vortex circulation $(-\Gamma/\delta U_\infty)$ development over the near-field region.

vortices. Fitting a line over the transient circulation plot, Figure 5.12, at t = 0.05 s, and $300 < x < 330$ mm, implies that when the circulation has become steady can be scaled by $\Gamma \sim x^{0.19}$. This rate of increase in the experiments by Jukes *et al.* [54] was found to be $\Gamma \sim x^{1/3}$. The difference may stem from the differences between the current simulated model and the experimental model was studied by Jukes *et al.* [54]. Few characteristic instances are chosen in Figure 5.12. At these moments the vortices in the near-field region are illustrated spatially by using iso-surfaces in Figures 5.13 and 5.16.

5.3.1 ON-Cycle

Figure 5.11 illustrates the vortex structure by using the iso-surfaces with the levels of $\Omega_x = \pm 65$ and ± 3 (1/s). The blue iso-surfaces show a CCW rotation, and the red ones are CW. The streamlines are plotted that are initiated from $x = 290.5$ mm, $z/\Delta z = -0.275$. In
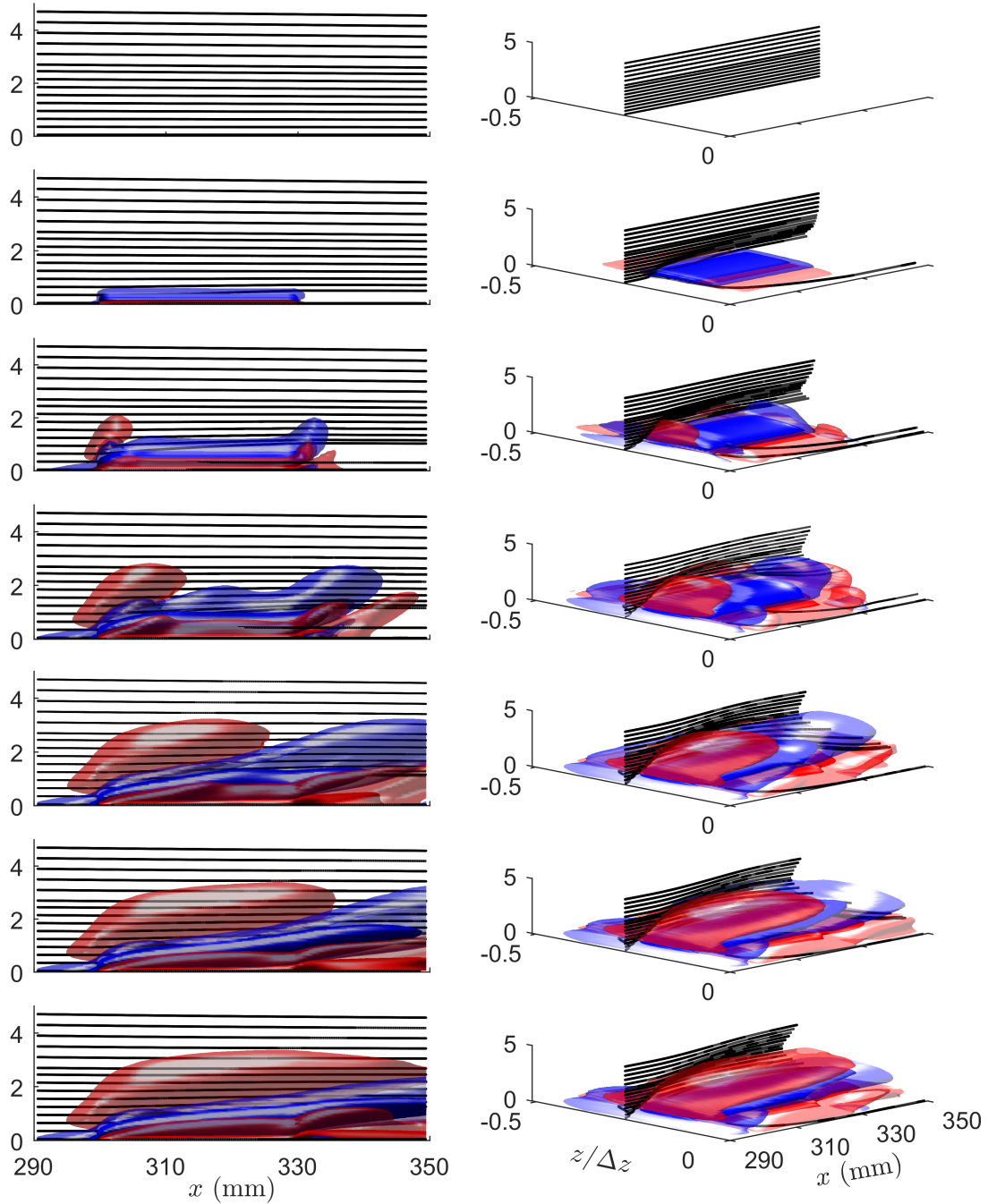
Figure 5.13: Streamwise vorticity isosurfaces. $\Omega_x = \pm 65$ and ± 3 (1/s). Streamlines with increments of 0.3η for $0.05 < \eta < 2.5$ and increments of 0.4η for $2.5 < \eta < 5$ initiating from x = 290.5 mm, $z/\Delta z = -0.275$. a) t = -0.0004 s, b) t = 0.0004 s, c) t = 0.0032 s, d) t = 0.0076 s, e) t = 0.0136 s, f) t = 0.02 s, g) t = 0.05 s.

the normal direction, for $0.05 < \eta < 2.5$, they have 0.3 η increments, and from there to the edge of the boundary layer, the increment is 0.4 η. The edge of the actuator is at $z/\Delta z = -0.3$. The spanwise range of body force region is $-0.3 < z/\Delta z < -0.125$.

The first moment shown in Figure 5.13a is a time step before the body forces are activated. At this moment, there is no vortex and the streamlines show a parallel arrangement. One time step after actuation, Figure 5.13b, a very weak vortex is formed over the wall, that is resulted from the spanwise velocity component [54]. The vortex at this moment has a uniform structure along the actuator. As demonstrated in the isometric view at this moment, streamlines show deviation from their previous arrangement, since flow is affected by the jet velocity. At t = 0.0032 s, Figure 5.13c, the vortex shows the formation of two significant bulges at the tip and trailing edges of the actuator. The streamlines in the side view at this moment show that the flow after hitting the jet velocity is blocked and moved away from the wall.

At instant (d), t= 0.0076 s, the circulation $(-\Gamma/\delta U_\infty)$ reaches the peak value for the front edge of the actuators. The vortex iso-surfaces at this moment Figure 5.13d, also show a clear amplification at that location since the shown blue iso-surface is at a higher η and have spatially become bigger which means that the vortex core has become stronger and the lower levels are pushed to the surroundings. At the same time, the bulge at downstream is also amplified that is also can be found due to the iso-surface spatial size. At point (e), t = 0.0136 s, the circulation reaches the maximum at $x = 315$ mm, or the middle of the body force region. At this moment the iso-surfaces show a significant increase in theri size. Therefore, the vortices are more amplified. In addition, the blue iso-surface for 340 mm $< x$, has reached higher regions of boundary layer. For t = 0.02 s, or instant (f) the circulation peaks at the trailing edge of the body force's region. The vortices at this point show that the have slightly moved down, which is more obvious for the blue iso-surface. Comparing the last time instant (g), t = 0.15 s, and instant (f) shows that the iso-surfaces are wider at instant f at $x = 330$ mm. At instant (g) circulation has stationary condition along the near-field region. At this moment the vortices are completely developed.

Following the CW vortex above the primary CCW vortex, from instant (b) to (g) shows that this vortex does not exist with the assigned iso-surface levels. However from instant (c) is observable and at the initial moments this vortex is more intense near the front edge of the actuator and as time has passed this vortex has amplified and developed to the streamwise direction. The instances when the circulation has peaked at different streamwise locations are the moments when top CW vortex has formed there. It can be said the initial bulge which is formed from the front and trailing edges of the body force regions is responsible for the later non-minimum phase behavior at the far-field region.

The spanwise velocity component at $x = 300.5$, 315.5, and 329.5 mm and the spanwise location of $z/\Delta z = -0.25$ is illustrated in Figure 5.14. In this figure the time instances are the same as the instances in Figure 5.13 (b) to (e). At t = 0.0004 s, the spanwise velocity profile is identical for different downstream locations, and as discussed the vortex also is uniform along the body force region at this moment (Figure 5.13b). The increase in the induced jet
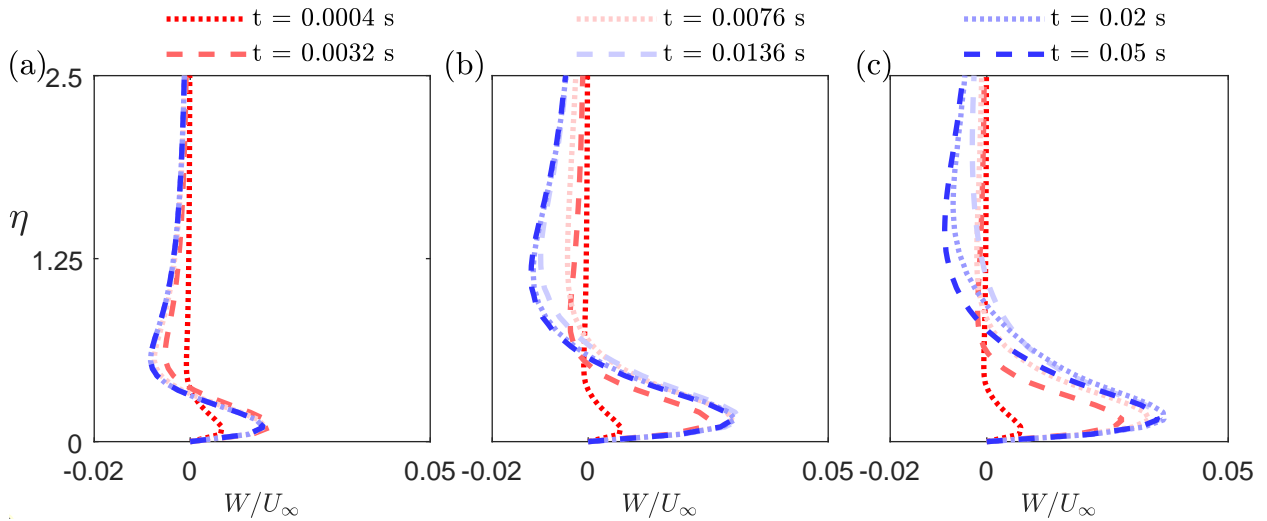
Figure 5.14: Spanwise velocity profile at $z/\Delta z = -0.275$ at (a) $x = 300.5$ mm, (b) $x = 315.5$, (c) $x = 329.5$ mm.

velocity for next times is evident for the three downstream locations. Moreover, it is evident that, except the first instant, at later times the jet velocity has increased for the further downstream locations, which stems from the body force accumulation. Following the temporal

evolution of the spanwise velocity profile suggests that the profile has peaked its maximum at t = 0.0032, 0.0136, and 0.02 s at x = 300.5, 315.5, and 329.5 mm respectively. The peaks has occurred later for the downstream locations, due to the arrival of the affected flow at the upstream. It can be seen that during the steady condition, t = 0.05 s, the maximum velocity is slightly reduced for all streamwise locations. The steady profile look similar to the profile that was experimentally measured by Balcon *et al.* [50], in a quiescent condition. Unlike the maximum point that is reduced once the flow has become steady the minimum velocity, $(W/U_\infty < 0)$, that has led to the formation of the upper CW rotation shown in Figure 5.13, has become more negative during the steady condition for all streamwise locations.
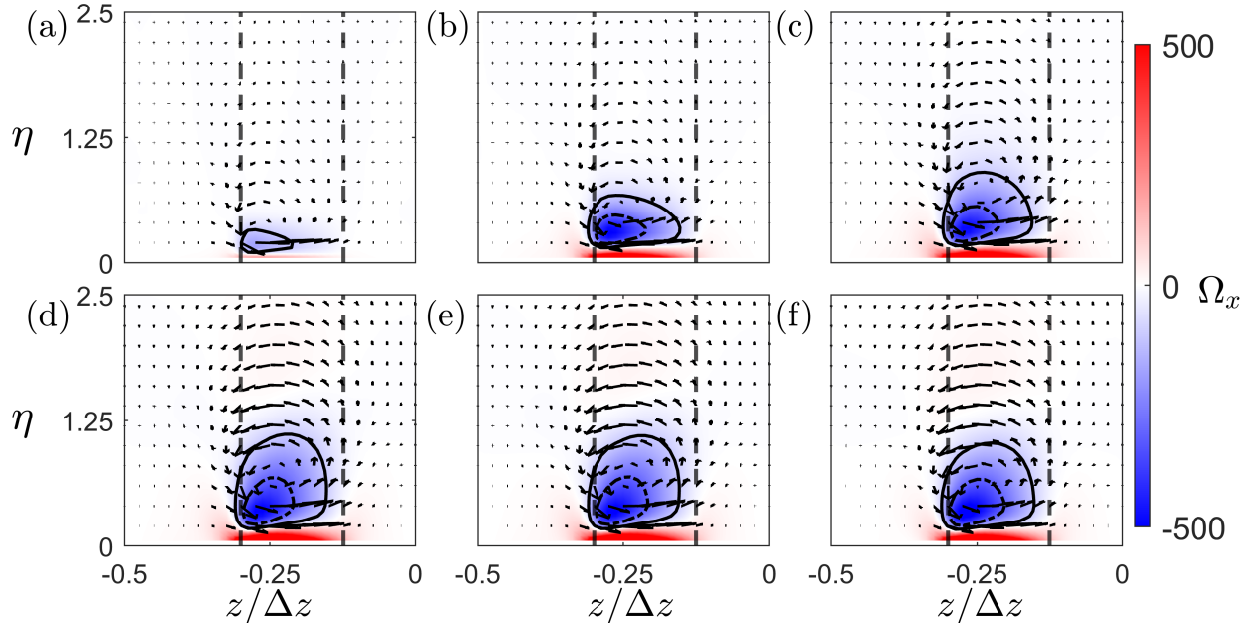
Figure 5.15: Contours of the vorticity and the velocity vectors at x = 315.5 mm, and $-0.5 < z/\Delta z < 0$. Dashed black lines represent the spanwise region of applied body force and are at $z/\Delta z$ = -0.3 and -0.125. The black solid contour line level is -100 (1/s) and the black dashed-dotted contour line level is -300 (1/s). (a) t = 0.0004 s, (b) t = 0.0032 s, (c) t = 0.0076 s, (d) t = 0.0136 s, (e) t = 0.0144 s, and (f) t = 0.05 s.

Figure 5.15 shows the transient vorticity evolution at the middle of the body force region x = 315.5 mm beside the edge of the imaginary upper electrode at $z/\Delta z$ = -0.3 in six instances. At instant (a), t = 0.0004 s, the flow entrainment caused by the body force is shown by the

velocity vectors. At this moment a weak CCW vorticity is observable beside the edge of the body force region. At later instances from (b) to (d), the vorticity has enhanced and shows a growing pattern which can be observed by following the contour level of -100 (1/s). At t = 0.0136 s, when at this location the circulation has peaked (see Figure 5.12), the contour line with the level of -100 (1/s) has reached higher wall-normal location. During the next instances the CCW vorticity shows a wall-ward motion and ultimately a steady condition is shown in Figure 5.15f, t = 0.05 s. From instant (d) to (f) the counter rotating vorticty above the primary vorticity can be observed by a very light red contourmap. According to Figure 5.14, and Figure 5.15, it can be said that the counter rotating vorticity develops as the primary vorticty gets stronger and it becomes more dominant when the flow reaches its steady rotational condition beside the actuator.

According to the observations in transient vortex formation (Figure 5.13) and the transient velocity profile evolution (Figure 5.14), the following story is suggested as the reason for the bulge formation during the on-cycle. As pointed in Chapter 2, when the plasma actuators are activated, a starting vortex forms beside the edge of the actuator before the jet profile becomes stationary. This starting vortex for a single plasma actuator can move away from the wall and edge of the actuator [52]. However, for a spanwise array of plasma actuators placed in a boundary layer, since they produce pairs of impinging wall-jets, the starting vortex can not move completely to the span; therefore, it moves upward while is pushed by the upcoming flow to the downstream. Hence, the starting vortex will be added to the primary vorticity which leads to the peaks in circulation, and its upward motion causes the bulge formation.

5.3.2   OFF-Cycle

During the off-cycle, the flow is studied at 7 instances. The first time is at the moment when the actuators are turned off, t = 0.1004 s. The vortices structure at this time looks very similar to the steady situation during the on-cycle. However, the maximum of jet velocity profiles, Figure 5.17, at $x = 300.5, 315.5$ and 329.5 mm are decreased by 43%, 16%, and 13 %
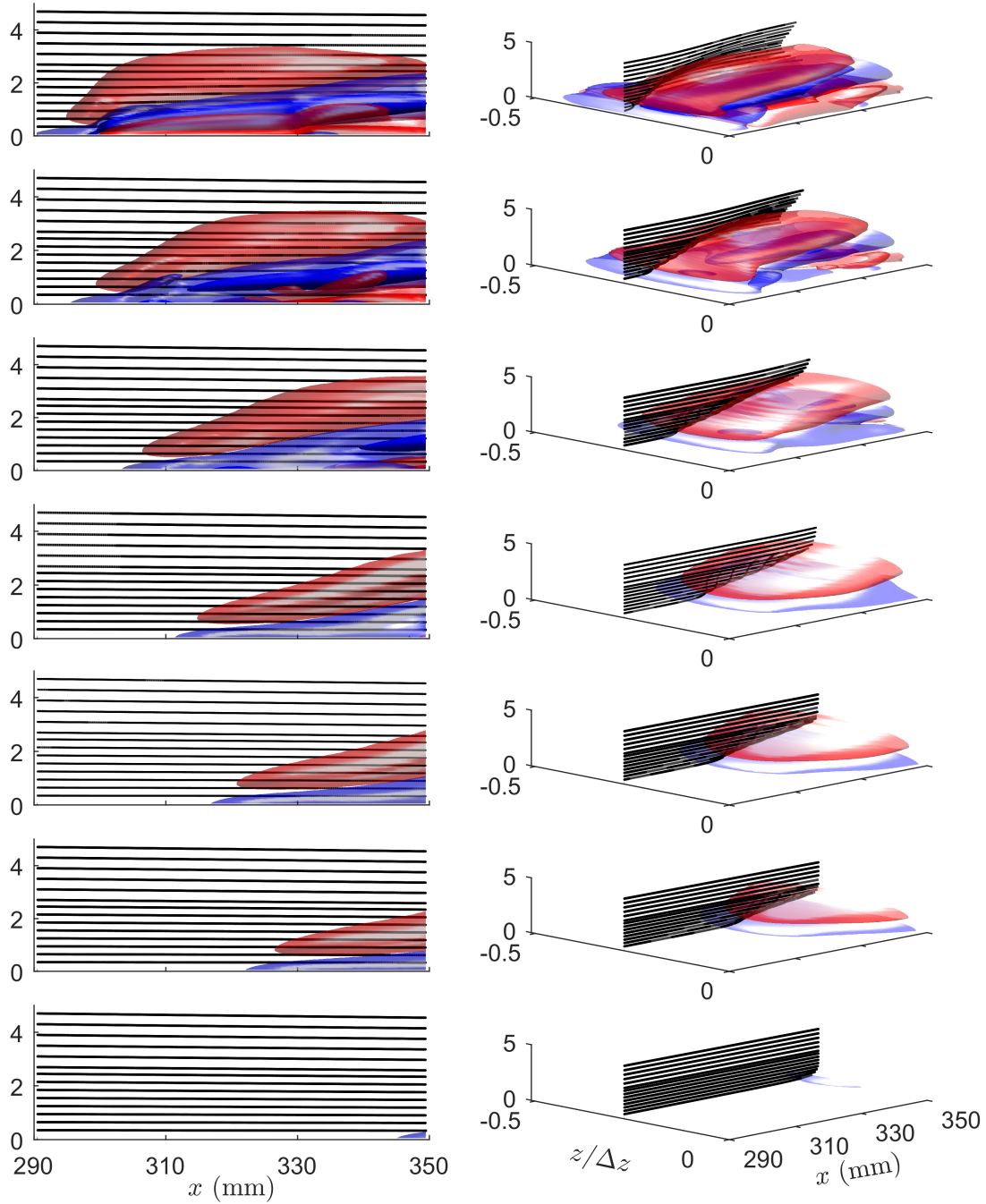
Figure 5.16: Streamwise vorticity isosurfaces. $\Omega_x = \pm 65$ and ± 3 (1/s). Streamlines with increments of 0.3η for $0.05 < \eta < 2.5$ and increments of 0.4η for $2.5 < \eta < 5$ initiating from x = 290.5 mm, $z/\Delta z = -0.275$. a) t = 0.1004 s, b) t = 0.1064 s, c) t = 0.1152 s, d) t = 0.1216 s, e) t = 0.126 s, f) t = 0.13 s, g) t = 0.146 s

respectively, comparing to their steady condition, or a time step before. This sudden decrease stems from the reason that during the off-cycle there is no more energy output by the body forces, which also caused the sharp reduction of the circulation in Figure 5.12.

At instant (b), t = 0.1064 s, when at $x = 300.5$ mm, the circulation reaches its minimum (Figure 5.12) and a phase inversion in the vortex is visible. The upper vortex replaces the CW vortex close to the wall. This causes the CCW rotation to become the dominant circulation within the flow, leaving a weak effect above that appears as the CW vortex. The jet velocity profile, Figure 5.17, at this moment at $x = 300.5$ mm shows that the spanwise velocity component has almost become zero. The phase inversion is also observable at $x = 315.5$ mm, however at $x = 329.5$ mm is not still occurred.
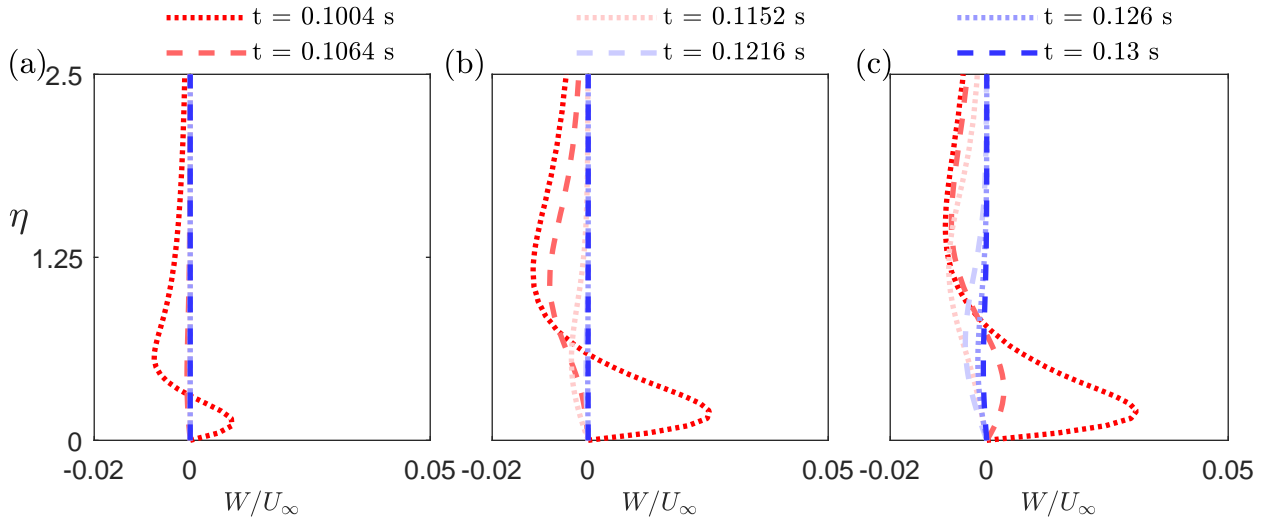
Figure 5.17: Spanwise velocity profile at $z/\Delta z = -0.275$ at (a) $x = 300.5$ mm, (b) $x = 315.5$, (c) $x = 329.5$ mm

At instant (c), t = 0.1152 s, when at $x = 315.5$ mm the circulation becomes minimum, the replacement of the vortices has become more apparent. At instant (d), t=0.1216 s, at $x = 330$ mm, the minimum circulation occurs, according to Figure 5.12. Unlike the front planes, as shown in Figure 5.12, the circulation downstream becomes zero more gradually because of the arrival of the upstream vortices. Their motion is apparent in all time instances during the off-cycle. In the last three instances t =0.126, 0.13 and 0.146 seconds this is demonstrated.

In all of the off-cycle instances as shown in the side view the streamlines have moved to their wall-normal positions before the actuation. Suggesting that the main blockage is caused by the strong induced jet due to the output of the body forces. Moreover, in the isometric view they show their reorientation in the span due to the presence of the remaining vortices inside the flow.

The transient vorticity evolution during the off-cycle at $x = 315.5$ mm beside the edge of the imaginary upper electrode and in the spanwise range of $-0.5 < z/\Delta z < 0$, is depicted in Figure 5.18. To better picture the vorticity map at instances d to f the colorbar level is set at the range of ± 200 (1/s). Therefore, at instances a and b the colormap looks more saturated. The contourline with the level of -100 (1/s) has become smaller from instant (a) to (d), suggesting the reduction in the vorticity magnitude. Besides, the near wall vorticity shows a significant attenuation. Which as discussed earlier in this Section, is due to the
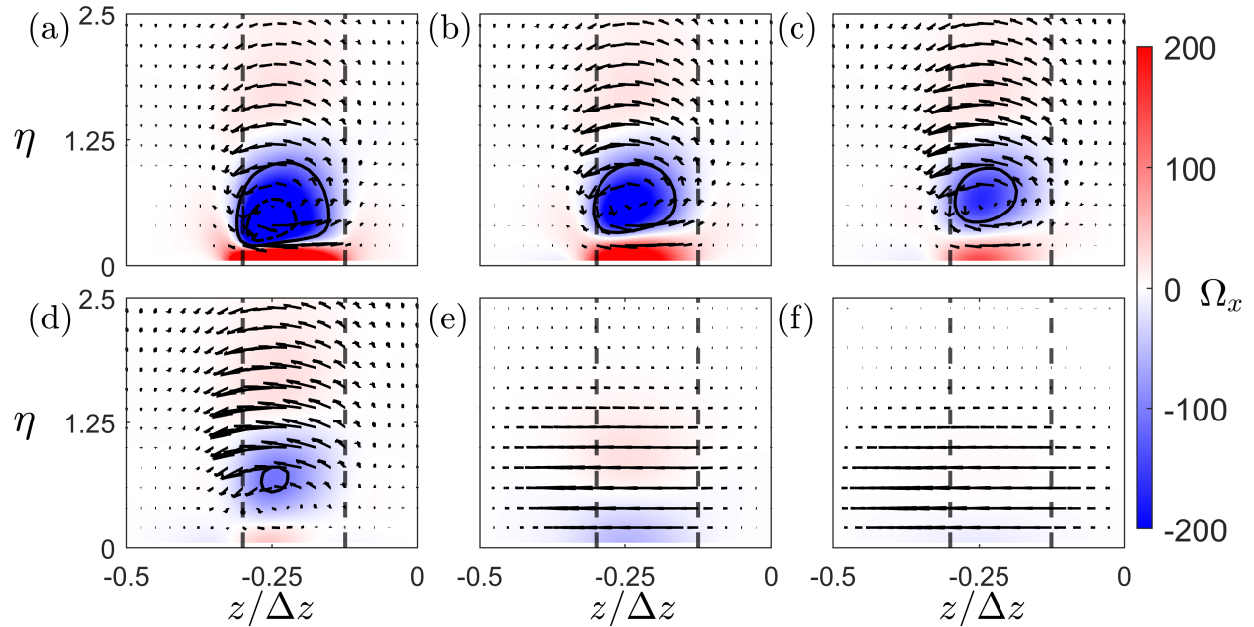
Figure 5.18: Contours of the vorticity and the velocity vectors at $x = 315.5$ mm, and $-0.5 < z/\Delta z < 0$. Dashed black lines represent the spanwise region of applied body force and are at $z/\Delta z = $ -0.3 and -0.125. The black solid contour line level is -100 (1/s) and the black dashed-dotted contour line level is -300 (1/s). (a) t = 0.1004 s, (b) t = 0.1020 s, (c) t = 0.1036 s, (d) t = 0.1060 s, (e) t = 0.1152 s, and (f) t = 0.1204 s.

deactivation of the body force. During the on-cycle the vorticity showed a bottom to top development. However, as shown in Figure 5.18 a to f, a top to bottom evolution is followed during the off-cycle. At instant (e), the near-wall CW rotation is completely replaced by the CCW rotation and the circulation has reached to its minimum magnitude at this moment. At instant (f), t = 0.1204 s, it can be seen that the vorticity is almost completely convected to the down stream.

The following story is suggested as the reason for occurring second non-minimum phase response, point d in Figure 5.3, which was found to be led by a vortex amplification showed in Figure 5.7d and Figure 5.8c, d. As pointed by Jukes [54], and observed by the streamlines in Figure 5.13, the spanwise jet velocity during the On-Cycle causes flow blockage, and consequently an upward motion for the upcoming flow. When the body forces are deactivated, the spanwise jet velocity reduces significantly and the flow blockage will be reduced drastically. Hence, the regions with higher streamiwse velocities move back closer to the wall. As a result the remained vortices at the near-field region move faster to downstream and will have higher magnitude at downstream locations compared to the steady condition.

5.4   Concluding Remarks

To determine the non-minimum phase behavior of the flow at the Far-Field region, observed in the experiment [14] that limits the controller efficiency during the active actuation, a transient model is simulated numerically. The same flow response is observed in the simulated flow. The numerical model has provided a more advanced picture for the reason of this flow response by accessing the full field data that is hard to be measured experimentally.

It is found that the distance from the trailing edge of the actuators and the flow properties, including the free stream velocity and boundary layer height, are of the key parameters that define the disturbance evolution in time, measured at a particular height of the boundary layer. Studying the transient flow energy variation with analogous routes for both experiments and simulation suggests the same with very similar times when the peaks happened (see

Figure 5.11).

Studying the spatial vorticity structure, provided by the simulation at the measurement plane, showed that the opposite phase of the disturbance near the wall($\eta = 0.85$) at points a and b in Figure 5.3 happen because of the secondary vortices generated beneath the primary vortices because of the presence of the wall. Furthermore, the other non-minimum phase response at point c is because of the vorticity amplification at that moment.

By extracting the full field vorticity data, a three-dimensional vortex structure could be reproduced, which provided a more profound insight for the top to the bottom motion of the vorticity in Figure 5.7a-e. It is shown that the reason arises because of the inclined front head of the vortex. Hence, the vortex enters from the top to the study window and leads to a secondary vortex formation. Its rotational phase is similar to the primary vortex indicated with blue isosurfaces in all figures representing the vortex. Besides, as mentioned, the amplification of the disturbance at instant c in Figure 5.3 happens due to the arrival of the bulge from the upstream to there. Since the only sources of vorticity inside the flow are the reorientation of spanwise jet, boundary layer spanwise vorticity, and the twisted flow entrained above the actuators, the origin of this vortex formation goes back to the upstream where the actuators are placed.

When the actuators are activated, at the initial instances, a uniform vortex is created beside the actuators that its spanwise development is limited by the vortices that are created by other body force regions in the span, while Jukes [54] showed that in the case where only one actuator is inside the flow the vortex moves to the span with the yaw angle of 10°. Two bulges will appear in the front and back of the actuators; they grow and finally coalesce. The bulgy part of the vortex then travels to downstream by the upcoming flow. Ultimately, during the off-cycle, another bulge appears that causes the amplification of disturbance later, as it moves further downstream. The formation of bulges during the On-Cycle seems to occur because of the starting vortex. During the Off-Cycle the vortex is not amplified by the body forces anymore and the reason for the presence of stronger vortices at the downstream stem from the faster motion of strong vortices formed befire deactivating the actuators over

the body forces region to the downstream with higher convective velocity. In another word, when the flow blockage is removed, the wall-normal positions of the vortices, place in higher regions of boundary layer with less viscous dissipation and higher streamwise velocity.

Chapter 6

Conclusions

Plasma actuators have shown promising results for active flow control applications. For example, a spanwise array of plasma actuators oriented in the streamwise direction were used by Hanson *et al.* [12, 13, 14] for controlling the transient growth of streaks that lead to sub-critical transition to turbulence that is known as Bypass Transition. The current study is motivated by the non-minimum phase flow response observed experimentally during the dynamic response of the boundary layer when a step input was applied to the plasma actuators. It is known that a non-minimum phase response, when used as input for a feedback control system, limits the bandwidth of the control system. In the related experiments the results of the flow were limited to only the streamwise velocity component. In the related experiments the results of the flow were limited to only the streamwise velocity component. The numerical simulations in this thesis provide all flow velocity components and permitted a more detailed study of the underlying flow response.

Initially, a laminar boundary layer that agrees with the Blasius solution is established. Afterward, to simulate the effect of plasma actuators, a body force is applied to the established flow using a momentum source. The applied body force has a linear distribution in wall-normal and spanwise directions similar to the model proposed by Shyy *et al.* [79]. A parametric study on the geometrical distribution of the applied body force and its magnitude is conducted first to consider the effect of each of these parameters and ultimately match the generated

disturbances in the numerical model with a particular experimental model downstream of the actuators.

For a constant width and height, increase in the body force magnitude leads to increase in the total flow energy. However, the study on the energy ratio of the first three fundamental wavenumbers showed that the energy ratio of the first and third modes would decrease. In contrast, the second mode will have more contribution to the total energy ratio. The total energy ratio of the first three modes decreases by increasing the magnitude of the body forces, implying the amplification of the higher harmonics. The spatial properties of the body force region, including its height and width, showed that the energy ratio of different modes mostly depends on the width of the body force region, while the total flow energy has very negligible variation with the variation of the width of the body force region. On the other hand, the total flow energy significantly varies with the variations of the height of the body force region.

The width of the body force region studied from 1.5 mm (or $n = 6$ cells) in the span and increased incrementally up to 3.5 mm ($n = 14$ cells). For the case with 1.5 mm spanwise extent of the body force region, the generated disturbance has a very weak second mode, while the third mode is the second dominant mode after the first fundamental mode. As the width increased, the second mode amplified, followed by a decrease in the third mode. Therefore, the disturbance velocity structure will vary with the variation of the width of the body fore region. For example, for a wider forcing region, the high-speed streaks centered at $z/\Delta z = \pm 0.5$ will be more double-peaked, while the low-speed streak will look more double-peaked by decreasing the width of the forcing region.

Moreover, it is found that the net body force applied to the flow depends on the height of the body force region. Applying the same amount of body force within a region with a greater height leads to a stronger disturbances and more flow energy. This stems from the more wall drag losses near the wall. For all the widths and heights, the body force magnitude is tuned to match the first fundamental mode of the simulated flow with first fundamental mode of the experiment. It is shown that the first mode can be easily matched. Among the available options with their matched first mode, the model which its second mode had a more

close match with the particular experimental model was chosen for studying the dynamic actuation.

The flow response to a step input with the duration of 0.1 s, the same as the corresponding experiment, was considered. The dynamic disturbance evolution showed the non-minimum phase behavior near the wall at $\eta = 0.85$ at two different times. While the first point is also out of phase with the disturbances expected from the steady actuation at the same location. The inversion in the disturbance velocity near the wall was observable in the spatial transient evolution of the disturbances. Access to the transient full field data in the numerical model enabled picturing the transient evolution of the vortices that lead to the spanwise regions of high and low speed streaks. It is found that the transient vortex formation over the body force region is responsible for the non-minimum phase behavior downstream. An amplified vortex will move away from the wall and cause a counter-rotating response near the wall that initially leads the out of phase streak. At the end of the actuation cycle, stronger vortices were observed that cause the second non-minimum phase response.

The study of the streamwise and spanwise wall shear stress showed that the spanwise wall shear stress will change instantaneously by the variation of the near-wall vorticity and is in phase with the near-wall vorticity in the streamwise direction. On the other hand, the streamwise wall shear stress, the signature of the streaks on the wall, has a time delay compared to the spanwise wall shear stress component. Therefore, this suggests that the spanwise wall shear stress may be used as input in a control system to reduce time lag.

References

[1] M. Molina et al. "What We Know–The realities, risks, and response to climate change". In: American Association for the Advancement of Science (AAAS). 2014.

[2] *Paris Agreement.* Apr. 2016. URL: https://en.wikipedia.org/wiki/Paris_Agreement.

[3] Environment Canada and Climate Change. *Government of Canada.* URL: https://www.canada.ca/en/environment-climate-change/services/environmental-indicators/progress-towards-canada-greenhouse-gas-emissions-reduction-target.html.

[4] J. Kim. "Physics and control of wall turbulence for drag reduction". In: *Philosophical Transactions of the Royal Society A: Mathematical, Physical and Engineering Sciences* 369.1940 (2011), pp. 1396–1411.

[5] *Canada's Action Plan to Reduce Greenhouse Gas Emissions from Aviation.* URL: https://tc.canada.ca/en/corporate-services/policies/canada-s-action-plan-reduce-greenhouse-gas-emissions-aviation-0#s1.

[6] S. L. Brunton and B. R. Noack. "Closed-loop turbulence control: progress and challenges". In: *Applied Mechanics Reviews* 67.5 (2015).

[7] R.D. Joslin. "Aircraft laminar flow control". In: *Annual Review of Fluid Mechanics* 30.1 (1998), pp. 1–29.

[8] P.K. Kundu, I.M. Cohen, and D.R. Dowling. *Fluid Mechanics.* Elsevier Science, 2015. ISBN: 9780124071513.

[9] M. Gad-el-Hak. *Flow Control: Passive, Active, and Reactive Flow Management.* Cambridge university press, 2007.

[10] A. M. Naguib, J. Morrison, and T. A. Zaki. "On the relationship between the wall-shear-stress and transient-growth disturbances in a laminar boundary layer". In: *Physics of Fluids* 22.5 (2010), p. 054103.

[11] Andersson, P. and Brandt, L. and Bottaro, A. and Henningson, D. S. "On the breakdown of boundary layer streaks". In: *Journal of Fluid Mechanics* 428 (2001), pp. 29–60.

[12] R. E. Hanson, K. M. Bade, B. A. Belson, P. Lavoie, A. M. Naguib, and C. W. Rowley. "Feedback control of slowly-varying transient growth by an array of plasma actuators". In: *Physics of Fluids* 26.2 (2014), p. 024102.

[13] R. E. Hanson, P. Lavoie, A. M. Naguib, and J. F. Morrison. "Transient growth instability cancelation by a plasma actuator array". In: *Experiments in fluids* 49.6 (2010), pp. 1339–1348.

[14] R. E. Hanson. "Control of transient growth induced boundary layer transition in a zero-pressgure gradient boundary layer using plasma actuators". PhD thesis. University of Toronto, 2013.

[15] W. S. Saric, H. L. Reed, and E. J. Kerschen. "Boundary-layer receptivity to freestream disturbances". In: *Annual Review of Fluid Mechanics* 34.1 (2002), pp. 291–319.

[16] P.J. Schmid and D.S. Henningson. *Stability and Transition in Shear Flows*. Applied Mathematical Sciences. Springer New York, 2000. ISBN: 9780387989853.

[17] T. Sayadi, C. W. Hamman, and P. Moin. "Direct numerical simulation of complete H-type and K-type transitions with implications for the dynamics of turbulent boundary layers". In: *Journal of Fluid Mechanics* 724 (2013), pp. 480–509.

[18] J. M. Kendall. "Studies on laminar boundary-layer receptivity to freestream turbulence near a leading edge". In: (1991).

[19] P. Klebanoff. "Effect of free-stream turbulence on a laminar boundary layer". In: *Bulletin of the American Physical Society*. Vol. 16. 11. 1971.

[20] T. A. Zaki. "From streaks to spots and on to turbulence: exploring the dynamics of boundary layer transition". In: *Flow, Turbulence and Combustion* 91.3 (2013), pp. 451–473.

[21] M. Landahl. "A note on an algebraic instability of inviscid parallel shear flows". In: *Journal of Fluid Mechanics* 98.2 (1980), pp. 243–251.

[22] J. Hunt and P. Durbin. "Perturbed vortical layers and shear sheltering". In: *Fluid Dynamics Research* 24.6 (1999), p. 375.

[23] E. Reshotko. "Transient growth: a factor in bypass transition". In: *Physics of Fluids* 13.5 (2001), pp. 1067–1075.

[24] P. Andersson, M. Berggren, and D. S. Henningson. "Optimal disturbances and bypass transition in boundary layers". In: *Physics of Fluids* 11.1 (1999), pp. 134–150.

[25] X. Mao, T. A. Zaki, S. J. Sherwin, and H. Blackburn. "Transition induced by linear and nonlinear perturbation growth in flow past a compressor blade". In: *Journal of Fluid Mechanics* 820 (2017), pp. 604–632.

[26] N. J. Vaughan and T. A. Zaki. "Stability of zero-pressure-gradient boundary layer distorted by unsteady Klebanoff streaks". In: *Journal of Fluid Mechanics* 681 (2011), pp. 116–153.

[27] H. Choi, P. Moin, and J. Kim. "Active turbulence control for drag reduction in wall-bounded flows". In: *Journal of Fluid Mechanics* 262 (1994), pp. 75–110.

[28] L. N. Cattafesta and M. Sheplak. "Actuators for active flow control". In: *Annual Review of Fluid Mechanics* 43 (2011), pp. 247–272.

[29]   R. Rathnasingham and K. S. Breuer. "Active control of turbulent boundary layers". In: *Journal of Fluid Mechanics* 495 (2003), pp. 209–233.

[30]   J. Park and H. Choi. "Effects of uniform blowing or suction from a spanwise slot on a turbulent boundary layer flow". In: *Physics of Fluids* 11.10 (1999), pp. 3095–3105.

[31]   A. K. M. F. Hussain and W. C. Reynolds. "The mechanics of an organized wave in turbulent shear flow". In: *Journal of Fluid Mechanics* 41.2 (1970), pp. 241–258.

[32]   K. S. Breuer, J. H. Haritonidis, and M. T. Landahl. "The control of transient disturbances in a flat plate boundary layer through active wall motion". In: *Physics of Fluids A: Fluid Dynamics* 1.3 (1989), pp. 574–582.

[33]   J. H. M. Fransson and P. H. Alfredsson. "On the disturbance growth in an asymptotic suction boundary layer". In: *Journal of Fluid Mechanics* 482 (2003), pp. 51–90.

[34]   F. Lundell, A. Monokrousos, and L. Brandt. "Feedback control of boundary layer bypass transition: experimental and numerical progress". In: *47th AIAA Aerospace Sciences Meeting including The New Horizons Forum and Aerospace Exposition.* 2009, p. 612.

[35]   S. S. Collis, R. D. Joslin, A. Seifert, and V. Theofilis. "Issues in active flow control: theory, control, simulation, and experiment". In: *Progress in Aerospace Sciences* 40.4-5 (2004), pp. 237–289.

[36]   A. S. Sharma, J. F. Morrison, B. J. McKeon, D. J. N. Limebeer, W. H. Koberg, and S. J. Sherwin. "Relaminarisation of Reτ= 100 channel flow with globally stabilising linear feedback control". In: *Physics of Fluids* 23.12 (2011), p. 125105.

[37]   S. A. Jacobson and W. C. Reynolds. "Active control of streamwise vortices and streaks in boundary layers". In: *Journal of Fluid Mechanics* 360 (1998), pp. 179–211.

[38]   E. Moreau, R. Sosa, and G. Artana. "Electric wind produced by surface plasma actuators: a new dielectric barrier discharge based on a three-electrode geometry". In: *Journal of Physics D: Applied Physics* 41.11 (2008), p. 115204.

[39]   J. Wang, K. Choi, L. Feng, T. N. Jukes, and R. D. Whalley. "Recent developments in DBD plasma flow control". In: *Progress in Aerospace Sciences* 62 (2013), pp. 52–78.

[40]   M. Forte, J. Jolibois, J. Pons, E. Moreau, G Touchard, and M Cazalens. "Optimization of a dielectric barrier discharge actuator by stationary and non-stationary measurements of the induced flow velocity: application to airflow control". In: *Experiments in Fluids* 43.6 (2007), pp. 917–928.

[41]   N. Benard and E. Moreau. "Electrical and mechanical characteristics of surface AC dielectric barrier discharge plasma actuators applied to airflow control". In: *Experiments in Fluids* 55.11 (2014), p. 1846.

[42]   E. E. Kunhardt. "Electrical breakdown of gases: The prebreakdown stage". In: *IEEE Transactions on Plasma Science* 8.3 (1980), pp. 130–138.

[43]   J. Kriegseis. "Performance characterization and quantification of dielectric barrier discharge plasma actuators". PhD thesis. Technische Universität, 2011.

[44]   T. C. Corke, C. L. Enloe, and S. P. Wilkinson. "Dielectric barrier discharge plasma actuators for flow control". In: *Annual Review of Fluid Mechanics* 42 (2010), pp. 505–529.

[45]   J. P. Boeuf, Y. Lagmich, Th. Unfer, Th. Callegari, and L. C. Pitchford. "Electrohydrodynamic force in dielectric barrier discharge plasma actuators". In: *Journal of Physics D: Applied Physics* 40.3 (2007), p. 652.

[46]   E. Moreau. "Airflow control by non-thermal plasma actuators". In: *Journal of Physics D: Applied Physics* 40.3 (2007), p. 605.

[47]   I. Maden, R. Maduta, J. Kriegseis, S. Jakirlić, C. Schwarz, S. Grundmann, and C. Tropea. "Experimental and computational study of the flow induced by a plasma actuator". In: *International Journal of Heat and Fluid Flow* 41 (2013), pp. 80–89.

[48]   C. L. Enloe, T. E. McLaughlin, G. I. Font, and J. W. Baughn. "Parameterization of temporal structure in the single-dielectric-barrier aerodynamic plasma actuator". In: *AIAA Journal* 44.6 (2006), pp. 1127–1136.

[49]   T. N. Jukes and K. Choi. "Dielectric-barrier-discharge vortex generators: characterisation and optimisation for flow separation control". In: *Experiments in Fluids* 52.2 (2012), pp. 329–345.

[50]   N. Balcon, N. Benard, and E. Moreau. "Formation process of the electric wind produced by a plasma actuator". In: *IEEE Transactions on Dielectrics and Electrical Insulation* 16.2 (2009), pp. 463–469.

[51]   R. Whalley and K. Choi. "Starting, traveling, and colliding vortices: dielectric-barrier-discharge plasma in quiescent air". In: *Physics of Fluids* 22.9 (2010), p. 091105.

[52]   R. D. Whalley and K. Choi. "The starting vortex in quiescent air induced by dielectric-barrier-discharge plasma". In: *Journal of Fluid Mechanics* 703 (2012), pp. 192–203.

[53]   X. Zhang, Y. D. Cui, C. M. J. Tay, and B. C. Khoo. "Flow field generated by a dielectric barrier discharge plasma actuator in quiescent air at initiation stage". In: *Chinese Journal of Aeronautics* (2020).

[54]   T. N. Jukes and K. Choi. "On the formation of streamwise vortices by plasma vortex generators". In: *Journal of Fluid Mechanics* 733 (2013), pp. 370–393.

[55]   J. R. Roth, D. M. Sherman, and S. P. Wilkinson. "Electrohydrodynamic flow control with a glow-discharge surface plasma". In: *AIAA journal* 38.7 (2000), pp. 1166–1172.

[56]   C. L. Enloe, T. E. McLaughlin, R. D. VanDyken, K. D. Kachner, E. J. Jumper, T. C. Corke, M. Post, and O. Haddad. "Mechanisms and responses of a dielectric barrier plasma actuator: Geometric effects". In: *AIAA Journal* 42.3 (2004), pp. 595–604.

[57]   F. O. Thomas, T. C. Corke, M. Iqbal, A. Kozlov, and D. Schatzman. "Optimization of dielectric barrier discharge plasma actuators for active aerodynamic flow control". In: *AIAA Journal* 47.9 (2009), pp. 2169–2178.

[58] R. J. Durscher and S. Roy. "Three-dimensional flow measurements induced from serpentine plasma actuators in quiescent air". In: *Journal of Physics D: Applied Physics* 45.3 (2012), p. 035202.

[59] R. E. Hanson, N. M. Houser, and P. Lavoie. "Dielectric material degradation monitoring of dielectric barrier discharge plasma actuators". In: *Journal of Applied Physics* 115.4 (2014), p. 043301.

[60] N. Benard, P. Note, M. Caron, and E. Moreau. "Highly time-resolved investigation of the electric wind caused by surface DBD at various ac frequencies". In: *Journal of Electrostatics* 88 (2017), pp. 41–48.

[61] T. C. Corke, M. L. Post, and D. M. Orlov. "Single dielectric barrier discharge plasma enhanced aerodynamics: physics, modeling and applications". In: *Experiments in Fluids* 46.1 (2009), pp. 1–26.

[62] S. Sato, H. Furukawa, A. Komuro, M. Takahashi, and N. Ohnishi. "Successively accelerated ionic wind with integrated dielectric-barrier-discharge plasma actuator for low-voltage operation". In: *Scientific Reports* 9.1 (2019), pp. 1–11.

[63] G. Neretti, A. Cristofolini, C. A. Borghi, A. Gurioli, and R. Pertile. "Experimental results in DBD plasma actuators for air flow control". In: *IEEE Transactions on Plasma Science* 40.6 (2012), pp. 1678–1687.

[64] J. Kriegseis, B. Simon, and S. Grundmann. "Towards in-flight applications? A review on dielectric barrier discharge-based boundary-layer control". In: *Applied Mechanics Reviews* 68.2 (2016).

[65] A. Duchmann, B. Simon, C. Tropea, and S. Grundmann. "Dielectric barrier discharge plasma actuators for in-flight transition delay". In: *AIAA Journal* 52.2 (2014), pp. 358–367.

[66] S. Grundmann and C. Tropea. "Experimental damping of boundary-layer oscillations using DBD plasma actuators". In: *International Journal of Heat and Fluid Flow* 30.3 (2009), pp. 394–402.

[67] K. Barckmann, C. Tropea, and S. Grundmann. "Attenuation of Tollmien–Schlichting waves using plasma actuator vortex generators". In: *AIAA Journal* 53.5 (2015), pp. 1384–1388.

[68] J. HM. Fransson, A. Talamelli, L. Brandt, and C. Cossu. "Delaying transition to turbulence by a passive mechanism". In: *Physical review letters* 96.6 (2006), p. 064501.

[69] Jé. Jolibois, M. Forte, and É. Moreau. "Application of an AC barrier discharge actuator to control airflow separation above a NACA 0015 airfoil: Optimization of the actuation location along the chord". In: *Journal of Electrostatics* 66.9-10 (2008), pp. 496–503.

[70] M. L. Post and T. C. Corke. "Separation control on high angle of attack airfoil using plasma actuators". In: *AIAA Journal* 42.11 (2004), pp. 2177–2184.

[71] K. M. Bade, R. E. Hanson, B. A. Belson, A. M. Naguib, P. Lavoie, and C. W. Rowley. "Reactive control of isolated unsteady streaks in a laminar boundary layer". In: *Journal of Fluid Mechanics* 795 (2016), pp. 808–846.

[72] K. Sasaki, P. Morra, A. V. G. Cavalieri, A. Hanifi, and D. S. Henningson. "On the role of actuation for the control of streaky structures in boundary layers". In: *Journal of Fluid Mechanics* 883 (2020).

[73] G. I. Font, C. L. Enloe, and T. E. McLaughlin. "Plasma volumetric effects on the force production of a plasma actuator". In: *AIAA Journal* 48.9 (2010), pp. 1869–1874.

[74] R. Futrzynski. "Drag reduction using plasma actuators". PhD thesis. KTH Royal Institute of Technology, 2015.

[75] M. Kotsonis, S. Ghaemi, L. Veldhuis, and F. Scarano. "Measurement of the body force field of plasma actuators". In: *Journal of Physics D: Applied Physics* 44.4 (2011), p. 045204.

[76] H. Shan and Y. T. Lee. "Numerical modeling of dielectric barrier discharge plasma actuation". In: *Journal of Fluids Engineering* 138.5 (2016).

[77] Y. Suzen and G. Huang. "Simulations of flow separation control using plasma actuators". In: *44th AIAA Aerospace Sciences Meeting and Exhibit*. 2006, p. 877.

[78] B. Jayaraman and W. Shyy. "Modeling of dielectric barrier discharge-induced fluid dynamics and heat transfer". In: *Progress in Aerospace Sciences* 44.3 (2008), pp. 139–191.

[79] W. Shyy, B. Jayaraman, and A. Andersson. "Modeling of glow discharge-induced fluid dynamics". In: *Journal of Applied Physics* 92.11 (2002), pp. 6434–6443.

[80] C. Enloe, T. McLaughlin, R. Van Dyken, and J. Fischer. "Plasma structure in the aerodynamic plasma actuator". In: *42nd AIAA Aerospace Sciences Meeting and Exhibit*. 2004, p. 844.

[81] J. Sack and J. Urrutia. *Handbook of Computational Geometry*. Elsevier, 1999.

[82] C. Tropea and A. L. Yarin. *Springer Handbook of Experimental Fluid Mechanics*. Springer Science & Business Media, 2007.

[83] O. Mahfoze and S. Laizet. "Skin-friction drag reduction in a channel flow with streamwise-aligned plasma actuators". In: *International Journal of Heat and Fluid Flow* 66 (2017), pp. 83–94.

[84] D. Anderson, J. C. Tannehill, and R. H. Pletcher. *Computational fluid mechanics and heat transfer*. Taylor & Francis, 2016.